Electrochemical Reduction of Metal Oxides in Molten Salts for Nuclear Reprocessing

Thesis submitted to University College London

by

Rema Abdulaziz

In fulfilment of the requirements for the degree of

Doctor of Philosophy

2016

Declaration

I, Rema Abdulaziz, confirm that the work presented in this thesis is my own. Where information has been derived from other sources, I confirm that this has been indicated in the thesis.

Rema Abdulaziz

To Professor Douglas Inman,

Abstract

This thesis examines the electrochemical reduction of metal oxides in molten salts for nuclear reprocessing applications. This is of particular importance for the development of Gen IV nuclear power plants, where if pyroprocessing was to be implemented, electro-reduction and refining of spent nuclear fuel are two main steps in reprocessing. The objective of this research is to characterise and understand the direct electrochemical reduction of UO_2 to U metal in a LiCl-KCl molten salt eutectic, as part of the nuclear pyroprocessing scheme, following a similar approach to the FFC Cambridge Process for the reduction of TiO_2 to Ti metal. The voltammetric behaviour of reduction processes of metal oxides were evaluated using electroanalytical techniques such as cyclic voltammetry and chronoamperometry on different precursor types, such as thermally grown thin oxide films, metallic cavity electrodes, and 'a fluidised cathode', a novel system that was developed within this work. Material was characterised before and after the electroanalytical experiments using scanning electron microscopy, X-ray energy dispersive spectroscopy and X-ray diffraction.

Predominance phase diagrams, using recent thermodynamic data, for metal-molten salt systems, relating the potential to the negative logarithm of the activity of O^{2-} ions (E-pO^{2-}), were produced for the range of spent nuclear materials (U, Pu, Np, Am, Cm, Cs, Nd, Sm, Eu, Gd, Mo, Tc, Ru, Rh, Ag and Cd species), in both LiCl-KCl at 500 °C and NaCl-KCl at 750 °C. The two salt eutectics were chosen as they are the two main systems for pyroprocessing in the UK and US; temperatures were selected within each salt's normal operating range. All of the diagrams show regions of stability for the different metal species, their oxides and chlorides at unit activity; however, this activity can be altered in accordance with the equations derived. Examples of selective electrochemical reduction are also demonstrated for potential spent fuel reprocessing in both salt systems. In addition, the effects of

altering the operating temperature on the regions of stability within the diagrams are also investigated.

The bulk of this research was on investigating the electrochemical reduction of WO_3 to W metal. Tungsten was selected as a chemical surrogate for uranium, due to their similar physical and chemical properties, to investigate specific electrochemical reduction and process parameters. Nonetheless, tungsten is an important and desirable refractory metal because of its physical and chemical properties, and the electrochemical route for producing it of high purity might prove viable. The electrochemical reduction of WO_3 to W metal has been assessed, alongside a predominance diagram that was developed for the Li-K-W-O-Cl system, and it likely to occur as following the reaction mechanisms: $WO_3 \rightarrow WO_2 \rightarrow W$. A full reduction using the fluidised cathode process, with complete conversion of the product to W was achieved, via applying a constant potential of -2.14 V, with a high Faradaic efficiency. The reduction process is split into two sections; the first where rapid reduction of WO_3 occurs, the second where a slower reduction of the remaining oxides in the product takes place. The deposited material on the current collector is in the form of homogeneously distributed particles.

Parameters, such as the metal oxide-salt ratio and the fluidisation rate, were investigated, and depending on the desired means of recovery of the product, i.e. a continuous flow retrieval or batch via removal of electrodes, these conditions can be altered to suit. Particle coulometric analysis was also carried out, and an electrochemical deposition model was also developed to estimate the porosity of the deposit and the rate of its growth over time.

Finally, the electrochemical reduction of UO_2 to U metal using the fluidised cathode process was investigated. Voltammetry studies were conducted, and alongside a predominance diagram that was constructed, the reaction path-way was studied, and it is likely to take place following two different reaction mechanisms; $UO_2 \rightarrow U$, via a 4-electron transfer step reaction; and $UO_2 \rightarrow UO \rightarrow U$, via two 2-electron step reactions. The route the reduction process follows depends on pO^{2-}

and potential, which is highly influenced by the type of metal oxide precursor used, metallic cavity packed electrode or a fluidised cathode.

The main reduction potential using the fluidised cathode appeared to be -2.2 V. A Faradaic current efficiency for the process was established, and found to be ~ 92%. However this is a very rough estimate. The reduction process is split into three sections; the first where a seeding process takes place at a low potential to allow for the reduced uranium particles to be deposited onto the tungsten current collector; the second where rapid reduction of UO_2 particles takes place with a growth in electrode size accompanied by an increase in current being passed; the third where a slower reduction of the remaining oxides in the product occurs. As is the case with the electrochemical reduction of tungsten oxide, the reduced product can be collected from two areas; the deposit on the current collector's surface and the bottom of the reactor crucible.

The fluidised cathode is a robust, three-phase, high efficiency process. It was studied here for the electrochemical reduction of WO_3 and UO_2, however, it is likely applicable for other spent fuel oxides (such as UO_3 and PuO_2), and in the production of refractory metals, such as titanium. Another proposed advantage of using the fluidised cathode process is that it would eliminate certain steps in the preparation of the precursor and recovery of the reduced metal in the FFC Cambridge process with associated cost reductions.

Acknowledgements

During the many days and nights when this research was all consuming, several persons provided indispensable support. People to whom I am particularly indebted include:

- Professor Douglas Inman, to whom this thesis is dedicated, for his insight, advice and energy. He was an excellent mentor and friend, and I will always be grateful to have known him.
- My supervisor, Professor Dan Brett, for his unparalleled enthusiasm, guidance and confidence in me. I thoroughly enjoyed our regular meetings and discussions, and have learnt a lot from him.
- My second supervisor, Dr. Paul Shearing, for his support and for giving me the opportunities to gain experience working at Diamond Light Source and ISIS Neutron Source.
- The Department of Chemical Engineering, especially Professor Eva Sorensen, Professor Eric Fraga, Dr. Simon Barrass and Professor Bill Maskell.
- John Cowley and Michael Williams for their brilliant glassblowing skills, and Martin Vickers for his help with XRD (UCL Department of Chemistry).
- My friends and colleagues from the second floor, especially Shade, Matt, Vassilis, Chara and Noor.
- My friends and colleagues from the Electrochemical Innovation Lab, especially Toby, Jay, Amal, Quentin, Ishanka, Ana and Rhod.
- The EPSRC funded REFINE consortium, especially Dr. Clint Sharrad for providing UO_2 powder.
- My parents, Ahmed and Naima, and siblings, Rabea, Aisha and Mariam, for their unconditional love and support through the years.
- My friends for being the best support system one could ask for, especially Eoin, Holly, Rosalind, Fatma, Frances, Teodora, Malvika, Azza, Tom, John, George, Clair, Chiaki, Roxy, Damir, Haydar, Tomek, Grace and Jessica.

Table of contents

List of Figures

List of Tables

Nomenclature

List of abbreviations

3PI	Three phase interline
AEM	Alkaline earth metal
AGR	Advanced gas-cooled reactor
AM	Alkali metal
ANL	Argonne National Laboratory
BWR	Boiling water reactor
CV	Cyclic voltammetry
EDS	X-ray energy dispersive spectroscopy
EXAm	Extraction of americium
FBR	Fast breeder reactor
FFC	Fray Farthing Chen
FIB	Focused ion beam
FP	Fission products
GCR	Gas-cooled, graphite-moderated reactor
GFR	Gas-cooled fast reactor
GHG	Greenhouse gases
HLW	High level waste
IFR	Integral fast reactor
LEP	Liquid electrolyte phase
LFR	Lead-cooled fast reactor
LILW	Low and intermediate level waste
LSV	Linear sweep voltammetry
LWGR	Light-water-cooled, graphite-moderated reactor
LWR	Light water reactor
M	Metal
MA	Minor actinide
MCE	Metallic cavity electrode
MOX	Metal oxide
MSR	Molten salt reactor
MTHM	Metric tonne of heavy metal
NEA	Nuclear Energy Agency
NM	Noble metal
O	Oxidised species
OS	Ono Suzuki

PHWR	Pressurised heavy-water-cooled and moderated reactor
PUREX	Plutonium-uranium extraction
PWR	Pressurised water reactor
R	Reduced species
RE	Rare earth metal
RIAR	Research Institute of Atomic Reactors
SANEX	Selective actinide extraction
S.Cl.E	Standard chlorine electrode
SCP	Solid compound phase
SCWR	Supercritical-water-cooled reactor
SEM	Scanning electron microscopy
SFR	Sodium-cooled fast reactor
SMP	Solid metal phase
TBP	Tri-butyl phosphate
TRISO	Tristructural-isotropic fuel
TRU	Transuranic material
TRUEX	Transuranic extraction
UNF	Used nuclear fuel
UOX	Uranium oxide
VHTR	Very-high-temperature reactor
XRD	X-ray diffraction

List of Symbols

ΔG^0	Gibbs energy of formation	J mol^{-1}
ΔT	Change in temperature	K
θ	Angle	Rad
λ	Wavelength	m
ρ	Density	kg m^{-3}
a	Thermodynamic activity	-
C	Concentration	mol m^{-3}
C_O	Concentration of O	mol m^{-3}
C_{bulk}	Concentration of bulk	mol m^{-3}
c	Specific heat capacity	J kg^{-1} K^{-1}
D_O	Diffusion coefficient of O	m^2 s^{-1}
d	Interplanar spacing	m
E	Potential	kg m^2 s^{-3} A^{-1} (V)
E^0	Standard electrode potential	kg m^2 s^{-3} A^{-1} (V)
E_d	Defined potential	kg m^2 s^{-3} A^{-1} (V)
$E_{O/R}$	Reduction potential for redox couple O and R	kg m^2 s^{-3} A^{-1} (V)
e	Electronic charge (1.602×10^{-19} C)	A s (C)

F	Faraday constant (96485 C mol^{-1})	A s mol^{-1} (C mol^{-1})
I	Current	A
i	Current	A
ID	Inner diameter	m
k	Specific conductance	A^2 s^3 kg^{-1} m^{-3} (S m^{-1})
L	Length	m
L	Latent heat	J kg^{-1}
M	Molar mass	kg mol^{-1}
m	Mass	kg
N	Number of reduced oxide units	-
N_A	Avogadro constant (6.022×10^{23} mol^{-1})	mol^{-1}
$N(t)$	Molar accumulation at t	mol
n	Number of moles	mol
OD	Outer diameter	m
P	Partial pressure	kg m^{-1} s^{-2} (Pa)
P	Power	J s^{-1}
pO^{2-}	$-\log_{10}[O^{2-}]$	-
Q	Charge	A s (C)
Q	Heat	J
q	Flux	mol m^{-2} s^{-1}
R	Universal gas constant (8.314 J K^{-1} mol^{-1})	J K^{-1} mol^{-1}
R	Resistance	kg m^2 s^{-3} A^{-2} (Ω)
r	Radius	m
r_0	Radius at $t = 0$	m
$r(t)$	Radius at t	m
T	Temperature	K
T_f	Final temperature	K
T_s	Start temperature	K
t	Time	s
t_s	Start time	s
t_d	Defined time	s
V	Voltage	kg m^2 s^{-3} A^{-1} (V)
$V(t)$	Volume at t	m^3
x	Distance	m
z	Number of e transferred per reduced formula unit of oxide	-

1. Introduction

The world's energy consumption increases with the growth of economies, and demand is expected to increase by a factor of 1.5-3 by 2050. Furthermore, standards of living are directly related to the availability of electricity, for which the demand is expected to be twice as large by 2050 as well [1]. The majority of global electricity is derived from the burning of fossil fuels, which produces greenhouse gases (GHG) that are large contributors to global climate change. Though the use of renewable energy resources continues to develop, it is still not satisfactory for fulfilling energy demands [2]. Figure 1.1 shows the breakdown of the world electricity generation by source of energy, in 1971 and 2010. Nuclear energy for electricity generation offers large-scale low-carbon energy production, but suffers with challenges such as the handling of radioactive waste materials.

For low and intermediate level waste (LILW) disposal facilities already exist in twenty three countries around the world. As for high level waste (HLW) no such facilities exist. However, there are storage facilities in operation. The disposal of HLW is the only step in the civilian nuclear fission cycle with no large scale facilities in operation yet [3].

The reprocessing of spent nuclear fuel is important as it can reduce the amount of waste to be disposed of, and lessens the indirect environmental footprint. Most of the GHG emissions associated with nuclear power come from construction (40%), mining activities (32%) and enrichment (12%); whereas, conversion, disposal and reprocessing are only responsible for 5, 2 and 7% respectively [4]. Therefore, by reducing or forfeiting the mining and the enrichment steps, via reprocessing, the GHG emissions would be significantly reduced.

While the reprocessing of some of the spent fuel materials increases the efficiency of the fuel-cycle, the reprocessing of other materials, such as the minor actinides, is only important for the public acceptance of civilian nuclear power. Also, the more

materials are reprocessed, the less space will be needed for underground storage in the future.

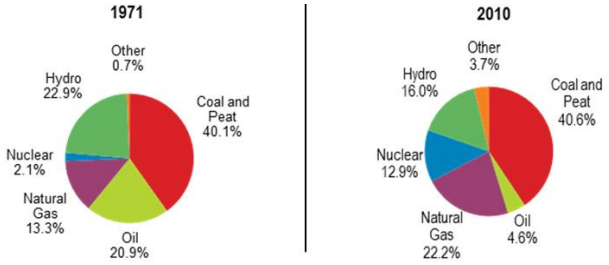

Figure 1.1 - World electricity generation by source of energy [5].

High temperature molten salt reprocessing technology (pyroprocessing) offers a range of advantages when compared to aqueous reprocessing techniques. This is due to the fact that the technology is inherently 'safe' as it is resistant to proliferation and does not provide an environment for criticality accidents to occur; it also utilises compact easily accessible facilities.

The aim of this research is to develop the understanding of spent nuclear materials behaviour in molten salts, via thermodynamic and electrochemical techniques, and to investigate electrochemical reduction processes from oxides to metals, which can prove to be significant in future generation IV nuclear power plants. New reactor designs are investigated as well, to improve the efficiency of such processes.

This thesis consists of a literature review where a concise background of nuclear pyroprocessing, molten salts, electrochemical reduction, and spent nuclear materials in molten salts is given. This is followed by an experimental Chapter where a background of the electrochemical techniques and characterisation techniques is included, in addition to specific experimental designs used later in this work. A theoretical Chapter where predominance diagrams, summarising the thermodynamic and electrochemical behaviour of spent nuclear materials in molten salts, were produced is also included. Then, two experimental Chapters were the electrochemical reduction of WO_3 and UO_2 were investigated. Finally, this is all summarised in the conclusion, where also suggestions for future work were provided.

2. Background Review

This Chapter aims to present a critical review of the relevant literature and has been split into sections that cover: a background review on nuclear energy and reprocessing technologies, molten salts and their applications, electrochemical reduction processes for metals production in molten salts, fluidised bed electrode technologies, and the electrochemistry of spent nuclear materials in molten salts found in the literature.

2.1 Nuclear fuel cycle

The closed nuclear fuel cycle is outlined in Figure 2.1 and comprises of the following main steps:

1. Mining and milling of the ore (the creation of the 'yellow cake').
2. Purifying the ore and enriching of the fissile U^{235} content, if needed, then manufacturing the fuel.
3. Utilising the fuel in various reactor types, normally as fuel pellets in fuel rods. This is different for different reactors.
4. Reprocessing of the spent fuel at the end of its life time, where separating and recycling of uranium and plutonium occurs.
5. Safe and secure disposal of the remaining radioactive waste.

To close the back-end of the nuclear fuel cycle, uranium and plutonium are reprocessed, then recycled back into fuel for reactors. These reprocessing steps are highlighted in red in Figure 2.1. This is called the 'twice through cycle'. Ignoring reprocessing and the direct disposal of HLW into repositories is called the 'once through cycle'. Nonetheless, most legacy waste produced from nuclear power plants is in long term storage. This is not a permanent solution, but serves the quest of buying time to deal with nuclear waste materials some decades in the future [6]. Thus, for a sustainable nuclear power future, reprocessing of spent fuel material is vital.

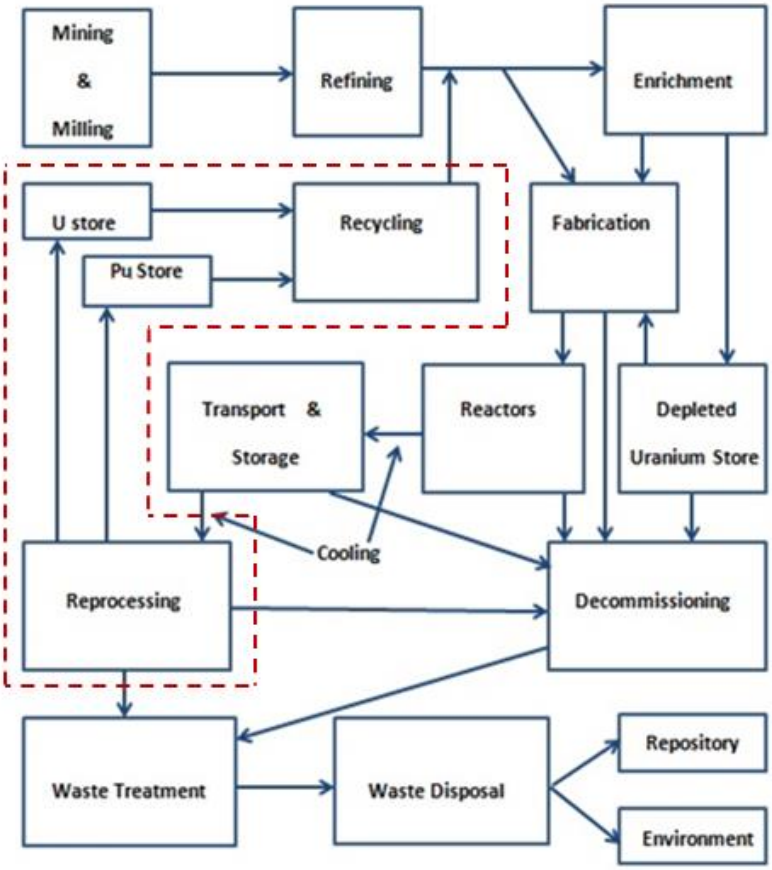

Figure 2.1 - The nuclear fuel cycle.

2.2 Nuclear reactors

Nuclear reactors are either thermal or fast reactors. They are classified by their purpose, by the type of moderator used to slow down neutrons, by the type of fuel or type of coolant used in them. The main purpose for using nuclear reactors is power generation; however, they are also used for research, testing and for the production of materials such as radioisotopes [7]. The principle types of nuclear reactors and their total net electrical capacities are summarised in Table 2.1.

Table 2.1 - World operational nuclear reactors in 2015 [8].

Reactor type	Description	Number of reactors	Total net electrical capacity (MW)
BWR	Boiling light-water-cooled and moderated reactor	78	74686
FBR	Fast breeder reactor	2	580
GCR	Gas-cooled, graphite-moderated reactor	15	8175
LWGR	Light-water-cooled, graphite-moderated reactor	15	10219
PHWR	Pressurised heavy-water-cooled and moderated reactor	49	24549
PWR	Pressurised light-water-cooled and moderated reactor	278	259777
Total		437	377986

The first generation of reactors that was used in the United Kingdom was the gas-cooled Magnox reactor. The following generation was the GCRs. The first PWR came much later, at Sizewell B. The majority of nuclear reactors in operation worldwide are light water reactors, especially PWRs.

Due to the phenomenon of nuclear decay, spent reactor fuel continues to give off heat even after the reactor has been shut down and the fission reactions have stopped. The graph in Figure 2.2, below, shows the heat given off by spent fuel from different reactors after shut down. Naturally, the heat release is highest when the spent fuel is first removed from the reactor and as time passes, it reduces significantly.

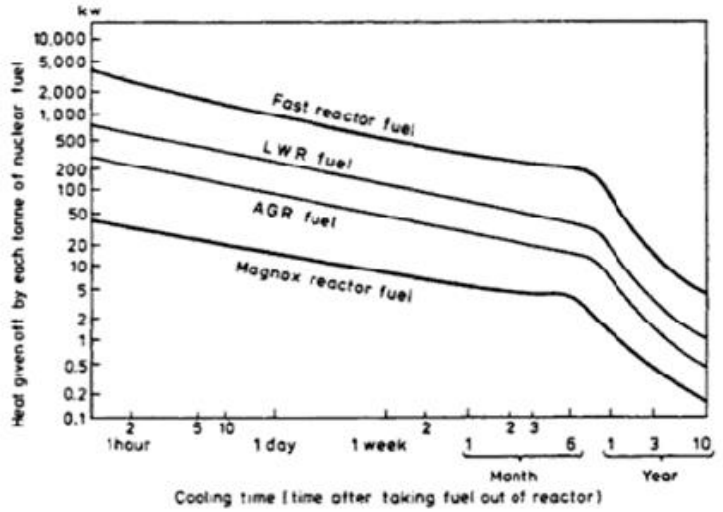

Figure 2.2 - Heat release from spent nuclear fuel [9].

In order to reduce the decay heat, spent nuclear fuel is stored in cooling water ponds for a relatively short time when first removed from the reactor. Carbon dioxide ponds have also been employed; however, they are not always suitable; for example, they cannot be used for spent fuel from Magnox reactors, as the magnesium moderator would form magnesium hydroxide [6]. PWRs' spent fuel can be stored for a very long time in cooling water ponds, which adds to the advantages of using them in power plants. Cooling ponds are maintained cool by using commercial heat exchangers and are easy to operate. However, there is a risk of reaching 'criticality'; this is when the pond itself starts acting as a nuclear reactor, when PWR, BWR and GCR spent fuel is being stored. For reactors that use natural uranium fuel, such as Magnox and PHWR, there is no criticality problem [9].

After the cooling off period is over, the fuel is transported from the ponds in safety flasks to reprocessing and discharge facilities.

2.3 Nuclear reprocessing

Reprocessing of irradiated nuclear fuel first started in the USA, in the 1940s; precipitation followed solvent extraction was used then. This was to separate weapons-grade plutonium from spent fuel materials. For the Manhattan Project, the plutonium-uranium extraction (PUREX) process was employed. In the PUREX process, uranium and plutonium are extracted, leaving fission products in the HLW disposal stream [10]. Two decades later, the UK and France adopted and modified the PUREX process, developing second generation reprocessing plants. Similarly, at different scales, improvements to the PUREX process took place in Belgium, Germany, Japan, Russia, China and India. In the 1980s, the UK and France developed the process further and established third generation civil reprocessing plants, where discharge of radioactive waste into the environment was reduced significantly. These facilities produced a mixture of non-weapons-grade uranium and plutonium called mixed oxide (MOX) fuel [11]. In the UK, however, these facilities have been closed recently. Table 2.2 shows the nuclear civil reprocessing plants around the world, and their capacities in 2014.

Table 2.2 - World commercial reprocessing capacity in 2014 [12].

Location (and design)	Reactor, fuel type	Capacity (t/year)
UK, Sellafield (THORP)	Thermal, oxide	600
UK, Sellafield (Magnox)	Thermal, metal	1500
France, La Hague (UP2-800, UP3)	Thermal, oxide	1700
Japan, Rokhashamura	Thermal, oxide	800
Japan, Tokai Mura	Thermal, oxide	40
Russia, Ozersk (Mayak)	Thermal, oxide	400
India (PHWR, 4 plants)	Thermal, metal	330

In the following sections, the two main nuclear reprocessing techniques, aqueous reprocessing and pyroprocessing are described.

2.3.1 Aqueous reprocessing

In aqueous reprocessing solvent extraction technologies are used. In most spent fuel reprocessing plants, the fuel is dissolved in nitric acid to aid the process. Equations 2.1-4 are the main dissolution reactions that take place between spent uranium species and nitric acid [11]. In the PUREX process, a solvent consisting of tri-butyl phosphate (TBP) dissolved in hydrocarbon diluent is contacted with a solution of dissolved nuclear fuel in nitric acid to extract uranium and plutonium, leaving fission products for disposal [10]. The separation process consists of four main steps; extraction, scrubbing, stripping and washing. This is demonstrated in Figure 2.3.

$$3UO_2 + 8HNO_3 \rightarrow 3UO_2(NO_3)_2 + NO + 4H_2O \quad 2.1$$

$$UO_2 + 4HNO_3 \rightarrow UO_2(NO_3)_2 + 2NO_2 + 2H_2O \quad 2.2$$

$$U_3O_8 + 7.5HNO_3 \rightarrow 3UO_2(NO_3)_2 + NO_2 + 0.35NO + 3.65H_2O \quad 2.3$$

$$UO_3 + 2HNO_3 \rightarrow UO_2(NO_3)_2 + H_2O \quad 2.4$$

Mixer-settlers are used for the extraction. They consist of two compartments and use equilibrium contactors, where the step concentration profile is the aqueous phase and the solvent is passed from one stage to another. This technology is implemented in Sellafield, La Hague and Rukhshamura [11].

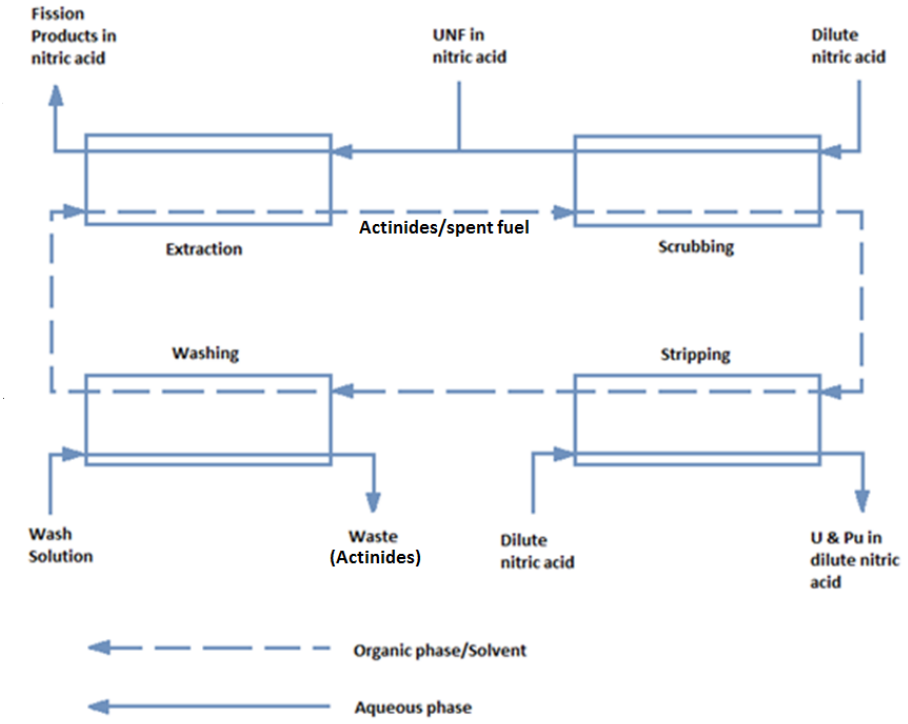

Figure 2.3 - Solvent extraction for used nuclear fuel (UNF).

The species in spent fuel that contribute the most to long-term radiotoxicity are the minor actinides, mainly Am, Cm, Np and Pu. Plutonium is recovered in the PUREX process, and neptunium can also be recovered in advanced PUREX processes. Other solvent extraction processes have been developed to extract the other minor actinides from the lanthanides, such as the transuranic extraction (TRUEX) for the removal of americium and curium, and the selective actinide extraction (SANEX) processes [13].

Solvent extraction for nuclear aqueous reprocessing suffers from a few drawbacks, primarily in terms of nuclear proliferation, as it provides a route for the separation of weapons-grade plutonium as a single species. Another concern, is that it employs solvents that contain hydrogen and carbon, which are neutron moderators, creating a criticality accident risk.

2.3.2 Pyroprocessing

Pyrochemical processing or pyroprocessing is a non-aqueous high temperature electrochemical method for the refinement and separation of irradiated spent nuclear fuel. It employs molten salts as solvents [14]. It is generally a desired scheme as it exploits more compact facilities than in solvent extraction, which is economically favourable for decontamination, it also requires a shorter cooling period for irradiated fuel, and it is a criticality accident risk-free process. Different process systems and salts have been studied in pyroprocessing, most of which are summarised in a Nuclear Energy Agency (NEA) report [15].

There are currently two main molten salt technology processes in existence, both using chloride salts as electrolytes; one in the USA at the Argonne National Laboratory (ANL) using LiCl-KCl eutectic, for metallic fuel for the Integral Fast Reactor (IFR), and one in Russia at the Research Institute for Atomic Reactors (RIAR) using NaCl-KCl eutectic, for oxide fuel for the Fast Breeder Reactor (FBR) [16]. Both processes are outlined in Figure 2.4. Another major difference between the ANL and the RIAR pyroprocessing systems is the removal of cladding. At RIAR cladding is removed before the pyrochemical refining stage, as is the practice in solvent extraction. This creates a radioactive waste stream. At ANL, it has been proposed that the zirconia fuel cladding is removed *in-situ* in the reprocessing stage via chlorination [17]. Equation 2.5 shows this dissolution reaction [18]. On a smaller scale, advances have been made in molten salt nuclear pyroprocesses in Europe and Japan as well [19-24].

$$ZrO_2 + 2Cl_2 \rightarrow ZrCl_4 + O_2 \qquad 2.5$$

Pyroprocessing is a desirable technology due to its inherent safety features, its ability to recover most fission products, and also because it is proliferation resistant, as it does not conventionally allow for the separation of weapons-grade plutonium as a single species, dissimilarly to the aqueous solvent extraction reprocessing schemes. Pyroprocessing remains in the R&D and pilot plant scales. Its facilities also require to be sealed from the atmosphere, and thus maintenance is very important. It also employs much higher temperatures than solvent extraction.

However, there is a clear motivation for implementing Generation IV nuclear reactors, which require metal as start-up fuel and follow a fully integrated and safe reactor and reprocessing design arrangements, hence, advances in the technology are made.

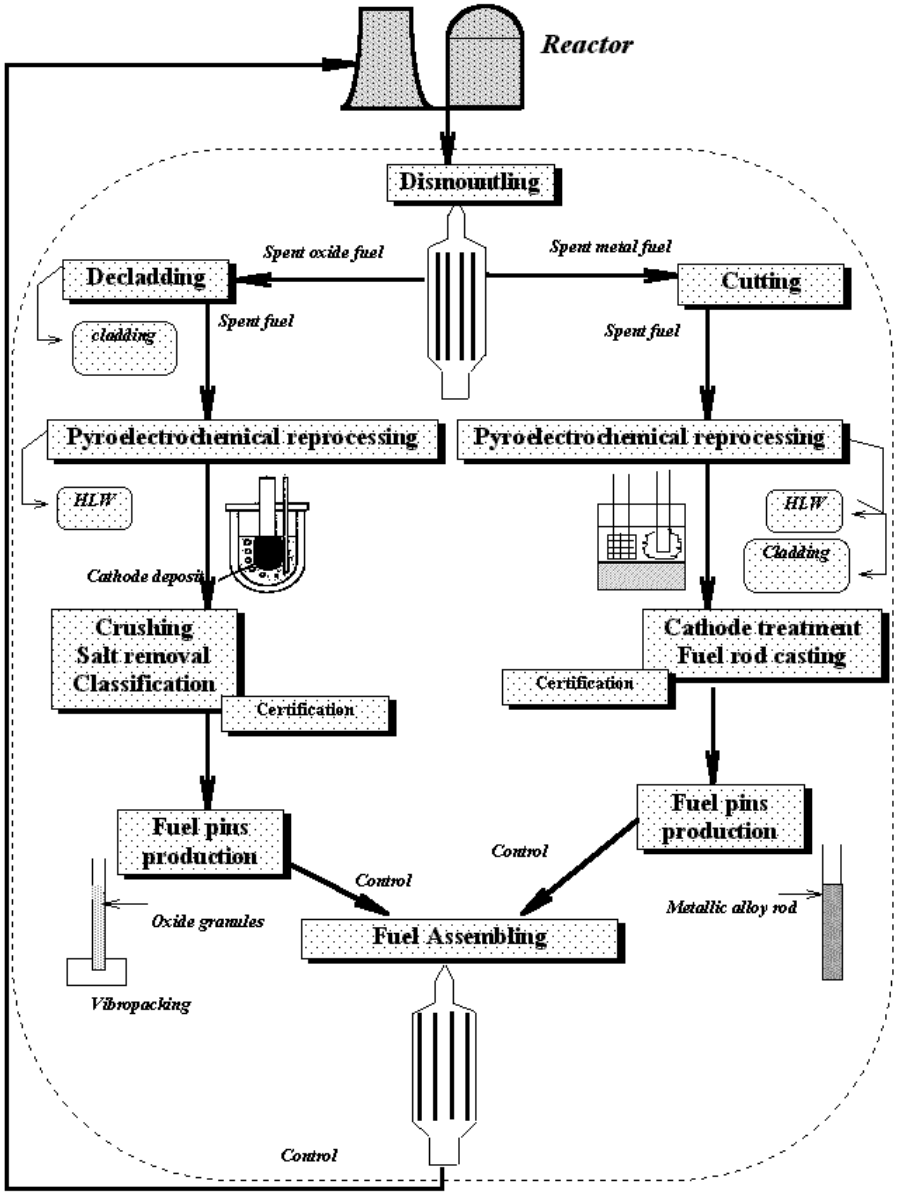

Figure 2.4 - Closed fuel cycles based on pyroprocessing developed at ANL (right branch) and RIAR (left branch) (Note: dismounting should read disassembling in the top box of the diagram) [25].

2.4 Molten salts

Molten salts are used extensively in the chemical industry. Their established applications are in the production of pure metals, such as aluminium, magnesium and sodium. They also have other important applications that are not fully exploited, which include molten salts fuel cells and batteries, catalysis, in the glass industry, and in solar power and energy storage [26].

In this section, a review of the characteristics and applications of molten salts as electrolytes is given.

2.4.1 Molten salt electrolysis

Molten salt electrolysis can be used for the electro-winning, refining and plating of refractory metals (Ti, V, Cr, Zr, Nb, Mo, Hf, Ta, W). The conversion of metals from their ores to their finished refractory stage is both energy and capital intensive. The electrochemical process scheme is a natural solution for these demands, as it significantly reduces operating costs through increasing the efficiency of the recovery of metals [27].

For most refractory metals electro-hydrometal-lurgical routes are not feasible for production, due to one or more of the following reasons [28]:

1. Most of these metals can only be electrodeposited at potentials more negative than those required for hydrogen evolution, as thermodynamic data shows.
2. The metals rapidly become protected by oxide films in oxidising environments. This can be a problem in fused salt systems too.
3. Metallic ions often get transformed to stable oxy-cations in aqueous solutions. Metallic ions with low oxidation states reduce water (e.g. Ti^{2+}), and those with high oxidation states oxidise water (e.g. Ti^{5+}).

As a result of these factors, the use of molten salts as solvents for electrolytic processes in metals production has emerged. The industrial applications of molten salts have been well acknowledged for more than a century. The commercial production of Al, Mg, Na, K, Li and Be make use of molten salt electrolysis processes [29]. However, the major processing routes for most refractory metals

are thermal, although most of them have also been extracted, refined or formed via molten salt electrolysis in laboratory or pilot plant scale [28].

2.4.2 Advantages of using molten salts as electrolytes

Molten salts are non-aqueous electrolytes. One of their best features is their large electrochemical window, which allows for a large variety of electrochemical processes to be carried out, as alkaline earth halides in salts have very negative Gibbs energies of formation, hence molten salts have a high decomposition potential, nonetheless this potential can be reduced by lowering the activity of the metal [28]. There is also a large number of different salts, salt mixtures and salt eutectics to choose from, with a wide temperature range (e.g. LiCl-KCl molten at 352 ˚C and operational at much higher temperatures). This allows for the various electrochemical reactions and their rates to be controlled via temperature. Hence, molten salts are defined into two categories; high temperature salts (above 700 ˚C) and low temperature salts (below 700 ˚C) [30]. In addition, molten salts have a good ionic conductivity range (2-9 $(\Omega\ cm)^{-1}$) [31].

When comparing molten salts to aqueous solutions, molten salts have the capacity to dissolve materials to a very high concentration. This high solubility results in a high limiting current density, and hence high productivity [32]. Chemical reactions between the metal ions and the solvent are generally absent in molten salt processes. However, due to the variety of metal oxidation states, interactions between the metal ions and the solvent must be carefully monitored.

In a reaction vessel, when a cold metal electrode is immersed into the molten salt solvent, a thin film of solid salt forms on the metal surface, acting as a temporary insulator, this reduces any thermal shock from taking place. This thin film and the high heat and wetting properties of salts cause the so called ‘preheating effect’, where rapid heat transfer through conduction takes place. Similarly, when the metal electrodes are removed from the vessel a thin liquid film forms on the surface. This helps in the protection and the cooling down of the final product. Also, when the reaction vessel is sealed from the environment, oxide formation and scaling effects of the materials are eliminated. This lessens maintenance problems [33].

Molten salt processes are also relatively low in initial costs. The reactor vessels normally have easy accessibility, regardless of how complex the system may be, and the final retrieved product is typically of high purity [29].

The intensive research on the subject over the past century has determined the various physical, chemical and thermodynamic properties of molten salt systems to a high standard. Nevertheless, until recently, not many innovative processes of using molten salt electrolysis for metal production have been developed [34].

2.4.3 Disadvantages of using molten salts as electrolytes

Despite the many advantages of using molten salts as electrolytes, there are a number of disadvantages. One of which is that the metal deposits produced by molten salt electrolysis are usually dendritic and/or powdery mixed with salt, which leads to a recovery process that is usually energy intensive and requires a consolidation process, which involves leaching, grinding and floatation procedures. Large scale molten salt processes can also prove to be difficult, as peripheral handling facilities are normally employed. Also, the insolubility of the high valence metal halides (mainly chlorides) can form cluster-type compounds within the electrolytic melt, which can complicate the process [28]. Another issue is the formation of CO_2/CO at the 'inert' anode, which is ordinarily a form of carbon. This could back-react with the metal deposited.

Due to the corrosive nature of molten salts when exposed to the environment (oxygen), reactor vessels and electrode materials can become damaged if not handled appropriately [29]. Serious health hazards can also arise from molten salt processes. This is due to their high operating temperatures and chemical reactions, which can yield toxic fumes. However, these hazards can be eliminated by proper design and planning, taking risk precautions, and the periodic cleaning and replenishment of salts and equipment [33].

2.4.4 Operating temperatures of molten salts

Frequently, mixtures of molten salts are used instead of a single salt. These mixtures are binary, ternary and sometimes even quaternary. They usually have much lower melting temperatures than pure salt constituents. This allows for

manipulations of the system's chemistry and temperature, to achieve desired operating designs. Table 2.3 shows the melting points of a few selected salts and salt mixtures.

Table 2.3 - Melting temperatures of salt mixtures and pure salt constituents [31, 35].

Constituents	Amounts (mol%)	Melting point (˚C)	Usual temperature used at (˚C)	Pure constituents	Melting point (˚C)
LiCl-KCl	59-41 (eutectic)	352	450-500	CaCl	772
NaCl-KCl	50-50	658	725-750	LiCl	610
$MgCl_2$-NaCl-KCl	50-30-20	396	475	NaCl	801
$AlCl_3$-NaF	50-50	154	175	$MgCl_2$	714
BF_3-NaF	50-50	408		KCl	770
AlF_3-NaF	25-75	1009	1080	$AlCl_3$	192*
				NaF	995
				AlF_3	1272*

*Under pressure

Some molten salt mixtures form eutectics, which have a unique minimum melting point, at a distinctive molar composition of the salt components. LiCl-KCl is such a eutectic; its phase diagram is depicted in Figure 2.5. Eutectics are common in chemistry, when two or more species, with their own bulk lattice arrangements, strike a unique composition forming a superlattice, that can release all its components at once into a liquid mixture at a much lower distinct temperature [36].

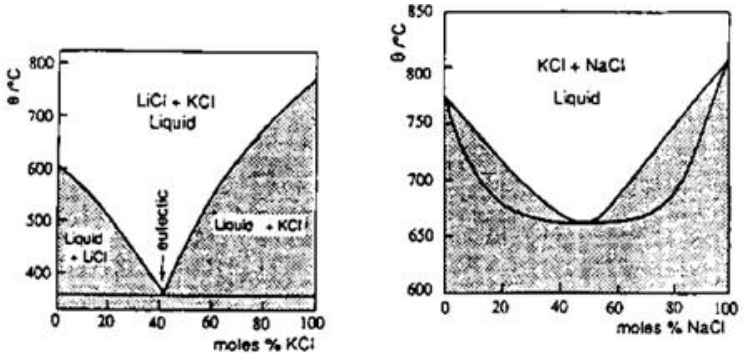

Figure 2.5 - Liquid state domains (non-shaded zones) of salt mixtures [35].

2.4.5 Conductance of molten salts

Molten salts have high ionic conductance, especially chlorides, which makes them ideal mediums for electrolytic processes. Figure 2.6 shows the specific ionic conductance of some pure molten salts at different temperatures. The high conductance of lithium chloride is particularly notable. When using salt mixtures, their specific conductance can be calculated using Equation 2.6, where *a*, *b* and *c* are parameters tabulated by Van Artsdaled and Yaffe [37] for different molar compositions of various salt mixtures and temperature ranges.

$$k = a + bT + cT^2 \qquad 2.6$$

Where, k is the specific conductance in mho cm^{-1};

T is the temperature in ˚C.

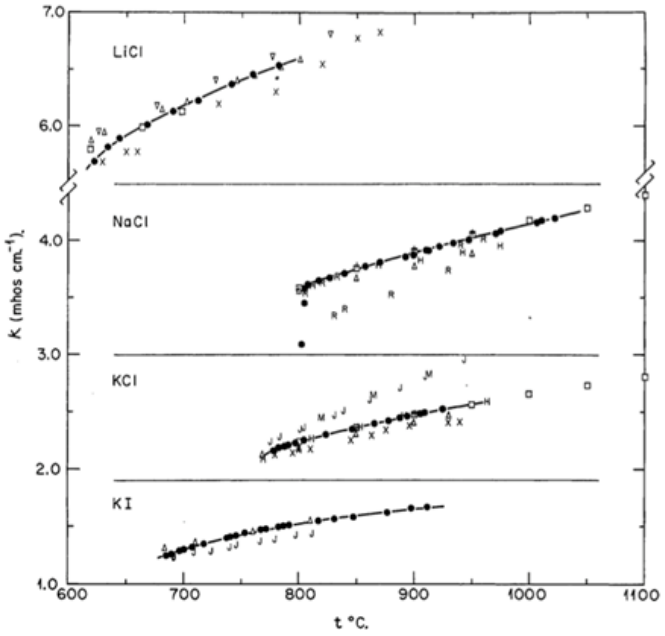

Figure 2.6 - Specific conductance of pure molten salts vs. temperature [37].

2.4.6 Density of molten salts

Molten salts possess relatively low densities, which contribute to them having good diffusion and dissolution properties. The densities of some molten salt eutectic

mixtures at different temperatures are presented in Figure 2.7. The relatively low density of LiCl-KCl eutectic is noteworthy, as it inhances transport phenomena in the fused salt. The density of pure salts and various salt mixtures can be calculated using Equation 2.7, where *a* and *b* are constants also published by Van Artsdaled and Yaffe [37] for different molar compositions of various salt mixtures and temperature ranges.

$$\rho = a - bT \qquad 2.7$$

Where, ρ is the density in g cm^{-3};

T is the temperature in ˚C.

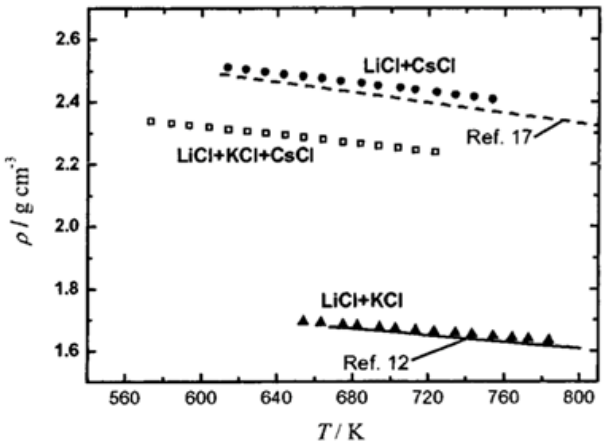

Figure 2.7 - Density of molten salt eutectic mixtures vs. temperature [38].

2.5 Electrochemical reduction of metal oxides in molten salts

2.5.1 The Fray Farthing Chen (FFC) Cambridge process

The FFC Cambridge process [39] is a novel approach for producing titanium metal from titanium oxide using molten salt electrolysis. Titanium has many advantages over other metals, in terms of weight, density, corrosion, maintenance and lifetime costs. However, its usage remains restricted due to its high production costs, and hence raw material cost [40]. The conventional method for producing metal

titanium is via the Kroll process [41]. In this process, $TiCl_4$ is reduced with pure magnesium in a molybdenum-lined crucible, in the presence of pure argon, at a temperature of 1000 ˚C. It is then separated from magnesium salts by leaching and acid treatment. The titanium metal in powder form is then compressed into bars and melted in special vacuum apparatus. The Kroll method for producing titanium metal is an expensive and complex procedure; Kroll himself predicted that his process would be replaced by an electrochemical process.

Since the 1950s and for forty years, research was underway in search of a new and cheaper method for titanium metal production, until the FFC Cambridge process was discovered in the late 1990s. The FFC Cambridge process is a novel electrolytic method for reducing metal oxide to metal in a molten salt medium. It was patented globally in 1998 [42, 43].

For the direct reduction of titanium oxide to metallic titanium, a qualified reducing agent, *R*, needs to be selected to remove the oxygen according to Equation 2.8.

$$TiO_x + xR \leftrightarrow Ti + xRO \qquad 2.8$$

The thermodynamic affinity of oxygen to *R* should be higher than to titanium. Reducing agents such as aluminium and carbon pollute and decrease the quality of the titanium metal produced. Only calcium and rare earth metals can reduce the remaining oxygen in the metal to less than 1000 mass ppm [44]. The reduction of titanium oxide chemically using calcium was proposed long before the FFC Cambridge process, however it was not considered due to the fact that calcium forms a CaO film on the titanium surface, which physically hinders the successive reduction by calcium. This is illustrated in Figure 2.8(a). The use of molten $CaCl_2$ salt as the electrolytic medium in the FFC process eliminates this problem, as $CaCl_2$ can dissolve amounts as large as 20 mol% of CaO and a few mol% of calcium. Hence, the CaO film would be removed as illustrated in Figure 2.8(b) [45]. This is the basis of the Ono-Suzuki (OS) process [46].

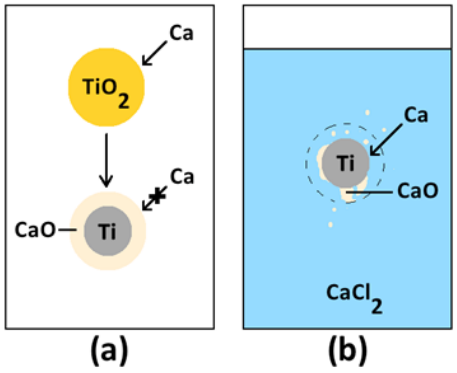

Figure 2.8 - Calcium reduction of TiO_2. (a) Calcium reduction. (b) Calcium reduction in molten $CaCl_2$.

There are two proposed mechanisms for the electrochemical reduction of titanium oxide in molten $CaCl_2$. These are as follows:

1. Deposition of calcium at a more cathodic potential followed by a chemical reaction:

$$Ca^{2+} + 2e^- \leftrightarrow Ca \quad 2.9$$

$$TiO_x + xCa \leftrightarrow Ti + xCaO \quad 2.10$$

2. Electrochemical reduction of Ti to release its oxide:

$$TiO_x + 2xe^- \leftrightarrow Ti + xO^{2-} \quad 2.11$$

In the first mechanism, the OS process, as presented in Equations 2.9 and 2.10, calcium is deposited on the titanium oxide cathode; it reacts with the titanium oxide on the surface forming CaO, which is soluble in $CaCl_2$. In the second mechanism, the FFC Cambridge process, as presented in Equation 2.11, direct reduction of titanium oxide is achieved electrochemically. Hence, the chemical reaction with calcium does not take place [39].

In the original FFC experiment, an electrochemical cell was constructed using titanium foil as the cathode and graphite as the anode, both were immersed in molten calcium chloride at 800 ˚C. Cyclic voltammograms were conducted, as illustrated in Figure 2.9. As can be seen, in the ‘as received’ titanium foil, Figure

2.9(b), cathodic peaks 1 and 2 and their anodic counterpart 7 are absent. These peaks are predominant in the cyclic voltammogram of the oxidised titanium foil, Figure 2.9(a). Peaks 1 and 2 appear at a less negative potential than that of calcium deposition, peaks 4 and 4' in (a) and (b) respectively. Thus, they are indicative of a direct electrochemical reduction of TiO_2. Peak 7 appears at a less positive potential than that of Cl_2 evolution, peaks 8 and 8', indicative of a reoxidation process. The electrochemical cell set-up, Figure 2.10, was later improved using TiO_2 pellets as the cathode and the temperature was raised to 950 ˚C to enhance kinetics.

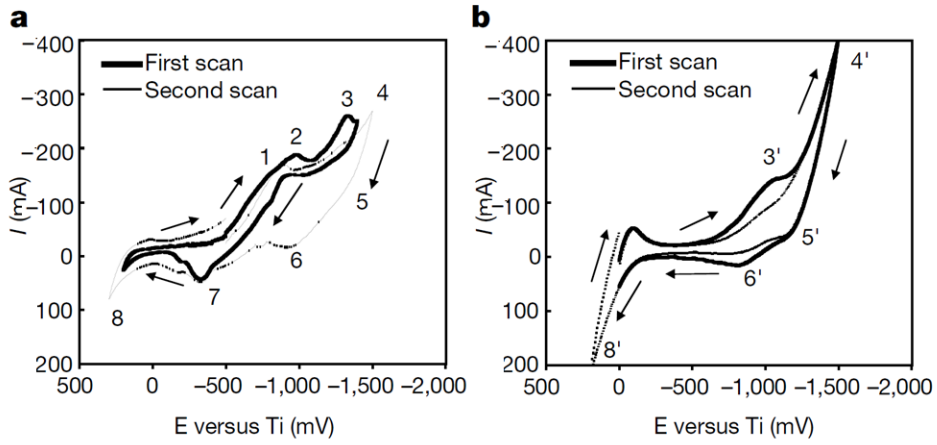

Figure 2.9 - Cyclic voltammograms of titanium foils in molten $CaCl_2$, scan rate: 10 mV s^{-1}, at 800 ˚C. (a) Oxide-scale-coated titanium foil. (b) As received titanium foil [39].

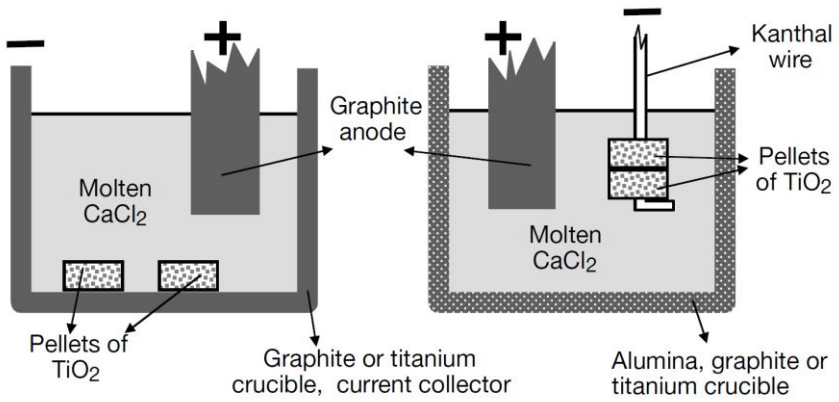

Figure 2.10 - Electrolytic cells for the reduction of TiO_2 pellets via the FFC Cambridge Process [39].

Schwandt and Fray [47] conducted an investigation to determine the kinetics of the electrochemical reduction of TiO_2 to Ti metal in molten $CaCl_2$. Partially reduced pellet samples were extracted by terminating the reduction process after specified reaction times. These samples were analysed using X-ray diffraction (XRD), scanning electron microscopy (SEM) and energy-dispersive X-ray spectroscopy (EDS). The experiment was split into three phases where chronoamperommety was performed. In the first phase, a potential of -2.5 V was applied for 8 h; in the second phase, the voltage was increased to -2.7 V and applied for 24 h; and in the third phase it was further increased to -2.9 V and left unchanged for 24 h. It was deduced that the reactions presented in Equations 2.12-14 took place in the first phase, which are attributed to a chemical reduction through calcium deposition. In the second phase, the chemical reaction illustrated in Equation 2.15 took place concurrently with the electrochemical reaction in Equation 2.16 at a lesser potential. The third phase involved the decomposition of $CaTi_2O_4$ and the formation of TiO, Equation 2.17. The TiO then further reduced electrochemically to produce titanium metal with solid solutions of oxygen in titanium, $Ti[O]_\delta$, where $\delta \rightarrow 0$. Thus, concluding that the reduction of TiO_2 to Ti in $CaCl_2$ is a combination of both, chemical and electrochemical processes.

$$4TiO_2 + Ca^{2+} + 2e^- \leftrightarrow Ti_3O_5 + CaTiO_3 \quad (2.12)$$

$$3TiO_2 + Ca^{2+} + 2e^- \leftrightarrow Ti_2O_3 + CaTiO_3 \quad (2.13)$$

$$2TiO_2 + Ca^{2+} + 2e^- \leftrightarrow TiO + CaTiO_3 \quad (2.14)$$

$$CaTiO_3 + TiO \leftrightarrow CaTi_2O_4 \quad (2.15)$$

$$2CaTiO_3 + 2e^- \leftrightarrow CaTi_2O_4 + Ca^{2+} + 2O^{2-} \quad (2.16)$$

$$CaTi_2O_4 + 2e^- \leftrightarrow 2TiO + Ca^{2+} + 2O^{2-} \quad (2.17)$$

$$TiO + 2(1-\delta)e^- \leftrightarrow Ti[O]_\delta + (1-\delta)O^{2-} \quad (2.18)$$

Studies by Dring *et al.* [48, 49] on thermally grown titanium oxide thin films, showed that four cathodic peaks associated with the electrochemical reduction of TiO_2 were observed. The cyclic voltammogram is shown in Figure 2.11. C0 is

associated with the decomposition potential of the salt and the deposition of Ca. C4 to C1 are attributed to the corresponding reactions in Equation 2.19. These were also characterised using XRD, SEM and EDS.

$$TiO_2 \overset{C4}{\rightarrow} Ti_3O_5 \overset{C3}{\rightarrow} Ti_2O_3 \overset{C2}{\rightarrow} TiO \overset{C1}{\rightarrow} Ti[O]_\delta \qquad 2.19$$

In the initial stages, the formation of $CaTiO_3$ through the chemical reaction of TiO_2 with Ca^{2+} and O^{2-} was observed. However, the titanate phase was not observed in the later stages with TiO. It was established that the diffusion of oxide ions in the product titanium-oxygen was the rate determining step. The formation of $CaTiO_3$ was due to the high concentration of oxide ions on the surface, and displaced the reduction reaction of Ti_2O_3 to TiO with reactions that possess significantly more negative potentials than predicted by the bulk oxide content of the salt. Under such high local oxide activity, the calciothermic reduction of titanium oxide, due to the formation of elemental calcium, was substantial. Thus, the reduction process was also determined to be a mixture of both, chemical and direct electrochemical.

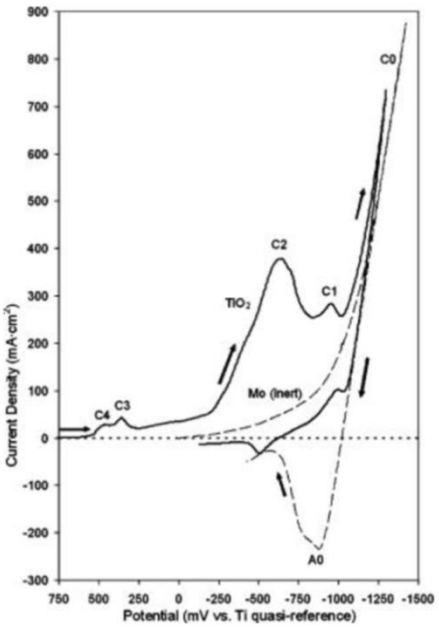

Figure 2.11 - Cyclic voltammograms of TiO_2 and inert electrode in $CaCl_2$, scan rate: 50 mV s^{-1}, at 900 ˚C [49].

An *in-situ* synchrotron diffraction study was conducted by Bhagat *et al*. [50], which shed more light onto the reduction pathway of TiO_2 to Ti in $CaCl_2$. The precursors in the study were in the form of pellets. The most important finding from this study was that it confirmed the presence of the $CaTiO_3$ titanate species, from the early stages of the process until almost the very end, before the final reduction of TiO, which was different from findings in previous works. Stoichiometric analyses of the results also showed that the formation of $CaTi_2O_4$ was due to the reaction of $CaTiO_3$ with TiO, rather than to a direct electrochemical reduction of the titanate species.

Many studies on the FFC Cambridge process were undertaken to develop the understanding of it and its different uses. Studies on the extraction of titanium from different pellet and sponge-like precursors [51-53] were carried out. Also, investigations using cheap precursors, such as titania dust and titanium-rich slug [54]. It was noted that some metallic impurities, such as aluminium and manganese, were partly or completely removed during the electrolysis. In addition, the FFC Cambridge process was successfully employed, using mixed oxide precursors, to produce NiTi [55-57], Ti-Mo alloys [58] and Ti-W alloys [59].

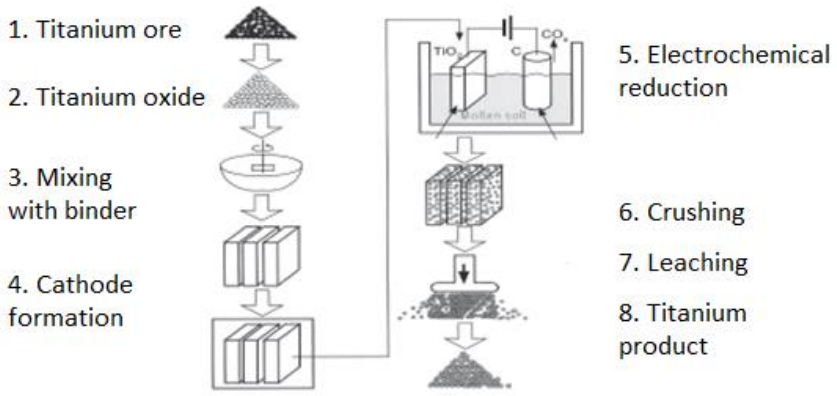

Figure 2.12 - Stages of the FFC Cambridge process [60].

The patent [43] on the FFC Cambridge process claims that a number of metals and semi-metals, such as Ti, Si, Ge, Zr, Hf, Sm, U, Al, Nd, Mo, Cr and Nd, can be produced with the starting material being the metal oxide, nitride, sulphide or carbide in a fused salt system. However, the majority of the research that has been reported so far has been on metal oxides, especially titanium dioxide. The FFC process for the production of titanium metal has been successfully scaled up, and is being industrialised by multiple developers. Figure 2.12 illustrates the simple stages that occur in the FFC Cambridge process for titanium metal production.

2.5.2 The three-phase interline (3PI)

The initial three-phase interline (3PI) model was proposed by Chen *et al.* [61]. It was developed by Deng *et al.* [62], and a comprehensive model by Kar and Evans [63] then followed. Any two phases are connected by a two-dimensional plane, and any three phases can only be connected by a one-dimensional point or line, the 3PI. The 3PI connects a conducting solid metal phase (SMP), an insulating solid compound phase (SCP) and a liquid electrolyte phase (LEP). In the case of a molten salt system, these are the metal phase (current collector), the metal oxide phase and the fused salt phase. This is illustrated in Figure 2.13.

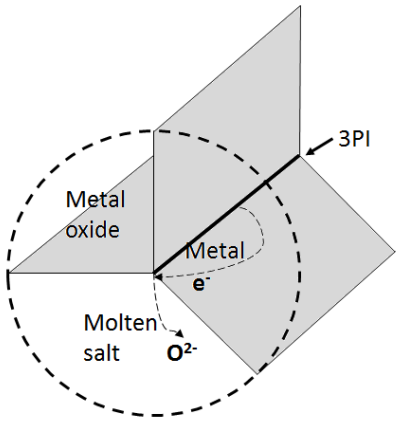

Figure 2.13 - Schematic representation of a three-phase interline (3PI) connecting a solid metal phase, a solid compound phase (metal oxide), and a liquid electrolyte phase (molten salt). The grey planes are the interlines between two neighbouring phases. At the 3PI, electron transfer occurs between the metal and the metal oxide and oxygen anion transfer between the metal oxide and the molten salt.

Along the 3PI, electron transfer occurs between the metal and the metal oxide, and oxide anion transfer occurs between the metal oxide and the molten salt. The 3PI is vital for the electrochemical reduction reaction. The longer the 3PI, the larger the current flow. As a reaction proceeds, the length and shape of the 3PI changes. The 3PI model, however, does not account for any inherent electrical conductivity of the oxide species. It also overlooks any changes in electrode morphology that takes place. Nonetheless, the model agrees with experimental findings to a reasonable level.

2.5.3 Challenges for electrochemical reduction in molten salts

There are a number of issues that arise when using a standard reactor setup, whether using electrode rods, porous pellets or sponge-type precursors as electrodes. In the case of reducing titanium oxide via the FFC Cambridge process, the current efficiency is quite low, 10-40%, to achieve sufficiently low oxygen content, 0.3%, in the final titanium product [51]. The current efficiency and the speed of the process must be increased in order to allow the electrochemical reduction of refractory metals in molten salts to be applied industrially [64]. This low efficiency and low speed of the process could be due to a number of reasons, such as diffusion, oxygen ionisation, electrolysis of molten salts, metal-to-oxide molar volume ratio, and transport characteristics of such systems. However, the most convincing explanations, from experimental results obtained from works on this matter are: the limited diffusion of the electrolyte within the precursor porous matrix, thus leaving the inner parts unreduced [65, 66]; and the anomalous electro-migration of oxygen vacancies in reduced metal oxides [67-69].

As a reduction reaction proceeds, the 3PI propagates, this is demonstrated in Figure 2.14, outward from the current collector to the inner parts of the precursor, and then inward from the reduced metallic surface towards the precursor's centre. The current increases initially, plateaus, then reduces until it stops [61]. This is due to the electrolyte not diffusing to the inner parts of the electrode, hence, the absence of the 3PI. This is due to the nature of the morphology of the oxide precursor, and to the change in density and structure of the materials reduced on the surface. For example, some metals, tend to have much higher densities than their oxides,

causing the metallic surface to collapse onto itself, creating a much denser morphology, hindering the diffusion of electrolyte [56].

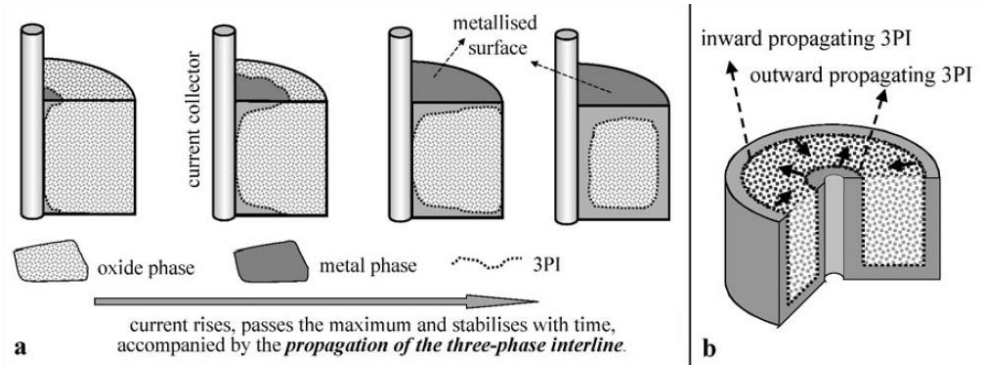

Figure 2.14 - Schematic of the 3PI propagation mechanism of a cylindrical metal oxide pellet. (a) Propagating from the current collector along the surface. (b) Propagating within the pellet [61].

Precursors in the form of oxide films, pellets or sponge-types are all porous. The size and interconnectivity of these pores affects the reduction process [51, 52]. When the metal oxide is reduced, some of the oxide ions transfer into the melt and migrate to the anode; however, some of them are trapped in the cathode's pores, as was observed by Dring *et al*. [49], where it was noted that the concentration of oxide ions at the surface of the electrode was higher than in the bulk molten salt. This can change the potential needed for the reduction significantly (refer to predominance diagrams, Chapter 4). It can also cause the formation of other metal phases (e.g. calcium titanate) due to the salt cation reacting with the oxygen ions on the surface. Ultimately, the oxide ions on the surface could block the current transfer, bringing the reduction process to a halt and leaving the inner parts of the metal oxide precursor unreduced.

Thus, creative new process designs must be developed to improve the efficiency and performance of the electrochemical reduction of metal oxides. One solution could be the use of a 'fluidised cathode' process [70], which was developed within the scope of this thesis.

2.6 'Fluidised bed' electrochemical processes

Numerous experimental, theoretical and review studies have been published on fluidised bed electrochemical processes [71-79]. The main advantages of employing fluidised bed electrodes are their large specific area (high specific productivity), and the free flowing character of their fluidised bed structure [80]. Applications include fuel cells, hydrogen peroxide synthesis [81, 82], water purification and organic electrosynthesis [83, 84]. In fuel cells, the fluidised particles are sometimes coated with catalyst to enhance the process [74]; their main uses are as fluidised bed anodes for carbonate fuel cells [85-88] and cathodes for alkaline fuel cells [73, 74, 89, 90]. In water purification a large tank containing a fluidised bed of particles is commonly used. These particles are charged cathodically by a feeder electrode, as the waste water flows through the tank, metal ions are absorbed on the surface of the charged particles. When these particles then come into contact with the working electrode, the potential drives a charge transfer reaction and the unwanted metals are deposited as discharge. The particles need replacing with fresh ones very often in such continuous processes [91].

Fluidised bed electrochemistry has been extensively studied and used in the recovery of copper and other metals from dilute solutions for environmental applications [92]. The metals to be eliminated are usually at low concentrations (less than 1 g l^{-1}) [80]. A schematic of the process is demonstrated in Figure 2.15. The metal recovery process operates in a similar way to fluidised bed electrodes in water purification technology, where the metal ions are attracted to the charged fluidised bed particles and form a layer on the outside of the particle. There is a continuous feed and recovery of the metal in dilute solutions by the introduction of small particles at the top of the bed and the removal of grown particles at the bottom of it [93, 94]. In this thesis, the particles themselves are reacted and reduced from the metal oxide to the metal phase.

Some disadvantages in using fluidised beds in pyroprocessing could be the difficulty of separating the materials from the salts, and the risk of creating small free flowing particulates of fission products that could escape, or get carried by gases.

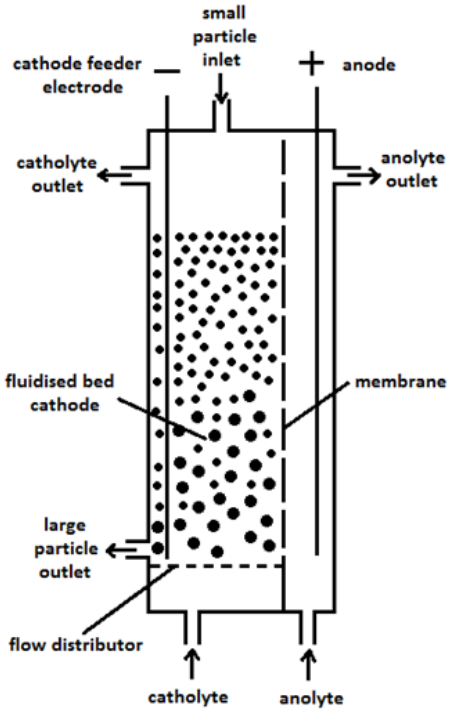

Figure 2.15 - Fluidised bed electrolysis reactor according to Fleischmann and Goodridge [95].

Fluidised bed electrodes have been studied and used industrially in various applications, though their definition is not precise; for example, sometimes they are reducing agents and other times they act as catalysts, yet they are still loosely called 'fluidised bed electrodes'. They have not been applied in molten salt electrochemical reduction processes, yet they may be a viable route to increasing the performance of such processes.

In the proposed arrangement, metal oxide particles are suspended in the molten salt via the use of an agitator (e.g. inert gas bubbling, stirring). An inert current collector, held at a suitable potential, is used, and an anode separated in its own compartment, to stop the reoxidation of the reduced metal particles. A schematic of the fluidised cathode process, and the different paths that a metal oxide particle could follow to be reduced, is illustrated in Figure 2.16. When a metal oxide particle is suspended and agitated in the fused salt, it comes into contact with the current collector, where a 3PI is instantly initiated, it is then either reduced fully or

partially, and it could get deposited on the electrode's surface or reflected from it back into the bulk salt. This process can be repeated multiples times for all particles until the reduction reaction reaches completion. The final product can then be retrieved from two areas: the deposit on the current collector's surface and the bottom of the reactor crucible, as particles sink and settle due to the high density of refractory metals.

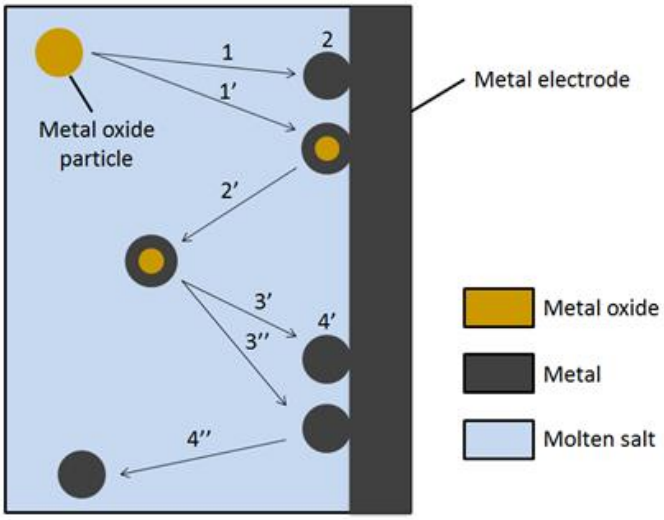

Figure 2.16 - Schematic of a fluidised cathode process in a molten salt showing various reaction mechanisms between particles in the melt and the electrode.

Studies on the electrochemical reduction of metal oxide particles on surfaces have recently been published [96-98]. However, these particles were small in size, not fluidised, and were used for thin film preparation. The fluidised cathode process is a larger-scale three-phase metal oxide to metal reduction process. A 3PI is continuously being created, every time an impending metal oxide particle comes into contact with the current collector. The matrix of the fluidised cathode also elevates the diffusion of electrolyte within the metal oxide particles, and of the oxygen ions within the electrolyte. Another proposed advantage of using a fluidised cathode process is that it would eliminate certain steps, in the preparation of the precursor and recovery of the reduced metal in the FFC Cambridge process, such as steps 3, 4 and 5 in Figure 2.12, with associated cost reductions.

2.7 Spent nuclear materials in molten salts

A significant amount of research on fission products in fused salts has been carried out over the past century. Molten salts provide a stable, proliferation resistant electrolytic medium for the dissolution, electro-plating, electro-reduction and refining of spent nuclear materials.

In an early study by Inman *et al*. [99], known quantities of UCl_3 were dissolved in an alkaline earth metal chloride eutectic, and a pure uranium working electrode was used. Following Equation 2.20, uranium was deposited on the working electrode. At current densities less than 100 mA cm^{-2}, the process had 100% Faradaic efficiency, based on the total deposit (adherent and non-adherent on the electrode surface) and the Nernst equation for the 3-electron-transfer determining step in Equation 2.20.

$$U \leftrightarrow U^{3+} + 3e^{-} \qquad 2.20$$

The cell potential at 452 °C was determined to be -1.398 V (vs. 1 wt% Ag/Ag^{+} reference electrode). It was also observed that some of the product was formed from a reaction with lithium in the salt, which resulted in a powdery deposit, and some of the product formed at lower potentials directly at the electrode resulted in a dendritic deposit. A similar, more recent study by Kuznetov *et al*. [100], using a tungsten working electrode, determined that the reduction potential for Equation 2.20, in a LiCl-KCl eutectic at 500 °C was ~ -1.5 V.

Most research on spent nuclear materials in molten salts was developed by the ANL [101-103]. Their molten salt electrorefiner, the schematic of which is presented in Figure 2.17, was a great innovation in nuclear molten salt technology. The electrorefiner comprises two cathodes: a solid steel/iron cathode, and a liquid cadmium cathode. Spent nuclear fuel is chopped and placed in a basket at the anode. This is then anodically oxidised. The actinides are reduced at the bottom of the electrorefiner at the liquid cadmium pool. Uranium is then electro-transported to the steel cathode, and a mixture of U, Pu and other actinides are transported to the liquid cadmium basket, and the Cd pool acts as the anode. Less noble fission products (e.g. alkali metals and alkaline earth metals) remain oxidised in the salt;

while the metals in the fuel cladding alloy and the noble fission products (e.g. ruthenium and palladium) are not oxidised and remain in the anode basket, or sink to the bottom of the electrorefiner as sludge in the cadmium pool. The deposit of uranium on the steel cathode was dendritic and sufficient for retrieval; however, once the process was applied to mixed fission products, especially plutonium, the morphology of the deposit was not adherent; therefore, the liquid cadmium cathode was introduced.

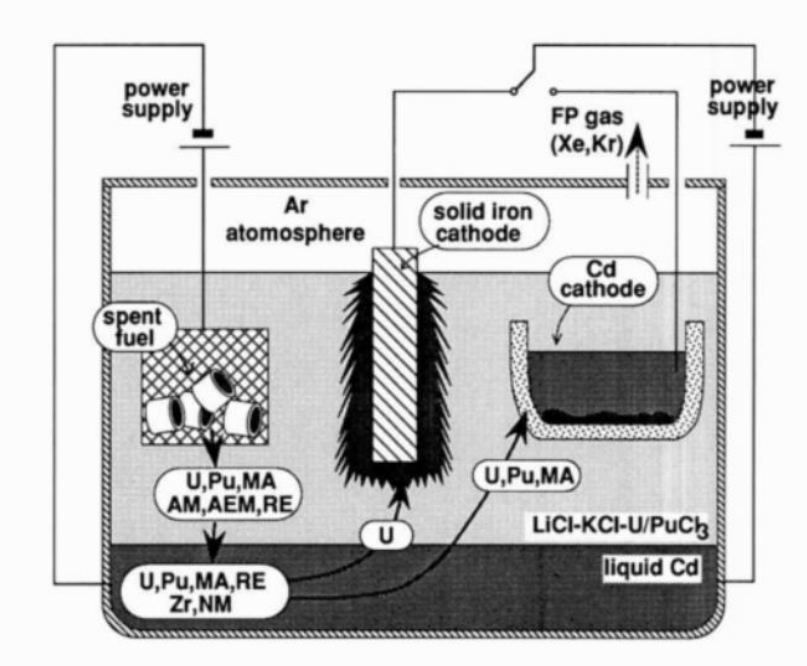

Figure 2.17 – Schematic of the electrorefining process developed by the ANL, operated at 500 °C, where AM = alkali metals, AEM = alkaline earth metals, MA = Np, Am and Cm, NM = noble metals, RE = rare earth metals, FP = fission product [104].

The electrorefiner was studied and developed further by Koyama *et al*. [19, 20, 104], they replaced the steel electrode with a pure iron cathode; and by other researchers [105, 106], who established the potentials at which the actinides and the cladding materials (e.g. Zr) are reduced from their chlorides, after they are anodically oxidised. These redox potentials are summarised in Table 2.4. One important thing to take notice of is that the potentials for the same redox reactions differ slightly from one study to another (e.g. for the U (III) / U(0) couple, from

Inman *et al*., Kuznetov *et al*. and Koyama *et al*.). This is due to the fact that cell potentials in molten salt systems are strongly dependant on the O^{2-} ion activities in the fused salts, which are difficult to control and are sometimes not accounted for after salt treatments have been applied. This phenomenon is discussed thoroughly in thermodynamically produced predominance diagrams, in Chapter 4.

Table 2.4 – Redox potentials of relevant elements in LiCl-KCl eutectic salt at indicated operating temperatures (V vs. Ag/Ag^+ reference electrode) [104-107].

	400 °C	450 °C	500 °C
U (III) / U (0)	-1.274	-1.233	-1.190
Pu (III) / Pu (0)	-1.591	-1.543	-1.497
Np (III) / Np (0)	-1.472	-1.434	-1.390
Am (II) / Am (0)		-1.592	
Zr (II) / Zr (0)		-0.693	

There are six types of Generation IV nuclear reactors and power plant under development, these are: the very-high-temperature reactor (VHTR), the sodium-cooled fast reactor (SFR), the supercritical-water-cooled reactor (SCWR), the gas-cooled fast reactor (GFR), the lead-cooled fast reactor (LFR), and the molten salt reactor (MSR). These designs and their operating conditions are summarised in Table 2.5. The fuel type used in the majority of these reactors is metal. Considering the fact that most reactors currently in use utilise metal oxide (MOX) fuel and most of the nuclear legacy waste is from MOX fuel, the conversion of metal oxides to metals is an important parameter for the development of safer and more efficient nuclear power generation. As discussed in Section 2.3, pyroprocessing of spent nuclear fuel provides an inherently safe technology that is also resistant to nuclear proliferation. Thus, the reduction of spent fuel metal oxides to metals is of importance to the development of civilian nuclear technology.

Table 2.5 – Generation IV reactor designs under development [108].

Reactor	Neutron spectrum	Coolant	Temperature °C	Fuel cycle	Fuel type	Size (MWe)
VHTR	Thermal	Helium	900 – 1000	Open	Oxide	100 – 300
SFR	Fast	Sodium	550	Closed	Metal/oxide	50 - 1500
SCWR	Thermal/fast	Water	510 – 625	Open/closed	Oxide	1000 – 1600
GFR	Fast	Helium	850	Closed	Metal	1000
LFR	Fast	Lead	480 – 800	Closed	Metal	20 – 1200
MSR	Fast/thermal	Fluoride salts	700 – 800	Closed	Metal*	1000

*The metal is dissolved in the fluoride salt (e.g. UF_4 and ThF_4).

Numerous studies on the electrochemical reduction of spent fuel oxides in molten salts have been published. In a study by Hermann *et al*. [109], crushed spent fuel was loaded into a stainless steel basket and submerged in molten LiCl-1 wt% Li_2O at 650 °C. A platinum anode and a Ni/NiO reference electrode were used. They determined that Equation 2.21, for the direct electrochemical reduction of UO_2 to U metal, took place at a potential of -2.40 V, and that the potential required for Li deposition from the salt, Equation 2.22, was -2.47 V. Thus, there was only a potential difference of 70 mV between the two reactions, which proved that the direct electro-reduction was difficult to achieve. However, the chemical reduction via Equation 2.23 provided supplementary help to the entire process. The only disadvantage being that the lithium evolution resulted in attacking the platinum anode and dissolving it. Choi *et al*. [110] managed to reduce 17 kg of UO_2 to U metal in LiCl-Li_2O. They concluded that a small pellet size, with a high anode surface area resulted in higher current efficiencies.

$$UO_2 \leftrightarrow U + O_2 \quad 2.21$$

$$Li_2O \leftrightarrow 2Li + \frac{1}{2}O_2 \quad 2.22$$

$$4Li + UO_2 \leftrightarrow U + 2Li_2O \quad 2.23$$

Studies on the reduction of U_3O_8 were also published. Seo *et al*. [111] conceived the main reduction potential for reducing U_3O_8 to U to be -2.27 V. In a further study by Jeong *et al*. [112], 20 kg of U_3O_8 were reduced successfully to U, with

more than 99% conversion. The reducing potentials seemed to vary from -2.47 V - -3.46 V. They concluded that an increase in the size of the pellets used in the cathode inhibits the diffusion of electrolyte to the inside of them, leaving them unreduced. This can be explained by the 3PI theory, described in Section 2.5.

In a study published by Sakamura *et al*. [113], UO_2 was reduced to U in both $CaCl_2$ and LiCl. The reduction in $CaCl_2$ appeared at < 0.6 V vs. Ca/Ca^{2+} at 800 °C. However, the conversion was not successful enough, as the diffusion of oxygen and electrolyte in the precursors appeared to be problematic. In LiCl, the reduction potential was < 0.15 V vs. Li/Li^{+} at 650 °C. The deposition of lithium was observed, and the process in LiCl had a higher current efficiency and better electrolyte diffusion in the precursor. Nonetheless, the reduction potentials in both systems were established to be very close to the salts' decomposition potentials.

Hur *et al*. [114] carried out the reduction of UO_2 to U metal in molten LiCl-KCl-Li_2O at 520 °C. The reduction potential was at -1.27 V vs. a Li-Pd reference electrode. They established that the reduction process was entirely caused by the chemical reduction reaction of UO_2 with Li. The contradictions in reducing potentials in the different studies is again due to the fact that the activity of O^{2-} ions in the molten salts is not accounted for, which can change the required potentials for certain reactions. This is explained in Chapter 4. When the reduction potentials and the salt's decomposition potential are close to one another, as is the case for the reduction of UO_2 in fused salt systems, the activity of O^{2-} ions also affects the kinetic pathways and rate determining steps of the process. However, the most important conclusion to draw from this, is the fact that the reduction of UO_2 to U metal, appears to take place in one overall direct 4-electron-transfer step, without any intermediate uranium oxides being formed (e.g. UO).

2.8 Summary

To set the theme for this research, a background review on nuclear energy and reprocessing technologies has been provided, molten salts and their applications have been covered, electrochemical reduction processes for metal productions in molten salts have also been covered, some fluidised bed electrode technologies

have been included, and finally the electrochemistry of spent nuclear materials in the literature was also included.

The electrochemical reduction of spent nuclear materials is an important development for civilian nuclear applications, especially for next generation power plants. Molten salts provide an excellent electrochemical route for the conversion of spent fuel to reusable metal fuel, as they are safer, smaller, and produce less waste streams than aqueous reprocessing routes.

The aim of this thesis is to develop the understanding of spent nuclear materials behaviour in molten salts, via thermodynamic and electrochemical techniques, and to investigate electrochemical reduction processes from metal oxides to metals, which can prove to be significant in future Generation IV nuclear power plants. New reactor designs are investigated as well, to improve the efficiency of such processes.

3. Experimental

This chapter is divided into three sections. The main electrochemical techniques used in experiments are described, the material characterisation techniques used are also described, and the experimental set-ups and designs are also covered.

3.1 Electrochemical techniques

The majority of the electrochemical studies in this work are conducted using controlled potential techniques. The chosen potential is set into the potentiostat's control, and in turn it supplies the required charge to reach this potential. The systems studied comprise an oxidised species O and a reduced species R, with redox reaction $O + ne^- \leftrightarrow R$, and associated reduction potential $E_{O/R}$.

3.1.1 Linear sweep and cyclic voltammetry

Linear sweep voltammetry (LSV) and cyclic voltammetry (CV) are two commonly used techniques, and are usually the first electrochemical characterisation processes used to study a system. Both have linear potential versus time functions. In CV, the potential is reversed and cycled between two set potentials at a constant rate (V s^{-1}). The current response occurs at an array of potentials at which the over-potential is increasing, and in the absence of other charge transfer reactions, this current reaches a maximum, then starts to decline until it flattens out. Figure 3.1 (a-b) shows the potential versus time waveforms for LSV and CV for a reversible (Nernstian) charge transfer reaction.

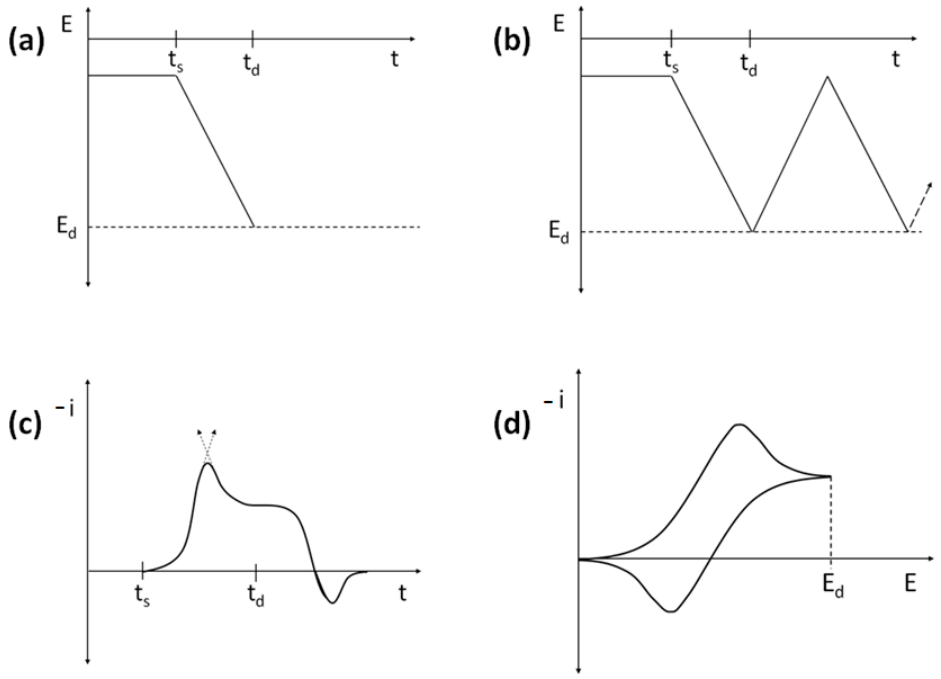

Figure 3.1 - (a) Potential vs. time waveform for linear sweep voltammetry (LSV). (b) Potential vs. time waveform for cyclic voltammetry (CV). (c) Current vs. time response corresponding to LSV. (d) Current vs. potential response corresponding to CV.

In Nernstian processes, electron transfer is rapid, thus the diffusion of the electro-active species into the electrolyte is rate determining. In irreversible processes, electron transfer is very slow, and quasi-reversible processes are both diffusion and charge transfer limited. In LSV and CV, the diffusion layer at the electrode surface is not allowed to reach equilibrium, due to the sweep rate of such scans.

For the reversible reaction O + ne^- ↔ R, the concentration gradient profile presented in Figure 3.2 depicts the depletion of O.

The flux of O into the electrolyte is directly proportional to the concentration gradient of O at any time; this is described by Fick's first law of diffusion, Equation 3.1, where the diffusion coefficient of O, D_O, is constant.

$$q(x,t) = D_O \frac{\partial C_O(x,t)}{\partial x} \quad 3.1$$

The flux is measured as current in the external circuit. Under fixed conditions of potential, the flux would diminish as the concentration gradient decreases due to diffusive mass transfer of O. In LSV and CV, the potential varies with time, thus giving O a concentration profile over time at the electrode surface. When the concentration profile reaches curve 4 in Figure 3.2, the concentration gradient is at its maximum, which gives rise to the current peaks in Figure 3.1 (c-d).

The main advantage of CV over LSV is that for Nernstian reaction O + ne^- → R, it shows the coupled peak for the reoxidation reaction R → O + ne^-, for the redox couple. It also gives better insight into whether a reaction is in fact electrochemically reversible, irreversible or quasi-reversible (i.e. only part of the reverse reactions steps can take place).

As the electron transfer process becomes slower, the cathodic and anodic peaks broaden and the separation between them becomes larger, due to higher over-potentials.

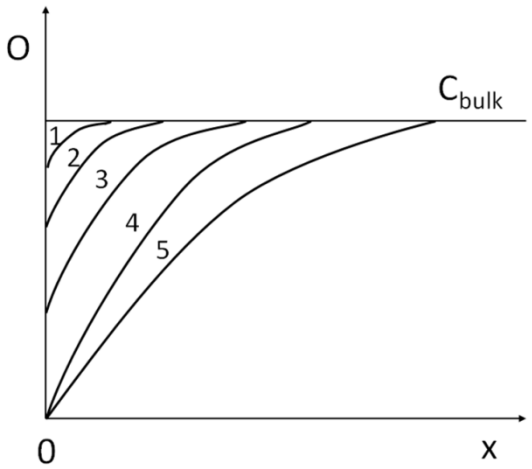

Figure 3.2 - Oxidised species (O) concentration vs. distance at different times, 1-5, during a linear sweep voltammetry.

3.1.2 Chronoamperometry

In chronoamperometry, a set constant potential is applied for a specified time period, and the current response is measured. For the redox reaction O + ne^- ↔ R, with reduction potential $E_{O/R}$, at potentials less than the reduction potential, no reaction would occur; however, at a range of potentials higher than $E_{O/R}$, the reduction reaction of O would occur rapidly, with associated charge transfer. The current versus time response for chronoamperometry is illustrated in Figure 3.3. The rate at which O moves to the electrode surface is limited by diffusive mass transfer, which the amount of current flux is proportional to.

The concentration profile of O over time, and the diffusion limited current i_D, can be described by Fick's second law of diffusion, Equation 3.2, where the boundary conditions are defined as: $\lim x \rightarrow \infty$, $C_O(x,t) = C_{bulk}$ and $C_O(0,t) = 0$.

$$\frac{\partial C_O(x,t)}{\partial t} = D_O \frac{\partial^2 C_O(x,t)}{\partial x^2} \qquad 3.2$$

The advantage of using chronoamperommetry over linear sweep techniques is that it allows for the electrode to reach polarisation, and it is a more adequate methodology for analytical characterisation.

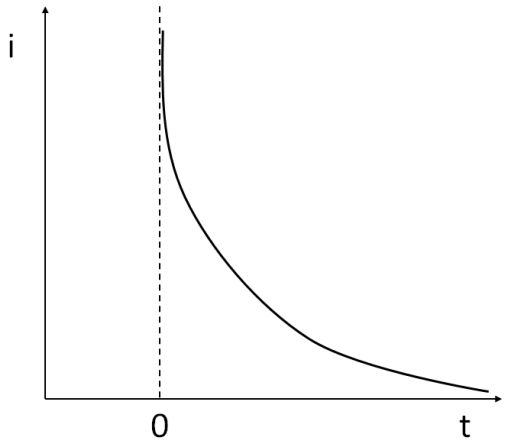

Figure 3.3 - Current vs. time response for chronoamperommetry.

3.2 Material characterisation techniques

Following the electroanalytical techniques, material characterisation techniques were used to identify materials and phases before and after experiments were conducted. The three techniques used here are: X-ray diffraction for phase identification; scanning electron microscopy, coupled with energy dispersive x-ray spectroscopy, for microstructural measurements and phase identification; particle size analysis for size distributions of powder particles.

3.2.1 X-ray diffraction

Powder X-ray diffraction (XRD) is a very important tool for chemical analyses to provide evidence for electrochemical processes. The basic principles behind it can be described using Bragg's law, Equation 3.3, where n is the order of diffraction (normally this is unity), λ is the wavelength of the radiation, d is the inter-planar spacing of the crystal being analysed, and θ is the angle between the diffracted and incident ray and the crystal plane. This is illustrated in Figure 3.4.

$$n\lambda = 2d \sin\theta \qquad 3.3$$

When n is 1, the scattered beams from successive planes will each travel a distance differing by one wavelength. The beams will constructively interact registering an intense diffraction beam at the X-ray detector.

The apparatus used for XRD analysis is a Stoe StadiP capillary geometry system with a molybdenum source. Eva (Bruker) software, coupled with Mercury software, and database from the Royal Society of Chemistry (ICSD data base) were used to analyse and match the diffraction data for phase identification with patterns from the literature. The sample to be analysed was ground into fine powder and placed inside a 0.3 or 0.5 mm in diameter capillary, which was then sealed to protect sensitive samples from air and moisture. The capillary was mounted in a sample holder and was continuously rotating when measurements were taken. Typical parameters used were: a measurement angle of 2 – 50 ° with 0.5 ° step, and 20 s $step^{-1}$.

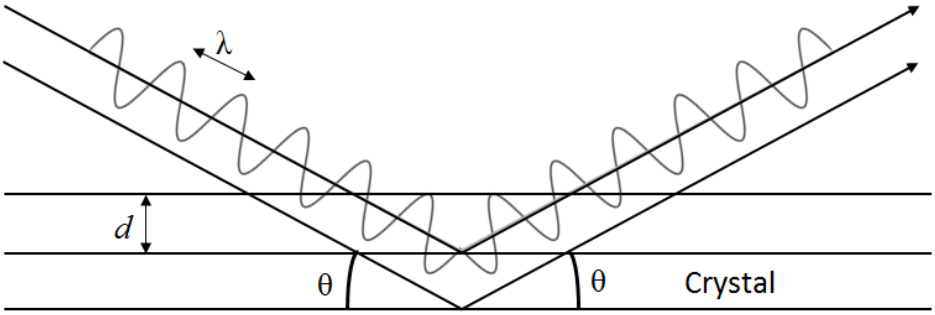

Figure 3.4 - X-ray diffraction schematic of a crystal.

3.2.2 Scanning electron microscopy and energy dispersive X-ray spectroscopy

Samples were analysed with scanning electron microscopy (SEM) using a Carl Zeiss XB1540 apparatus, which is also equipped with a "cross-beam" focused ion beam (FIB) microscope for microscopic milling of surfaces. Samples in the form of fine powders were mounted simply by placing them on carbon adhesive discs that are mounted on the SEM stubs. Working electrodes and current collectors were mounted in epoxy resin. They were placed in a desiccator that is fitted with a vacuum pump and left for about 10 minutes to allow the resin to penetrate through the pores in the samples and to remove air bubbles in the epoxy. After drying, the sample was ground using silicon carbide grinding paper, starting with a 220 grit, the sample was ground until smooth, then ground again in a direction perpendicular to the previous one using a 500 grit. This was repeated using 800, 1200, 2400 and 4000 grits. The samples were inspected under an optical microscope throughout the grinding procedure. Before placing a sample in the SEM chamber, its surface was gold coated, using a gold coating machine.

Quantitative analyses were performed using X-ray energy dispersive spectroscopy (EDS), which was calibrated against a cobalt standard before every use. It was typically operated at ~20.00 keV and ~15 mm working distance.

3.2.3 Particle size analysis

Samples were analysed using a Beckman Coulter LS13320 laser diffraction particle size analyser. Laser diffraction correlates the patterns of scattered light and its

intensity at different angles to the particle size distribution of a sample. The apparatus is fitted with a PC for data collection, which provides particle size distribution data using the Mie theory (this is explained in the Beckman Coulter LS13320 manual which can be found online). Small powder samples were dispersed in deionised water in a special sample holder through which laser is scattered and detected.

3.3 Experimental design

The experimental set-up was designed to exploit the physical properties of the salt eutectic, mainly the low melting point of the LiCl-KCl eutectic (352 °C). This allowed the use of borosilicate glass as the cell wall material, which was beneficial as it provided visual access to the process.

The rig consisted of three compartments. The crucible: a disposable container placed inside the cell envelope which contains the molten salt; the envelope: the outer container of the electrochemical cell, which seals the process from the outer environment and was used as a safety precaution to contain the molten salt in case of crucible breakage; the heating element: two different heating methods were used, one employing a thermostatic salt bath, and one using a vertical tube furnace.

Although the reaction cell was sealed with a constant stream of argon passing through the top part of it, the experiments utilising the thermostatic salt bath were carried out inside a dry glove-box, Figure 3.5. This limited water, or any other types of contaminants, from entering the reaction vessel. The glove-box was made of Perspex, providing extra shielding when handling uranium, and also protected against heat given off from the rig.

Figure 3.6 illustrates the general full schematic of the experimental rig. There were two loops; a closed one where the air inside the glove-box was pumped through two desiccant tubes in series, to absorb water vapour and reduce humidity, then was recycled back into the glove-box; and an ‘open loop’ where dry argon was passed to the inside of the reaction cell, via a flowmeter creating an argon blanket at the top of the cell, and then out of the reaction cell and the glove-box into a fume cupboard, whilst passing over two Dreschel bottles to prevent any back flow. There were two cooling fans at opposite corners of the glove-box to aid the distribution of

temperature, and prevent the Perspex walls from reaching critical heat. Thermocouples were placed in all sections of the rig to monitor the temperature. There was also a camera mounted and pointed toward the reaction cell, ready to record any visual activity.

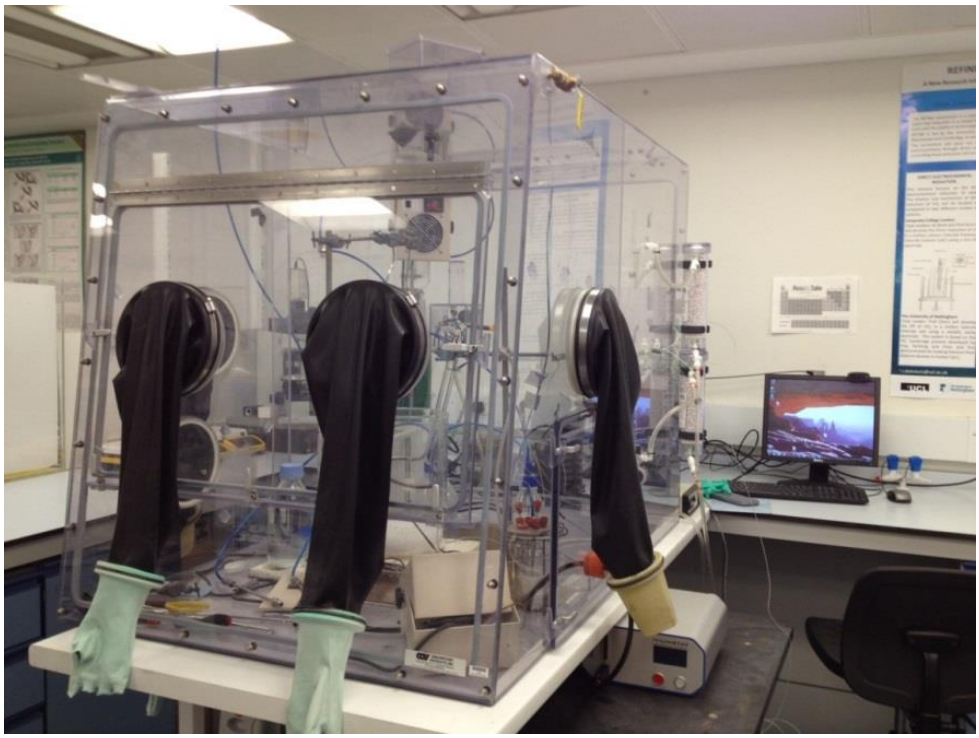

Figure 3.5 - Perspex dry glove-box containing molten salt electrochemical cell.

3.3.1 Heating and temperature control

Two methods were used for heating the electrochemical cell components to the desired temperatures. One method uses a thermostatic salt bath, similar to the arrangement used by Inman and Bockris [115], which benefits from visual accessibility throughout experiments. The other uses a typical vertical tube furnace, which is more practical in terms of time and reliability; however, one cannot inspect the process visually whilst experiments are running.

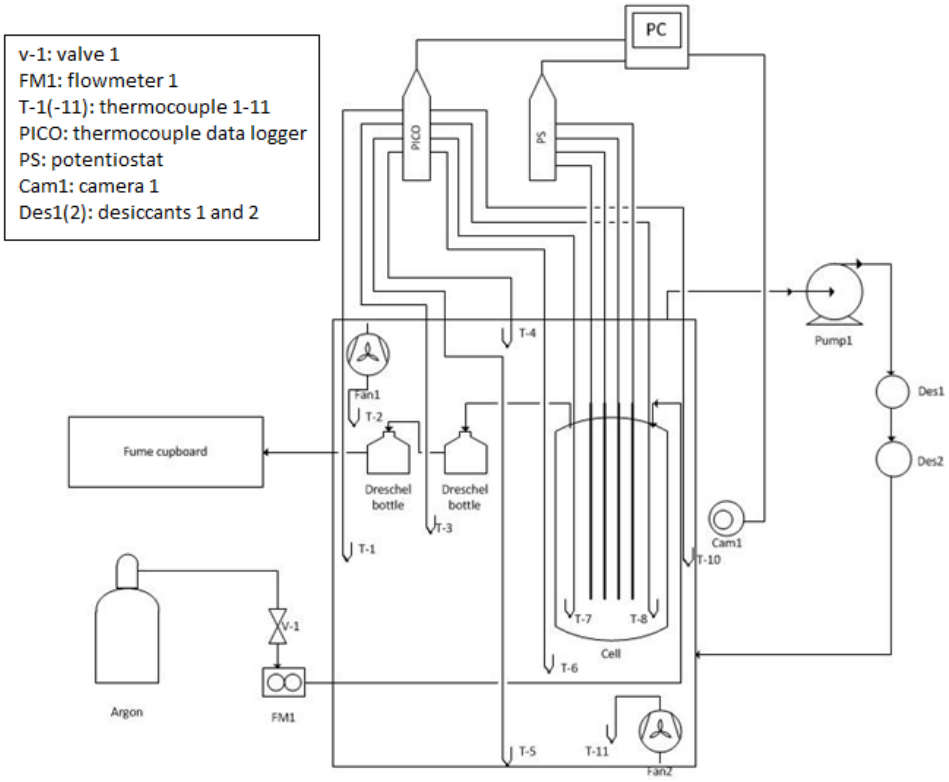

Figure 3.6 - Schematic of the rig set-up, showing components inside and outside the dry glove-box.

3.3.1.1 Thermostatic salt bath

The thermostatic salt used was a $NaNO_3$-KNO_3 eutectic. It was kept and melted in a 5 L borosilicate glass heavy-duty beaker, to maintain visibility. Corrosion and attack effects from the salt on the glass were negligible [116], hence the container beaker could be used for a large number of experiments. The salt eutectic, once molten, is homogeneous in temperature and has the ability to store energy for a long period of time [117]. The eutectic is equimolar and has a melting temperature of 220 ˚C, as illustrated in the phase diagram in Figure 3.7. It has a latent heat value of 97 J g^{-1}. Information on its viscosity and specific heat values at different temperatures can be found in the works by Coscia *et al*. [118] and Nissen [119].

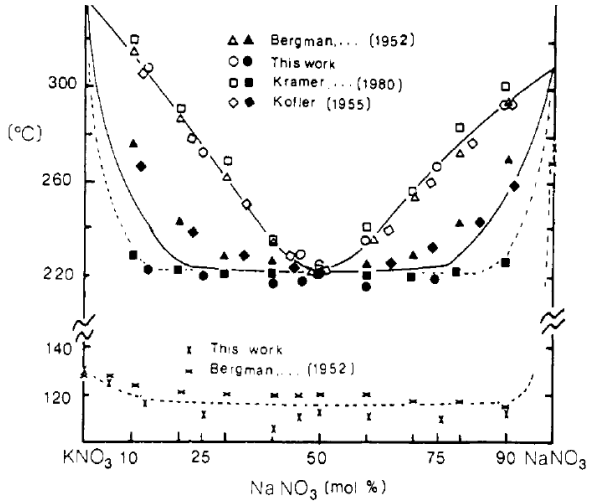

Figure 3.7 - Phase diagram for $NaNO_3$-KNO_3 eutectic [120].

To heat up the thermostatic salt bath an immersion heater was used. The tubing material for the immersion heater was silica glass, which withstands higher temperatures and has higher mechanical integrity when compared to borosilicate glass. The dimensions of the immersion heater are shown in Figure 3.8. The reactor cell, when placed in the thermostatic salt bath, is encircled by the bottom round side of the immersion heater, Figure 3.10.

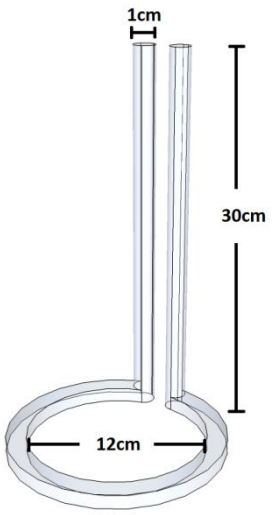

Figure 3.8 - Dimensions of silica tubing for immersion heater.

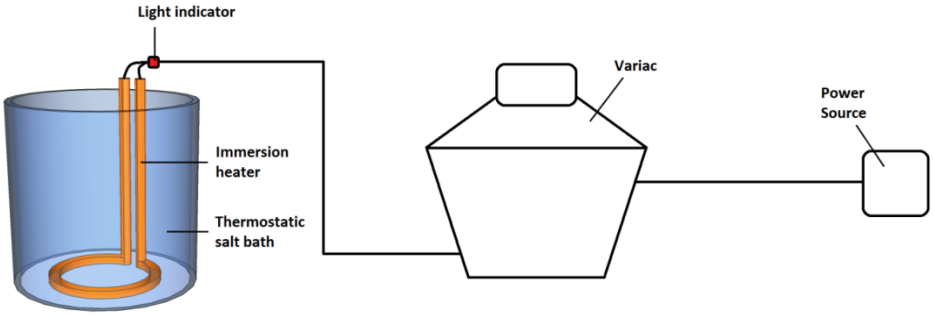

Figure 3.9 - Schematic for heating apparatus.

Nichrome wire, 0.46 mm thickness and 4 m long, was coiled up and put through the silica tubing. This was then connected to a power source and voltage was passed through it via a variac, as illustrated in Figure 3.9. A small light bulb was also connected to the top of the immersion heater, to indicate when the power was on, for safety. Calculations were carried out, Appendix A, to estimate the voltage needed to be passed through the nichrome wire to reach specific temperatures of the thermostatic salt bath. This was set at the variac and presented in Table 3.1. Nonetheless, these are estimates as the heat loss to the environment was not accounted for. Thus, these calculated values provide an indication of the voltage needed, and during experimentation the heating is monitored, via the use of thermocouples, to be able to control the temperatures precisely.

Table 3.1 – Guideline for voltage required to achieve temperatures of 3 kg of $NaNO_3$-KNO_3 thermostatic salt bath after 1.5 h.

T (˚C)	100	200	300	400	500	600
V (V)	44	65	90	102	113	123

Thermocouples were placed in different positions in the rig, as illustrated in Figure 3.6. There were two inside the main rig testing area: one inside the crucible of the cell, to monitor the operating temperature, and one inside the thermostatic salt bath beaker. The operating temperature could then be adjusted accurately via the variac. In practice, the voltages required were much higher than the calculated ones, due to losses of heat to the environment. There were more thermocouples placed around the rig, to monitor the process and prevent reaching critical temperatures. These

were placed at the front, back, sides, roof, bottom and corners of the Perspex glove-box.

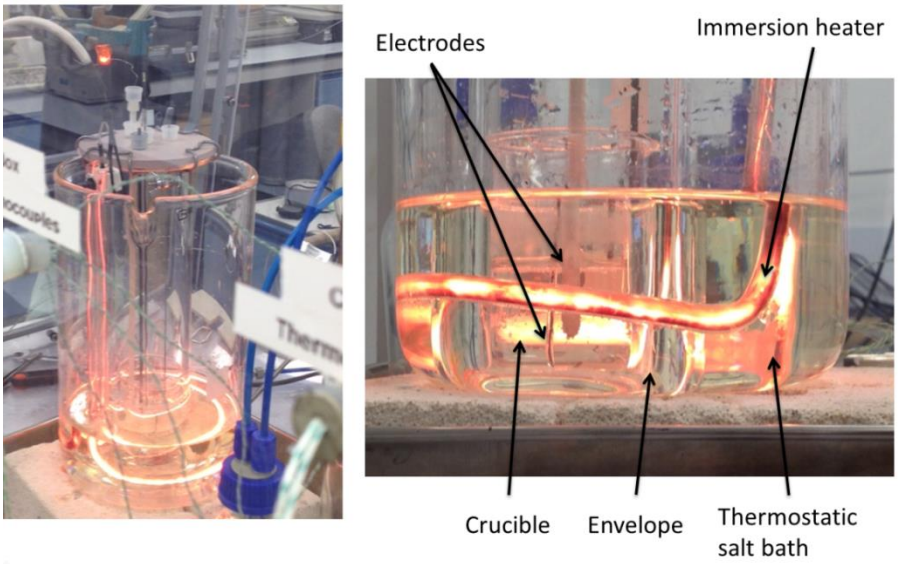

Figure 3.10 - Immersion heater rig.

3.3.1.2 Vertical tube furnace

A vertical split-tube furnace was used to provide heat to the electrochemical cell (CSC 12/90/300 V furnace, Lenton). This was custom built to fit the reaction cell. It provided a faster heating rate and a stable environment for electrochemical processes. Measuring the temperature inside the crucible via a thermocouple showed that the difference between the salt temperature and the set temperature of the furnace is ~10 °C. This furnace does not afford optical access to the inside of the cell.

3.3.2 Electrochemical cell

The electrochemical cell was mainly constructed from borosilicate glass. It consists of the envelope, the crucible, a cell head and electrodes. The crucible was a 250 ml high-form borosilicate glass beaker (Schott Duran). It was treated as dispensable, due to breakage caused by salt shrinkage as it solidifies. The crucible is placed inside the envelope. The envelope was a tall borosilicate glass beaker with a flange (GPE Scientific Ltd), and was designed to the specifications presented in Figure 3.11.

Machinable ceramic was used for making the cell head (Unfired Pyrophylite, Ceramic Substrates and Components Ltd). It was supplied in the form of a tube with 12 cm diameter. Discs of 0.5 cm thickness were sliced off the tube, then holes were drilled through them with the desired dimensions and arrangement. The cell head was then baked in a furnace (Vecstar VF1), at a ramp rate of 50 °C h^{-1} until 400 °C, followed by 100 °C h^{-1} until 1000 °C, then left at 1000 °C for an hour. Schematics of the two different cell head arrangements used are illustrated in Figure 3.14. Silicone rubber suba-seals (Sigma-Aldrich) were used to seal the holes in the ceramic head, and the required electrodes and thermocouple were pushed through them. They can withstand temperatures of up to 200 °C continuously or 400 °C intermittently, and it is easy to move the electrodes up and down through them. A PTFE gasket (Sci-Labware) was placed between the envelope flange and the cell head, which provided sealing from the environment. They were held together using a metallic clamp (Sci-Labware). A schematic of the electrochemical cell is illustrated in Figure 3.12.

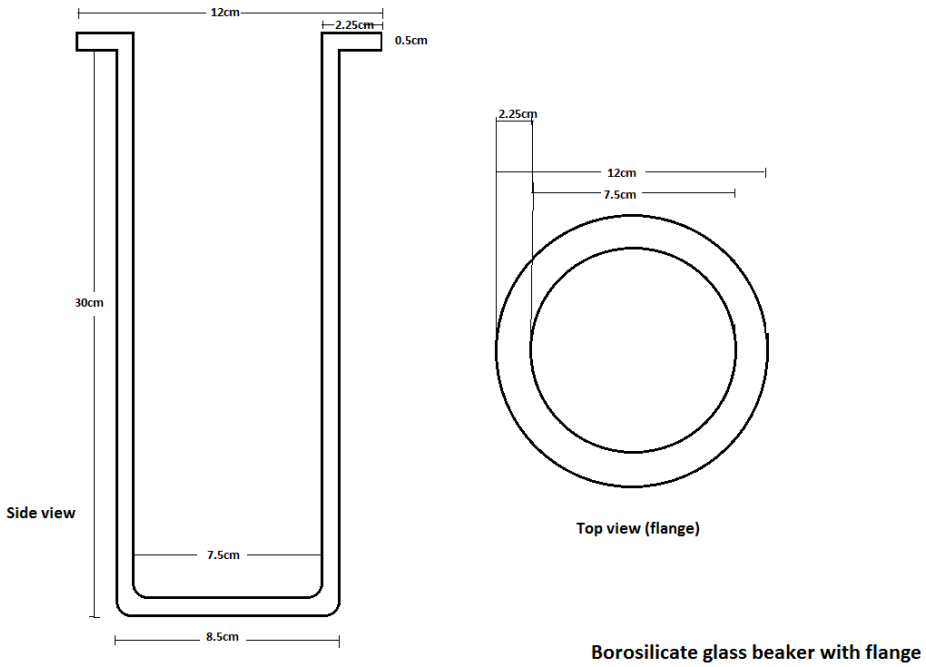

Figure 3.11 - Dimensions of cell envelope.

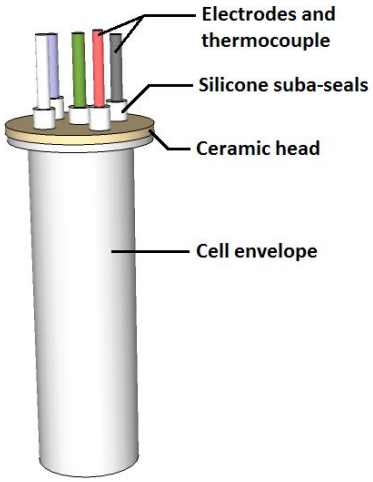

Figure 3.12 - Electrochemical cell schematic.

Two different electrolytic cells were used, the schematic for each is presented in Figure 3.13 and the cell head arrangements in Figure 3.14. A K-type thermocouple (Omega), placed inside a one end closed glass tube was always immersed in the salt to monitor the temperature.

For the fluidised cathode set-up, the cathode comprises particles of metal oxide that are agitated/suspended in the salt eutectic melt, and a pure metal rod current collector, that has a glass sheath around part of it so that 4 cm of it were always immersed in the salt, taking into account the movement of the surface of the melt as the salt was being agitated. The anode was separated in its own compartment to avoid reoxidation of the reduced particles. A glass frit (porosity 2, 15 mm in diameter, VWR International) was used to allow for the flow of salt ions. This frit was fitted with a glass tube that contained the anode. The anode compartment has an opening at the top to allow for gases to escape. The particles in the crucible were agitated via the flow of argon (99.998% purity, BOC) through the melt. It was bubbled via a ceramic tube (5 mm internal diameter, Alsint).

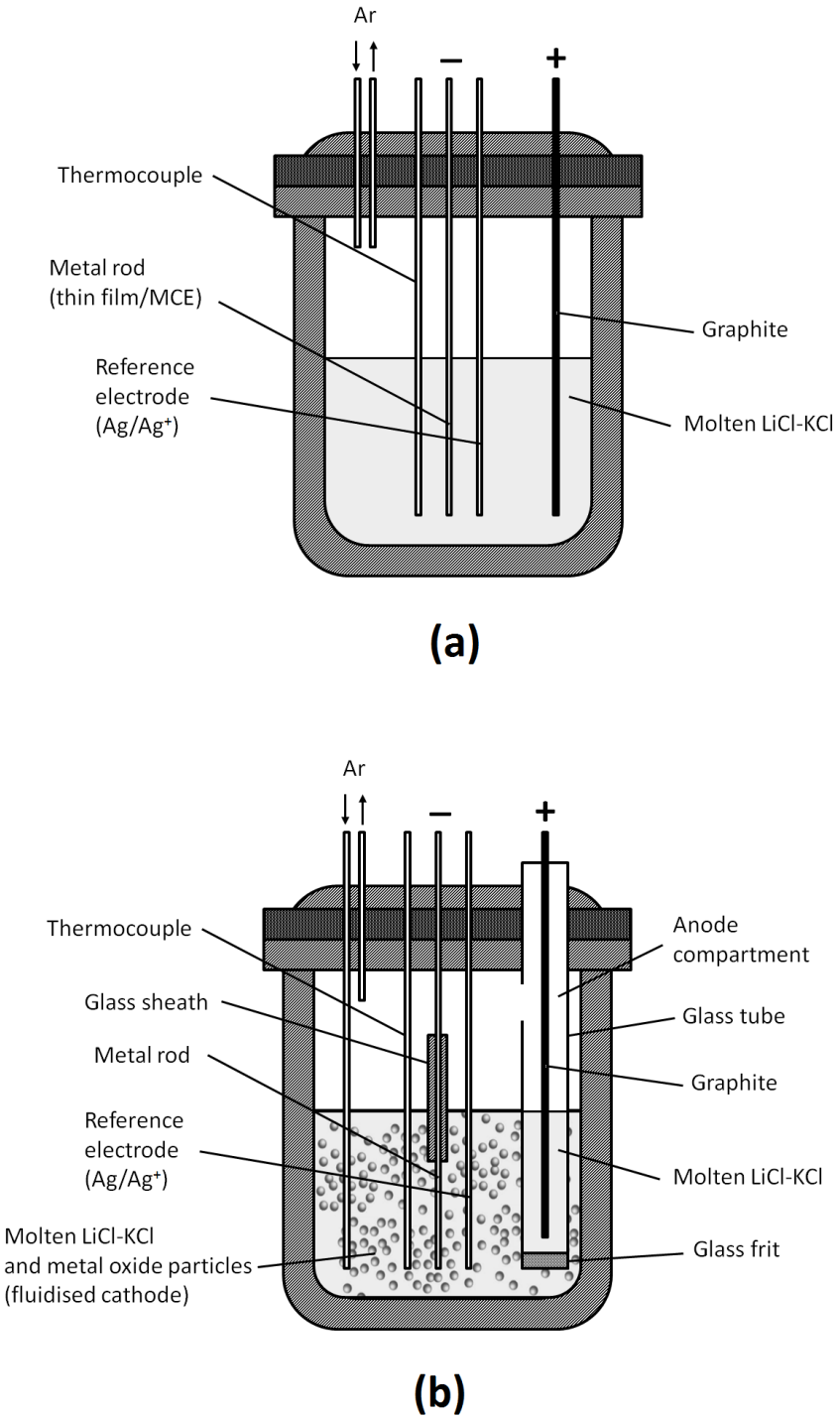

Figure 3.13 - Electrolytic cells. (a) For a typical cell set-up for the electrochemical reduction of thin films or metal cavity electrodes (MCEs), (b) for the electrochemical reduction of metal oxide powder using the fluidised cathode method.

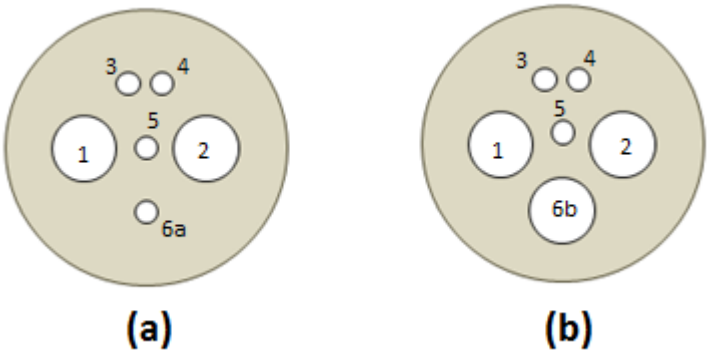

Figure 3.14 - Ceramic cell heads hole arrangements. (a) For a typical cell set-up. (b) For a fluidised cathode set-up. 1 is the argon inlet, 2 is the argon outlet, 3 is for the reference electrode, 4 is for the working electrode or current collector (also used for the sacrificial electrode in pre-electrolysis), 5 is for the thermocouple, 6a for the anode, and 6b for the anode compartment containing the anode.

3.3.3 Electrodes

The electrode materials needed to possess mechanical integrity, not contaminate the salt and withstand the relevant temperatures. They were immersed in the salt eutectic melt and held in position via the silicone suba-seals. The suba-seals are electrically insulating, and seal the cell from the outside environment. A three electrode system was employed as required, as it provides the same frame of reference for all the electrochemical experiments involving potential measurements. All electrodes were 32-35 cm in length.

3.3.3.1 Reference electrode

The reference electrode used was a Ag/Ag+ electrode [121]. Borosilicate glass tubes were used as the membrane sheath for the electrode; they have one closed end and one open end with 3 mm internal diameter and a 1 mm wall thickness (to aid transport). Silver wire with a 0.203 mm diameter (99.95% metal basis, Alfa Aesar) was used. A silicone suba-seal was used to seal off the open end of the glass tube, Figure 3.15.

The preparation of the reference electrode was conducted inside an argon glove box. Initially, the glass tube was baked for a few hours, at 200 ˚C, to get rid of any

residual moisture. Using treated dry salt, prepared as detailed in Section 3.3.4, 10 g of LiCl-KCl eutectic was mixed with 0.1 g AgCl (>99% purity, Sigma Aldrich). The mixture was then heated until molten to ensure homogeneity. After cooling down, the 1wt% AgCl in LiCl-KCl was ground to fine powder. The silver wire was then placed inside the glass tube and pushed all the way to the bottom. Using a small funnel, 1 g of the 1 wt% AgCl in LiCl-KCl was put inside the glass tube. The tube was then sealed using a silicone suba-seal and the top of the silver wire was pushed through it, exposing it for electrical conduction. A cross-section of the reference electrode showing its configuration is illustrated in Figure 3.15. When running an experiment, the reference electrode was immersed in the molten LiCl-KCl eutectic, the salt inside the tube also melts and the reference electrode is operational. Whenever Ag/Ag^+ electrode is mentioned in this thesis, it contains 1 wt% AgCl.

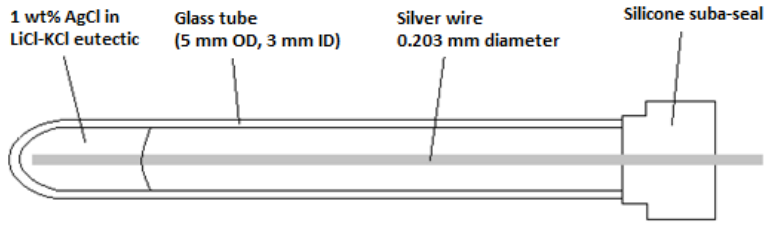

Figure 3.15 - Cross section of the Ag/Ag^+ reference electrode.

When electrochemical measurements are taken, the silver wire reacts with the chloride salt in the melt inside the glass membrane, according to the reversible redox reaction in Equation 3.4, creating a standard potential reference.

$$AgCl + e^- \rightleftharpoons Ag + Cl^- \qquad 3.4$$

3.3.3.2 Counter electrode

A high density graphite rod was used as a counter electrode, 3.05 mm in diameter (99.9995% metal basis, Alfa Aesar). The graphite rods were reusable if good mechanical integrity were maintained. They were cleaned thoroughly with acetone

before each use, and were heated via torch flame until glowing red, to remove any residual water from them.

3.3.3.3 Working electrode

All metal oxide powders used, WO_3 and UO_2, are described in Chapters 5 and 6 respectively. Their characterisation is included as well. Three types of working electrodes were used; thin film electrodes, metallic cavity electrodes, and fluidised cathodes. They are summarised as follows.

a) Thin film electrode

A thin layer of oxide was thermally grown on a tungsten rod, 1.5 mm in diameter (99.95% metal basis, Alfa Aesar). This was done by thermally oxidising the electrode in air at a temperature ramp rate of 250 °C h^{-1}, then holding the temperature at 700 °C for 2 h. The rod's surface became yellow/green in colour, indicative of the formation of WO_3.

b) Metallic cavity electrode (MCE)

Metallic cavity electrodes [122-126] were made using a 0.5 mm thick molybdenum sheet (Sigma-Aldrich, 99.9% purity). The sheet was cut into 5 mm wide and 6 cm long strips. Holes, or cavities, of 0.4 mm diameter were drilled at one end of the strips, as shown in Figure 3.16 (b). These strips were then attached to a tungsten rod using a molybdenum wire. When experiments were run, it was ensured that only half of a strip was immersed in the molten salt, with all the cavities exposed to the electrolyte, but keeping the wire and the tungsten rod above it. Before conducting electrochemical tests, the cavities were filled with fine powder of the desired metal oxide to be reduced, using two glass slides and a 'finger pressing' technique (here, a glass slide was placed on the desk, some powder was place on top of it, the MCE was places on top of the powder allowing it to fill the cavaties, some more powder was placed on top of the MCE, then a glass slide on top. Carefully using fingers, the two glass slides were pressed together to fill the cavities with dense powder).

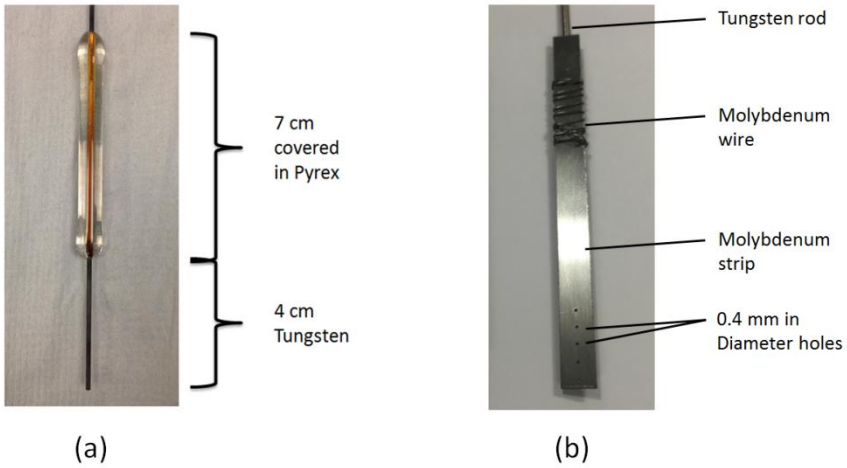

Figure 3.16 – (a) Working electrode for fluidised cathode set-up. (b) Metallic cavity working electrode (MCE).

c) Fluidised cathode

For the fluidised cathode set-up, the cathode compartment comprises metal oxide particles that were suspended in the fused melt via bubbling argon, and a current collector. The current collector was a tungsten rod, 1.5 mm in diameter (99.95% metal basis, Alfa Aeser) that has a Pyrex sheath around it, Figure 3.16 (a), to make sure that 4 cm of the electrode is always, and only, immersed in the salt during experiments. This is to guarantee that all current response effects are due to particle-electrode interactions, and not to the electrolyte's surface vibrating through agitation.

3.3.4 Electrolyte and cell atmosphere handling

All preparation steps were carried out under a sealed argon atmosphere, in an argon glovebox (MBRAUN), where O_2 levels were always kept at less than 0.5 ppm, and water levels were also kept at less than 0.5 ppm. Anhydrous lithium chloride (ACS reagent, ≥99.0% purity, Sigma-Aldrich) and potassium chloride (≥99.5% purity, Sigma-Aldrich) were used for the electrolyte. The salt was dried in a vacuum oven at 200 ˚C for 24 h to get rid of any residual moisture, then 59-41 mol% LiCl-KCl

were mixed together. The salt was placed in the crucible, which was placed inside the envelope, then, with the electrodes in place, the cell was sealed. This was then transferred to the rig, to be heated, and the argon inlet and outlet were connected. During experiments, a constant stream of argon was applied, creating a blanket at the top of the reaction vessel.

Cyclic voltammetry measurements were carried out on a LiCl-KCl salt eutectic at 450 °C using a pure tungsten electrode as the working electrode, a graphite rod as the counter electrode, and a Ag/Ag^{+} reference electrode. The scan rate applied was 50 mV s^{-1}, scanned from 0 V to -3 V to 3 V and back to 0 V. The cyclic voltammogram produced is shown in Figure 3.17. It illustrates the potential window of the LiCl-KCl salt eutectic. As can be seen, there are no significant current peaks between the potentials 1.1 V and -2.6 V. Thus, between these two potential values lies the salt's potential window. At 1.1 V chlorine gas evolution starts and it reaches its maximum level at about 2.6 V. At -2.6 V lithium metal formation starts. From predominance diagrams of LiCl-KCl eutectics, Chapter 4, one can deduce that lithium metal formation starts before potassium metal formation. There is a peak on the left hand side of the diagram, in the positive direction, this is due to the fact that when the potential is swept in the positive direction lithium is oxidised back into its ionic form. This does not appear on the right hand side of the graph, where chlorine gas evolution takes place, as the Cl_2 molecules evolved leave the melt. Again, if the potential window of LiCl-KCl from this cyclicvoltammogram is compared to that established in the predominance diagram, noting that here the potential is shifted to the right, as it is against a Ag/Ag+ reference electrode and the predominance diagram is against the standard chlorine electrode, one can see that the width of the window is about the same, 3.7 V. This supports the validity of the predominance diagram for predicting the stability of the electrolyte. As for most molten salts, the potential window of the LiCl-KCl eutectic is very wide, which allows for flexibility in conducting electrochemical reactions.

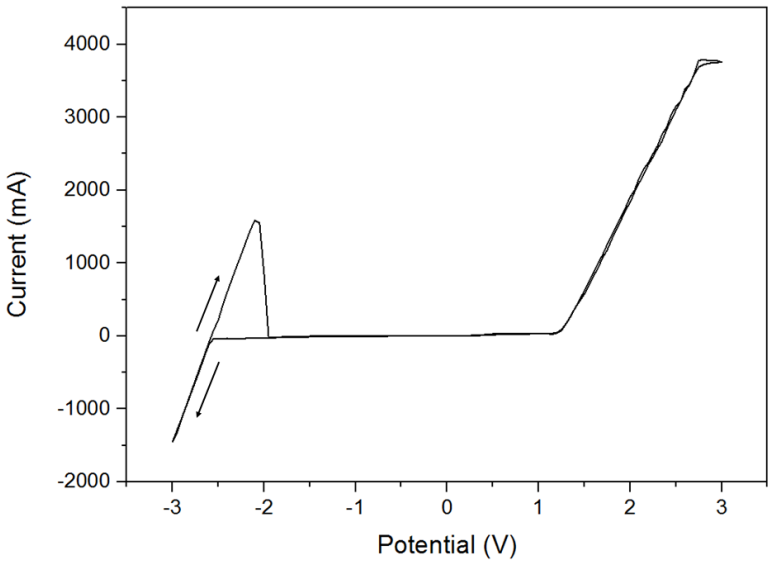

Figure 3.17 - Cyclic voltammogram showing the potential window of LiCl-KCl eutectic at 450 °C, scan rate 50 mV s^{-1}, and reference electrode: Ag/Ag^{+}.

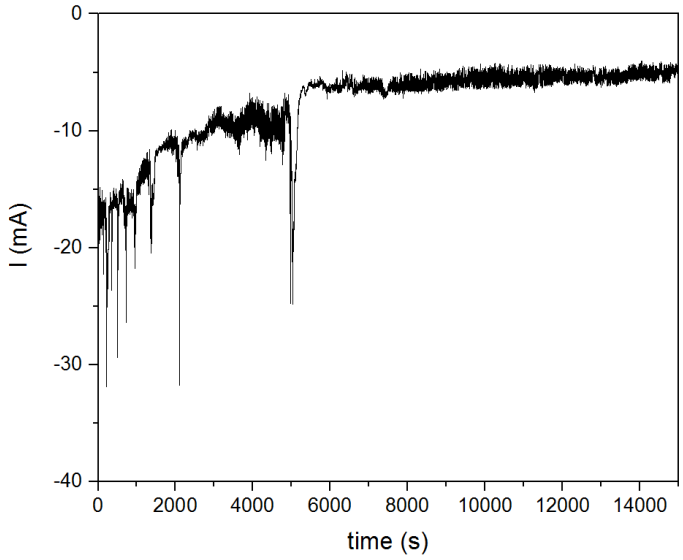

Figure 3.18 - Chronoamperogram showing a typical pre-electrolysis of LiCl-KCl eutectic at 450 °C, set voltage: -2.300 V, and reference electrode: Ag/Ag^{+}.

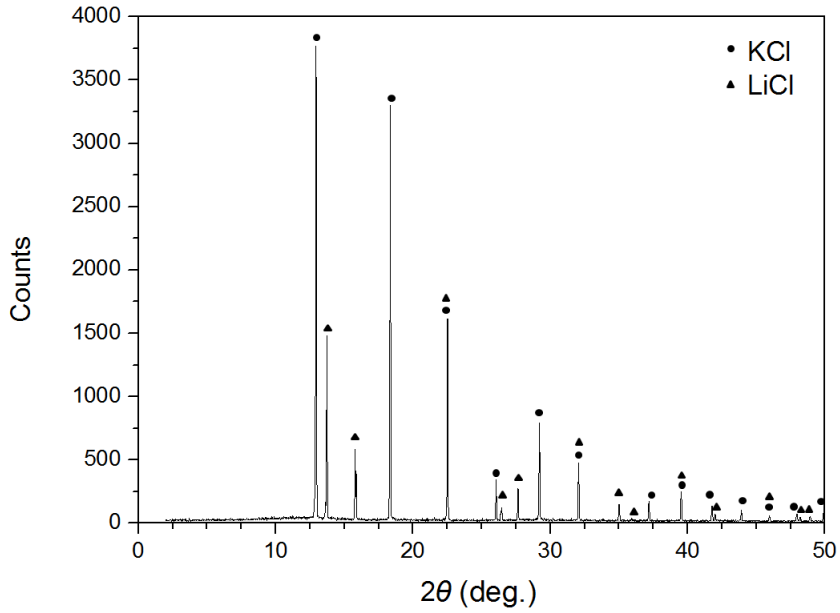

Figure 3.19 - X-ray diffraction spectrum (Mo Kα) of treated LiCl-KCl salt, showing KCl (165593-ICSD [127]), and LiCl (26909-ICSD [128]).

Prior to conducting electrochemical experiments, the electrolyte is treated further, via applying a constant potential of -2.3 V, close to the salt's decomposition potential, using a sacrificial tungsten electrode, a pre-electrolysis step, to remove any residual contaminant and moisture. This is usually applied for a few hours. Figure 3.18 illustrates a typical pre-electrolysis chronoamperogram. The salt eutectic was analysed via X-ray powder diffraction, Figure 3.19, which shows the spectra of pure LiCl and KCl, indicating that the salt is contaminant-free (free of metal ions).

3.3.5 Electrochemical set-up

A PC computer controlled potentiostat (IviumStat, Ivium Technologies, NL) was used to perform electrochemical tests. Most experiments were run using a four lead option, working electrode, counter electrode, reference electrode and 'sense'. The sense lead is attached to the electrode just below the working electrode's lead to reduce the voltage drop effects from the connecting cable, which might affect the

potential difference between the working and the reference electrode. The potentiostat was used to run electro-analytical tests such as cyclic voltammetry (CV), linear sweep voltammetry (LSV), chronoamperommetry and chronopotentiommetry.

3.4 Summary

In this chapter, the electrochemical and material characterisation techniques used in this research have been outlined. The experimental designs and materials used have also been covered, including the electrolytic cells, the electrodes and the salt eutectic used in experiments. The procedures to prepare experiments and to treat the LiCl-KCl eutectic have been outlined. Characterisation of the treated salt has also been included.

4. Predominance Diagrams

Predominance phase diagrams for metal-molten salt systems are diagrams of potential vs. the negative logarithm of the activity of O^{2-} ions (E-pO^{2-}); they are a valuable tool for predicting and understanding electrochemical systems and for optimising process conditions. Here, predominance diagrams are produced for U, Pu, Np, Am, Cm, Cs, Nd, Sm, Eu, Gd, Mo, Tc, Ru, Rh, Ag and Cd species, in both LiCl-KCl at 500 ˚C and NaCl-KCl at 750 ˚C. The two salt eutectics were chosen as they are the two main systems for pyroprocessing; temperatures were selected within each salt's normal operating range. All of the diagrams presented show regions of stability for the different metal species, their oxides and chlorides at unit activity; however, this activity can be altered in accordance with the equations derived. Examples of selective electrochemical reduction are also demonstrated for potential spent fuel reprocessing in both salt systems.

4.1 Introduction

Different process schemes and salts have been studied in pyroprocessing, most of which have been summarised by the NEA [15]. There are currently two main molten salt technology processes in existence, both using chloride salts as electrolytes; one in the US at the Argonne National Laboratory (ANL) using LiCl-KCl eutectic for metallic fuel in integral fast reactors (IFR), and one in Russia at the Research Institute for Atomic Reactors (RIAR) using NaCl-KCl eutectic for oxide fuel for the Fast Breeder Reactor (FBR) [16]. There have also been other advances made in molten salt nuclear pyroprocesses in Europe and Japan [19-24].

Predominance diagrams (also known as Littlewood diagrams) were originally developed by Littlewood in 1962 [129] to summarise thermodynamic characteristics of metal-molten salt systems and are akin to Pourbaix diagrams, which describe the behaviour of species in aqueous solutions. In Pourbaix diagrams, the equilibrium potential is plotted against pH to show regions of

stability for a specific system [130]. Predominance diagrams show potential vs. the negative logarithm of the activity of oxygen anions: the pO^{2-}.

The fundamental notion of predominance diagrams is to represent thermodynamic data in a diagrammatic form. Data is converted to linear equations relating free energies to logarithmic functions of material composition. The free energies of the system are represented by potentials that are relative to the electrochemical equilibrium between the salt's anion and its elemental form, in chloride salts this is the standard chlorine electrode. The composition variable is the negative logarithm of the activity of the oxygen ions in the melt, pO^{2-} (analogous to *p*H). These diagrams are very useful when studying complex metal-molten salt systems, such as Li-K-U-O-Cl, as they describe the regions of stability and the pathways of the system's evolution at different equilibrium potentials.

The procedure for producing predominance diagrams is best described in the works of Littlewood, Dring *et al*. and Brown *et al*. [129, 131, 132]. Predominance diagrams have been developed for various systems [133-140], providing valuable insight into the electrochemical processes of metals and their oxides in molten salts. However, they are not flawlessly accurate. Fundamentally predominance diagrams are only as accurate as the thermodynamic data used to create them, and therefore they need to be validated experimentally, as reaction kinetics and surface processes will have a dominant effect in defining reaction rate. Extensive work has been performed to characterise the reduction of TiOx in $CaCl_2$; this has been compared with the predominance diagram produced by Dring *et al*. [131]. X-ray diffraction analysis of the reduction process of TiO_x at different stages has been carried out by Schwandt and Fray, Wang and Li, and Bhagat *et al*. [47, 50, 141], providing validation of processes predicted by the predominance diagram.

Table 4.1 - List of nuclides commonly considered in burn-up credit criticality analyses (from NEA 2011) [142] and used as the basis for the systems examined here.

Nuclide	Half-life (years)	Content in spent UOX PWR fuel[a] (g/MTHM) 52 GWd/t at discharge	Relative importance rank for 40 GWd/MTHM PWR fuel – 5 years cooling[b]
^{234}U	2.45×10^{5}	143	24
^{235}U	7.04×10^{8}	6050	1
^{236}U	2.34×10^{7}	5650	11
^{238}U	4.47×10^{9}	927000	3
^{238}Pu	87.74	372	22
^{239}Pu	2.41×10^{4}	5810	2
^{240}Pu	6550	2840	4
^{241}Pu	14.40	1820	5
^{242}Pu	3.76×10^{5}	1020	19
^{237}Np	2.14×10^{6}	811	14
^{241}Am	432.60	228	10
^{243}Am	7370	1.74	11
^{243}Cm[c]	28.50	0.624	
^{244}Cm[c]	18.11	141	
^{245}Cm[c]	8532	11	
^{133}Cs	Stable	1630	12
^{143}Nd	Stable	1070	7
^{145}Nd	Stable	989	17
^{147}Sm	1.06×10^{11}	196	20
^{149}Sm	2.00×10^{15}	3.36	6
^{150}Sm	Stable	446	23
^{151}Sm	93	14.7	9
^{152}Sm	Stable	134	15
^{153}Eu	Stable	184	18
^{155}Gd	Stable	3.93	13
^{95}Mo	Stable	1180	21
^{99}Tc	2.10×10^{5}	1120	16
^{101}Ru	Stable	1210	26
^{103}Rh	Stable	540	8
^{109}Ag	Stable	119	25
^{113}Cd[c]	9.10×10^{15}		

[a] Measured content from ARIANE experimental programme data.
[b] Based on relative sensitivity coefficients from the Nuclear Regulatory Commission (2008) [143].
[c] Important for MOX fuel only.

Another limitation is that there is no adequate experimental technique for keeping the O^{2-} levels within a specified limit. Studies have looked at monitoring and controlling the pO^{2-} in molten salts [144]; but this is difficult to implement in practice, particularly on a larger scale. Rigorous salt preparation can reduce the O^{2-} ion concentration; however, once the reduction of a metal oxide proceeds, the increase of O^{2-} concentration in the melt shifts the equilibrium potential. Also, the

degradation and the formation of pores on the working electrode can act to 'trap' O^{2-} ions, thus increasing the levels at the interface, changing the local equilibrium. New reactor cell designs could prove useful here, such as the fluidised cathode process, as it would help disperse the O^{2-} ions, and give the system more homogeneity.

The nuclides commonly considered in burn-up credit analysis by the NEA [142] are shown in Table 4.1. This also lists their half-lives, their content (in g per metric tonne of heavy metal, g/MTHM) in uranium oxide (UOX) pressurised water reactor (PWR) spent-fuel and their relative importance according to the NEA. The different nuclides of uranium and plutonium are of highest importance, as their content in spent-fuel is significant. All of these nuclides are classed as high-level waste.

In this chapter, predominance diagrams are produced for spent nuclear materials in LiCl-KCl eutectic at 500 ˚C, as is in use at the ANL, and NaCl-KCl eutectic at 750 ˚C, as is in use at the RIAR. Each temperature was chosen to be within the salts' common operating temperature ranges [16, 35].

4.2 Theory

To construct a predominance diagram, one needs to employ the following equations and follow the subsequent steps. The Gibbs energy of formation of a given reaction, *ΔG*, may be related to the electrochemical potential of the specific cell, *E*, by Equations 4.1 (away from standard state) and 4.2 (standard state), and by the Nernst Equation 4.3. In these equations, *n* is the moles of electrons transferred in a reaction, *F* is Faraday's constant (96485.4 C mol^{-1}), *R* is the universal gas constant (8.314 J mol^{-1} K^{-1}), *T* is the operating temperature of the molten salt in Kelvin, and *Q* is the reaction quotient, a function relating the activities of the different chemical species involved in a chemical reaction.

$$\Delta G^o = -nFE^o \quad 4.1$$

$$\Delta G = -nFE \quad 4.2$$

$$E = E^o - \frac{RT}{nF} lnQ \quad 4.3$$

The potential window of the salt defines the bounds of the predominance diagram. For example, in LiCl-KCl, Cl_2 gas evolution defines the oxidative limit, and formation of metallic Li or K defines the reductive limit. The oxidative limit (in this example, the formation of Cl_2) is assigned a Gibbs energy of formation of zero, at all temperatures, to maintain a zero potential reference point. This is when the Cl_2 formed is at unit activity with the Cl^- ions in the melt at one atmospheric partial pressure. From this zero reference point, the regions of stability for the system chosen extend to the reductive limit, the decomposition potential of the salt.

There are three types of equilibrium that define the thermodynamic regions of stability for a specific species: one that does not involve transfer of electrons; one that does not involve transfer of oxide anions; and one that depends on both electron and oxide anions being transferred. Equations 4.4, 4.5 and 4.6 represent the three kinds of equilibrium reactions, where *M* is metal. Using Equations 4.1, 4.2 and 4.3, the equations in terms of electrode potential, *E*, and pO^{2-}, for each reaction can be derived, as seen in Equations 4.7, 4.8 and 4.9.

$$MO_y + 2yCl^- \leftrightarrow MCl_{2y} + yO^{2-} \quad 4.4$$

$$M^{(z+n)+} + ne^- \leftrightarrow M^{z+} \quad 4.5$$

$$MO_x + ne^- \leftrightarrow MO_{x-y} + yO^{2-} \quad 4.6$$

$$pO^{2-} = \frac{\Delta G^o_{4.4} + RTln\left(\frac{a_{MCl_{2y}}}{a_{MO_y}}\right)}{yRTln10} \quad 4.7$$

$$E_{4.5} = \frac{-\Delta G^o_{4.5}}{nF} - \frac{RT}{nF} ln\left(\frac{a_{M^z}}{a_{M^{z+n}}}\right) \quad 4.8$$

$$E_{4.6} = \frac{-\Delta G^o_{4.6}}{nF} - \frac{RT}{nF} ln\left(\frac{a_{MO_{x-y}}}{a_{MO_x}}\right) + \frac{yRTln10}{nF} pO^{2-} \quad 4.9$$

All thermodynamic data used is presented in Table 4.2.

Predominance diagrams for metal-molten salt systems are generally divided into three main regions of stability, where different species exist: one where the pure

metal exists, either in the salt solution or precipitated as a solid; one where the metal is covered by an oxide layer or is fully oxidised, also as a solute in the liquid salt or as a solid species; and one where the metal is in the form of a chloride, liquid or gas [129]. This is illustrated in Figure 4.1.

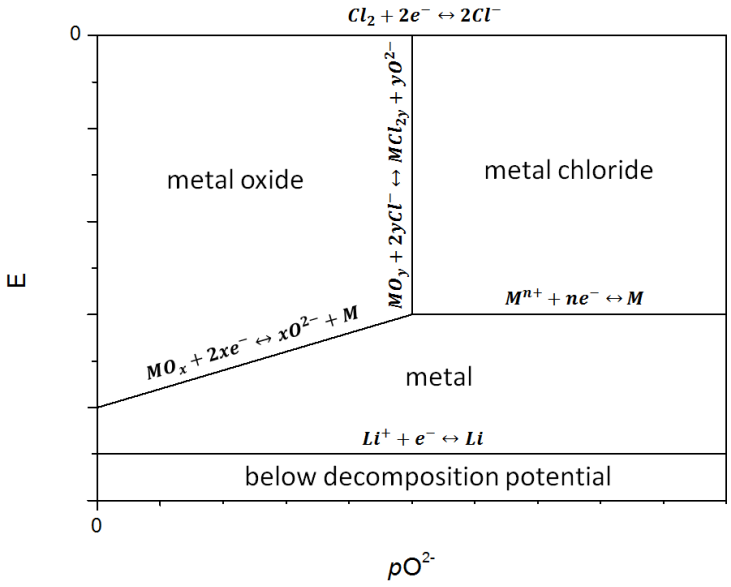

Figure 4.1 - Example of the three main regions of stability in a predominance diagram (based on a LiCl-KCl salt eutectic) and showing the nature of reactions leading to horizontal, vertical and diagonal lines.

The limiting potentials for the salt, at any given partial pressure of chlorine gas, and activity of liquid lithium metal and liquid potassium metal, may be calculated according to their corresponding Nernst Equations 4.13, 4.14 and 4.15, for the half-cell reactions presented in Equations 4.10, 4.11 and 4.12.

$$Cl_2 + 2e^- \leftrightarrow 2Cl^- \quad 4.10$$

$$Li^+ + e^- \leftrightarrow Li \quad 4.11$$

$$K^+ + e^- \leftrightarrow K \quad 4.12$$

$$E_{Cl_2} = E^O_{Cl_2} + \frac{RTln10}{2F}\log(\frac{P_{Cl^{2-}}}{P_{Cl_2}}) \quad 4.13$$

$$E_{Li} = E^O_{Li} + \frac{RTln10}{F}\log(\frac{a_{Li^+}}{a_{Li}}) \quad 4.14$$

$$E_K = E^O_K + \frac{RTln10}{F}\log(\frac{a_{K^+}}{a_K}) \quad 4.15$$

For the LiCl-KCl electrolyte at 500 ˚C, the potentials are solid horizontal lines at 0 V, -3.57 V and -3.76 V for the evolution of Cl_2, Li and K respectively. The same procedure was applied to the NaCl-KCl eutectic at 750 ˚C, and the potentials for the evolution of Na and K were found to be -3.28 V and -3.52 V respectively.

The next step is to calculate the Gibbs energy of formation of an oxide ion in the melt. There are two standard states for the oxide ion in the salt eutectic, these are Li_2O and K_2O. Using ΔG° of Equations 4.11 and 4.12, and ΔG° of the following half-cell reactions 4.16, 4.17 and 4.18, one can calculate the Gibbs energy of formation for the O^{2-} ion.

$$2Li + \frac{1}{2}O_2 \leftrightarrow 2Li^+ + O^{2-} \quad 4.16$$

$$2K + \frac{1}{2}O_2 \leftrightarrow 2K^+ + O^{2-} \quad 4.17$$

$$\frac{1}{2}O_2 + 2e^- \leftrightarrow O^{2-} \quad 4.18$$

At 500 ˚C, the Gibbs energy of formation for O^{2-} from Li_2O is +191.71 kJ mol^{-1}, and that from K_2O is +469.32 kJ mol^{-1}. The salt in this system is a LiCl-KCl eutectic with a molar composition of 59-41 respectively. Therefore, the assumed Gibbs energy of formation for the oxide ion at 500 ˚C in this system was calculated as +305.56 kJ mol^{-1}. The same method was applied to the NaCl-KCl equimolar system at 750 ˚C, and the Gibbs energy of formation for the oxide ion in the molten salt was established to be +408.91 kJ mol^{-1}.

Moreover, oxygen anions are in equilibrium with the atmosphere. Using the Gibbs energy of formation for O^{2-} and the Nernst equation, Equation 4.19 can be derived.

$$E_{O^{2-}} = E^{o}_{O^{2-}} + \frac{RTln10}{4F} logP_{O_2} + \frac{RTln10}{2F} pO^{2-} \quad 4.19$$

This shows the relationship between the electrode potential as a function of standard state potential, the oxygen gas partial pressure and the negative logarithm of the oxide ion activity, pO^{2-}. It is depicted in the predominance diagram in Figure 4.2 as a series of diagonal dashed lines, showing several states of equilibrium between oxygen gas and oxide ions at various O_2 partial pressures. The information from this diagram is useful for molten salt systems, where partial pressures of oxygen are normally very low, as it shows the potentials at which O_2 would be in equilibrium with the melt. These lines can be derived for the NaCl-KCl eutectic system following the same procedure. They can be superimposed onto the metal phase diagrams; however, to aid visual interpretation this is not performed here. Nonetheless, it is shown for uranium species, in Figure 4.9 and Figure 4.10.

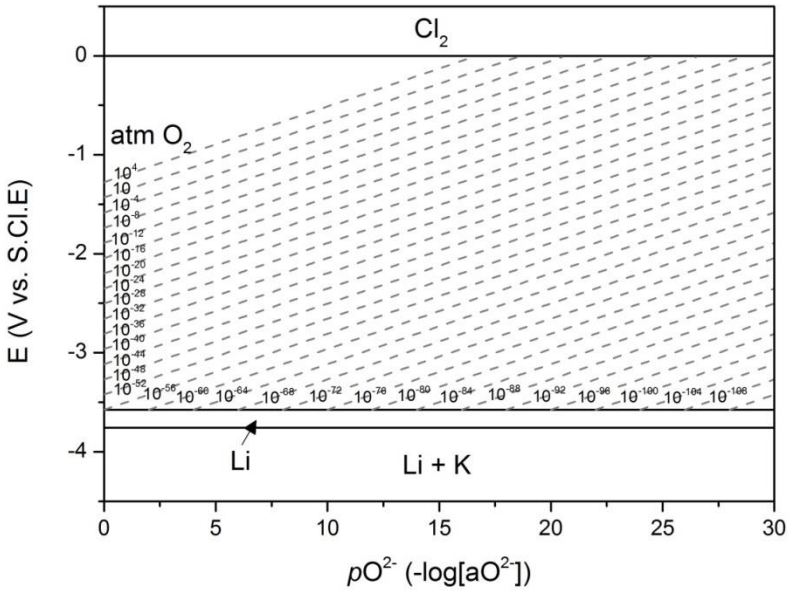

Figure 4.2 - Predominance diagram for the Li-K-O-Cl system at 500 °C, illustrating the relationship between oxygen pressure, oxide activity and potential, *E*, relative to the standard chlorine electrode.

Table 4.2 - Gibbs energy of formation for nuclear materials at 500 °C and 750 °C.

Species	ΔG_f^0 (kJ mol^{-1}) at 500 ˚C	ΔG_f^0 (kJ mol^{-1}) at 750 ˚C	Comments	References
LiCl (NaCl)	-344.887	(-316.766)		[145-147]
Li_2O (Na_2O)	-498.105	(-274.608)		[145, 148-152]
KCl	-362.418	-339.473		[153, 154]
K2O	-255.559	-220.057		[148, 149]
Li_2UO_4 (Na_2UO_4)	-1662.680	(-1486.881)	Extrapolated above 27 ˚C	[151, 152, 155]
UO	-477.980	-455.771	Extrapolated above 227 ˚C	[156]
UO_2	-950.563	-907.756		[149, 157]
U_4O_9	-3921.203	-3736.848		[149]
U_3O_8	-3055.659	-2896.089		[149]
UO_3	-1023.699	-962.404		[145, 148, 149]
UCl_2O	-888.723	-837.432	Extrapolated above 527 ˚C	[150, 155]
$U_2Cl_5O_2$	-1796.568	-1677.069	Extrapolated above 427 ˚C	[151]
UCl_3	-692.619	-642.160		[151, 155]
UCl_4	-794.542	-735.413		[145, 158]
Pu_2O_3	-1475.278	-1410.029		[148, 149]
PuO_2	-908.526	-861.327		[148-150]
PuClO	-806.625	-765.969		[155, 157]
$PuCl_3$	-787.684	-733.376		[154, 155, 158]
Li_2NpO_6 (Na_2NpO_4)	-1355.089	(-1346.466)	Extrapolated above 27 ˚C	[152]
NpO_2	-938.781	-894.564		[149, 155]
Np_2O_5	-1822.103	-1709.164	Extrapolated above 527 ˚C	[155]
$NpCl_3$	-725.188	-670.084		[155, 157]
$NpCl_4$	-758.434	-705.146	Extrapolated above 727 ˚C	[155]
Am_2O_3	-1473.270	-1406.104		[155]
AmO_2	-795.968	-756.153		[147, 155]
AmClO	-817.211	-777.668		[155]
$AmCl_3$	-795.282	-739.928	Extrapolated above 27 ˚C	[155]
Cm_2O_3	-1430.229	-1328.186	Extrapolated above 27 ˚C	[159]
CmO_2	-748.492	-684.109	Extrapolated above 27 ˚C	[159, 160]
CmClO	-807.035	-744.292	Extrapolated above 27 ˚C	[159]
$CmCl_3$	-767.028	-683.871	Extrapolated above 27 ˚C	[159]
Cs_2O	-242.961	-205.878		[148, 158]
Cs_2O_2	-283.880	-228.116		[148, 156, 158]
Cs_2O_3	-327.724	-259.383	Extrapolated above 427 ˚C	[150]
CsO_2	-173.900	-136.486	Extrapolated above 200 ˚C	[151]
Nd_2O_3	-1587.405	-1519.064		[148, 149, 151]

NdO_2	-696.669	-447.885	Extrapolated above 200 ˚C	[161]
NdClO	-855.745	-811.395		[145]
$NdCl_3$	-852.695	-796.445		[151]
Sm_2O_3	-1597.552	-1524.838		[145, 149]
SmClO	-861.226	-817.884	Extrapolated above 727 ˚C	[151]
$SmCl_3$	-838.055	-783.450		[145, 158]
EuO	-513.126	-489.177		[148, 151, 158]
Eu_2O_3	-1409.857	-1335.566		[151]
EuClO	-750.346	-703.088		[156]
$EuCl_3$	-737.401	-683.034		[151, 158]
Gd_2O_3	-1615.765	-1545.666		[148, 157, 158]
GdClO	-841.390	-797.533	Extrapolated above 727 ˚C	[145, 147, 148]
$GdCl_3$	-815.177	-765.475	Extrapolated above 727 ˚C	[150, 158]
Li_2MoO_4 (Na_2MoO_4)	-1232.046	(-1086.773)		[149, 151, 154, 162]
MoO_2	-445.688	-402.174		[149, 152, 163]
MoO_3	-547.974	-487.662		[145, 148, 149]
$MoCl_2O$	-357.355	-305.131		[147, 148]
$MoCl_2$	-172.364	-136.825		[147, 148, 151]
$MoCl_5$	-284.750	-223.078		[146, 158]
TcO_2	-314.411	-270.073		[150, 156]
TcO_3	-349.485	-300.478	Extrapolated above 127 ˚C	[145]
Tc_2O_7	-738.443	-644.378	Extrapolated above 427 ˚C	[149, 154]
$TcCl_3$	-133.223	-88.864		[156]
RuO_2	-172.921	-133.825		[150]
RuO_4	-47.246	0.188	Extrapolated above 172 ˚C	[151]
$RuCl_3$	-54.551	-4.138	Extrapolated above 450 ˚C	[150]
Rh_2O	-57.798	-47.534	Extrapolated above 727 ˚C	[157]
RhO	-31.229	-13.954		[157]
RhCl	-40.413	-28.786		[156]
$RhCl_2$	-65.752	-41.129		[156]
$RhCl_3$	-92.650	-39.953		[150-152]
Ag_2O	19.033	33.200		[147, 151, 159]
AgO	55.057	76.216	Extrapolated above 125 ˚C	[160]
Ag_2O_3	286.073	386.987	Extrapolated above 125 ˚C	[159]
AgCl	-86.475	-80.450		[147, 151, 152]
CdO	-181.481	-155.461		[151, 152, 157]
$CdCl_2$	-270.663	-240.187		[147, 150]

The functions of the interface lines between the different regions of stability, for each system, were derived using Reactions and Equations 4.4-4.9 and the thermodynamic data presented in Table 2. These are all presented in Appendix B. Pure liquid phases were assigned an activity of unity and pure gases were assigned unit atmosphere partial pressure. The diagrams depict regions of stability for species in solution and solid phases that would precipitate out, as well as liquid and gas phases. These diagrams can also be altered, by changing the activity used and conditions, which would shift the equilibria lines accordingly. For simplicity, unit activities are shown here. The predominance diagrams for the spent nuclear fuel materials in LiCl-KCl eutectic at 500 ˚C and NaCl-KCl eutectic at 750 ˚C are presented in Figure 4.3, Figure 4.4, Figure 4.5 and Figure 4.6.

4.3 Results

Some of the general features of the predominance diagrams can be illustrated by reference to the uranium system in Figure 4.3(a). Compounds with uranium at their highest oxidation states are found in the upper regions of the diagram, at less negative potentials. At very low oxide ion activities, on the right hand side of the diagram, uranium chlorides (UCl_3, UCl_4) are formed. Uranium metal can be extracted from these at less negative potentials compared to the reduction of UO_2. Since there is no transfer of O^{2-} ions in these reactions, from U^{4+} to U^{3+} and to U, the resultant interline functions between these species' regions of stability are independent of pO^{2-}. Thus, the interfaces are represented as horizontal lines in the predominance diagram.

Due to the stability of other compounds that could exist in the melt, there is an intermediate region of stability between the oxides and the chlorides. This intermediate region is the metal oxychloride form. In the case of uranium it is UCl_2O and $U_2Cl_5O_2$. The interface between these two phases is a horizontal line, as there is no transfer of O^{2-} occurring. The interfaces between the regions of stability of the reactions from UO_2 to UCl_2O and to UCl_4 are all vertical lines; hence, the derived interface equations are independent of potential, as the ratio of U

molecules does not change. All the other equations for interface lines related to UCl_2O and $U_2Cl_5O_2$ are dependent on both pO^{2-} and E, resulting in diagonal lines.

At high oxide ion activities, on the left hand side of the predominance diagram, other types of uranium oxides are predicted to form. This is due to the oxide ions reacting with lithium or potassium ions in the fused salt. In the case of uranium, the first stable metal uranium oxide to form is Li_2UO_4, as presented in Figure 4.3(a).

For the electrochemical reduction of UO_x to U metal, the reductive potential is very negative and close to the salt's decomposition potential. The diagram gives an indication of the number of phases expected to appear, and the order they would appear in, if UO_3 were to be reduced. It can also be deduced that some compounds, such as U_3O_7, UO and U_4O_9, have a very narrow band of stability, when reducing the uranium oxide; thus, it is not very likely that traces of them will remain in the final product, as is the case with TiOx [50].

The predominance diagrams for U in NaCl-KCl, and for Pu, Np, Am, Cm, Cs, Nd, Sm, Eu, Gd, Mo, Tc, Ru, Rh, Ag and Cd, in both LiCl-KCl and NaCl-KCl, can be interpreted in the same way as for U in LiCl-KCl. They are all presented in Figure 4.3(a-h), Figure 4.4(a-h) Figure 4.5(a-h) and Figure 4.6(a-h).

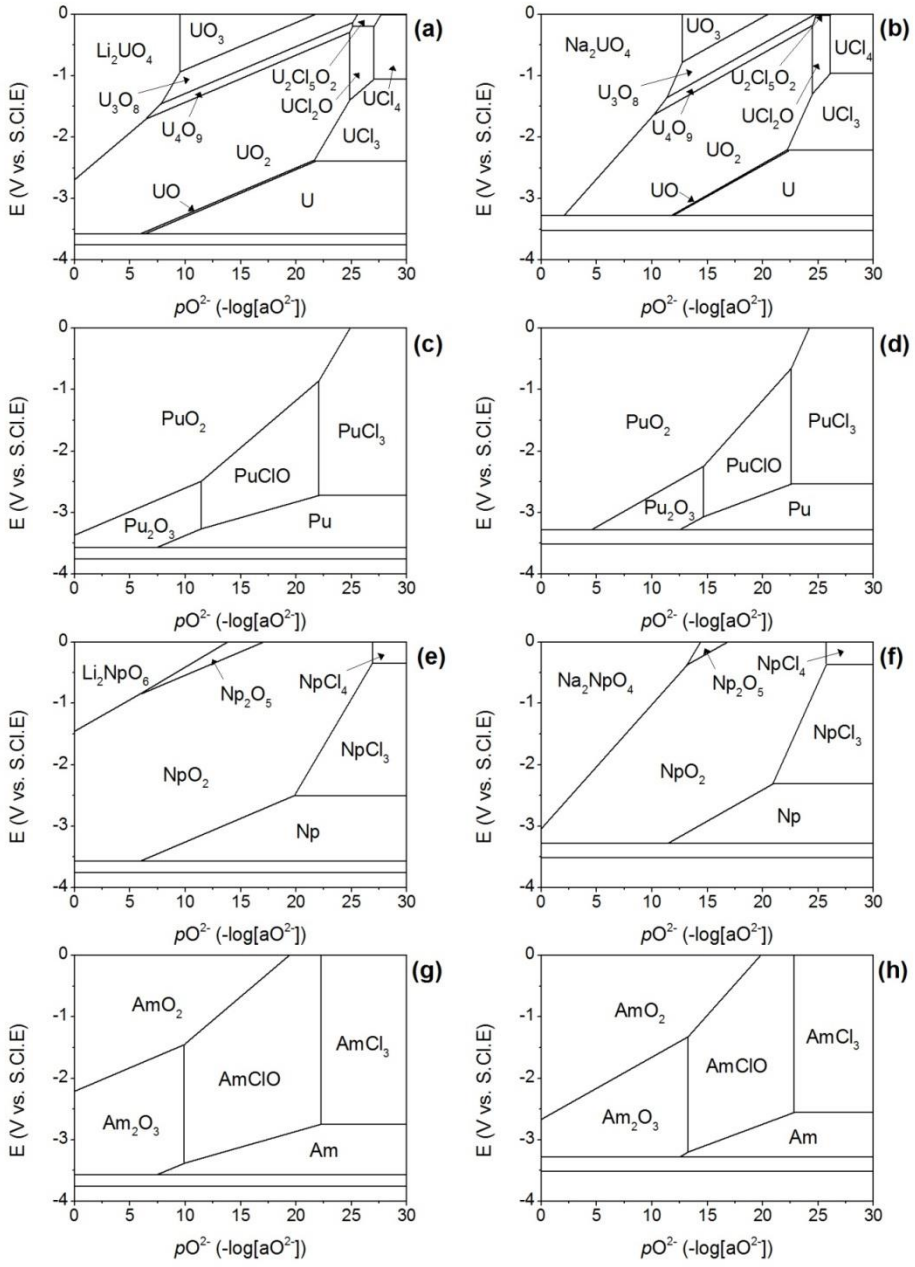

Figure 4.3 - Predominance diagrams of (a) U, (c) Pu, (e) Np, and (g) Am in LiCl-KCl at 500 °C. (b) U, (d) Pu, (f) Np, and Am are in NaCl-KCl at 750 °C.

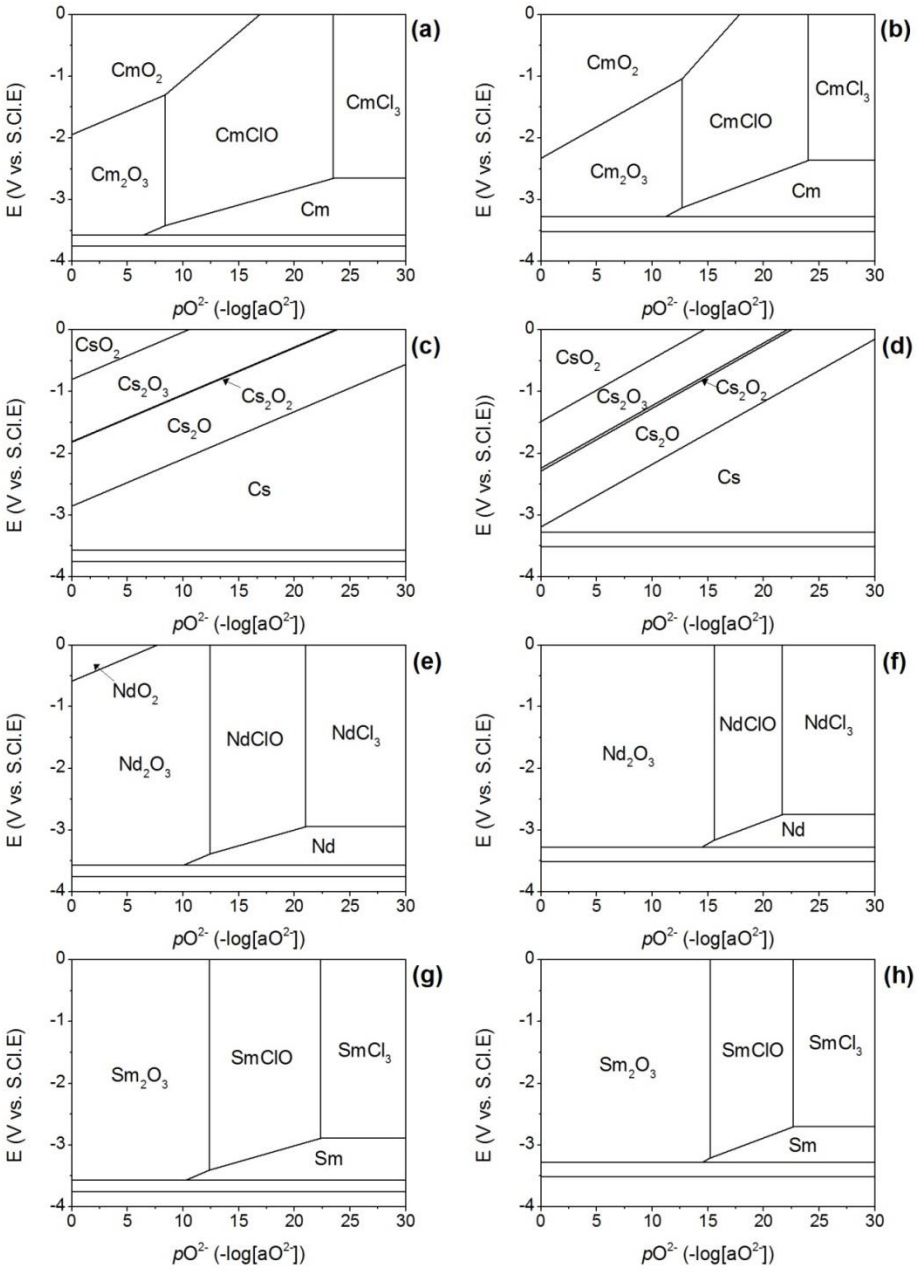

Figure 4.4 - Predominance diagrams of (a) Cm, (c) Cs, (e) Nd, and (g) Sm in LiCl-KCl at 500 °C. (b) Cm, (d) Cs, (f) Nd, and Sm are in NaCl-KCl at 750 °C.

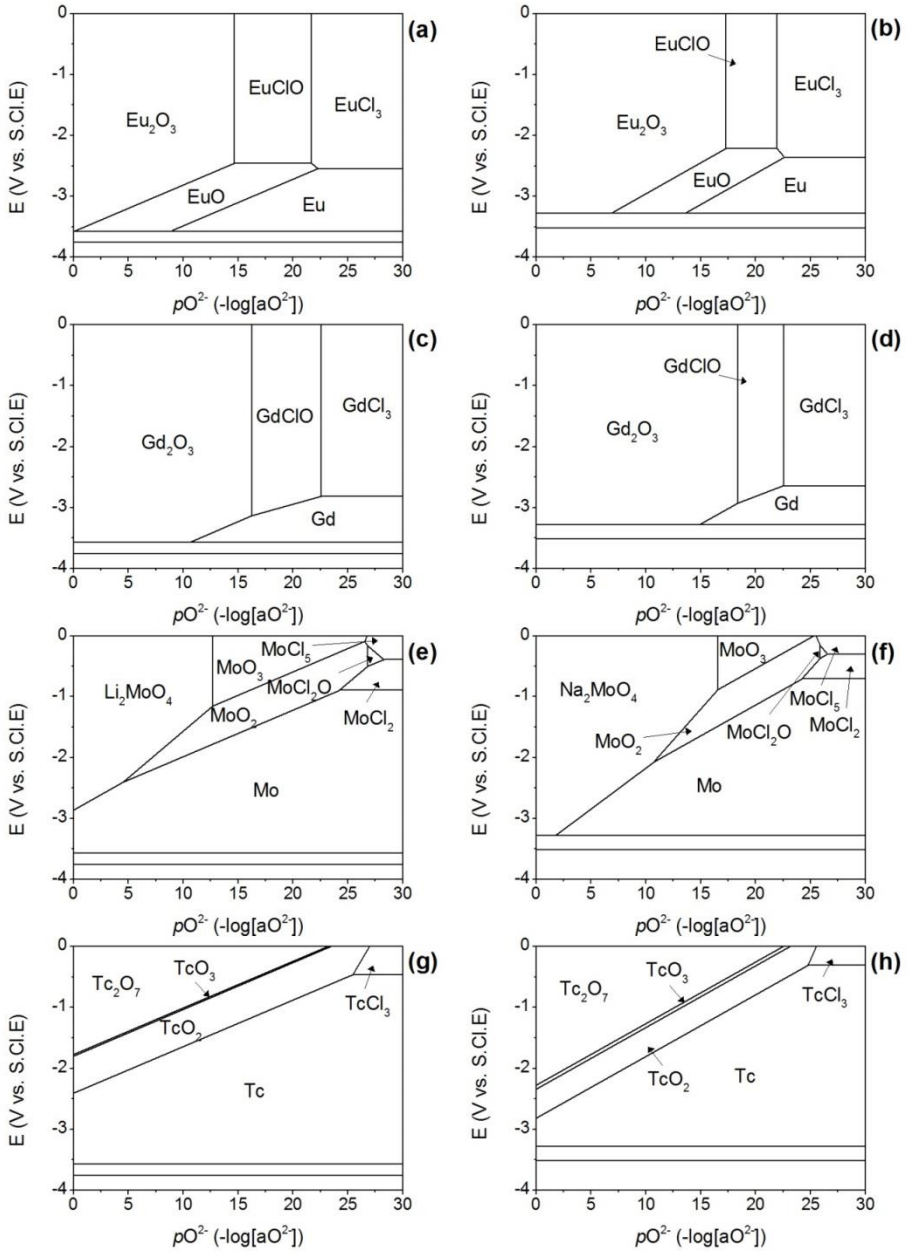

Figure 4.5 - Predominance diagrams of (a) Eu, (c) Gd, (e) Mo, and (g) Tc in LiCl-KCl at 500 °C. (b) Eu, (d) Gd, (f) Mo, and Tc are in NaCl-KCl at 750 °C.

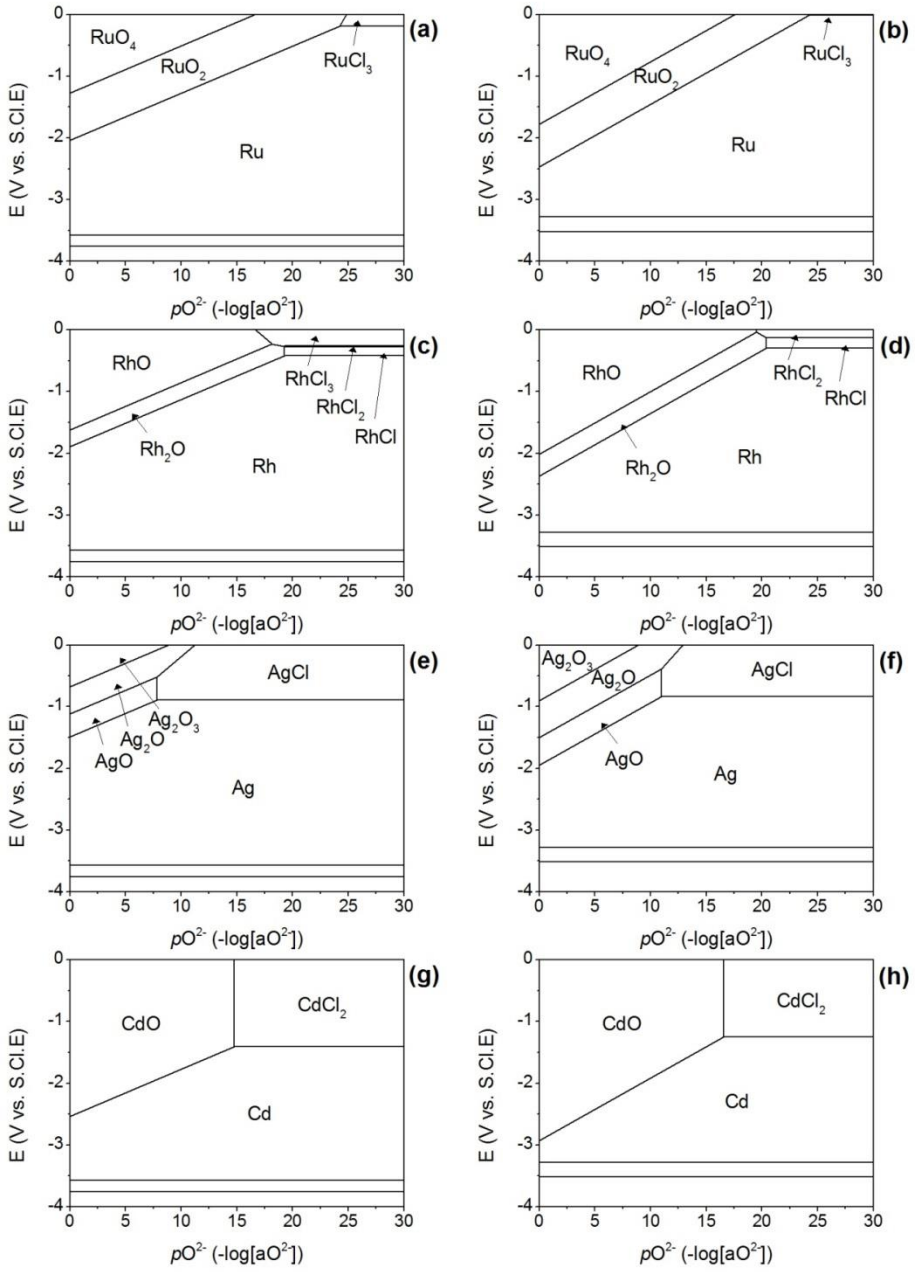

Figure 4.6 - Predominance diagrams of (a) Ru, (c) Rh, (e) Ag, and (g) Cd in LiCl-KCl at 500 °C. (b) Ru, (d) Rh, (f) Ag, and Cd are in NaCl-KCl at 750 °C.

4.4 Discussion

The interface lines between the lowest oxidation state and the pure metal state are of particular importance for electrochemical reduction and pyroprocessing, for metal fuelled reactors; and the interface line between oxide states for oxide fuelled reactors. From Figure 4.3, Figure 4.4, Figure 4.5 and Figure 4.6, it is evident that the reduction of the transition metals, Rh, Ag, Ru, Tc, Cd and Mo, showed first, at less negative potentials. Then, the reduction of U, Pu and the minor actinides, in the order of U, Cs, Pu, Am, Np and Cm, at increasingly negative potentials. Finally, the reduction of the lanthanides in order of increasingly negative potential: Nd, Sm, Gd and Eu. These findings are encouraging, as the three different groups are clearly divided, thus indicating that they can be selectively reduced and separated from the spent-fuel. Separating Pu as a single species appears to be challenging, this is an important non-proliferation feature.

From the predominance diagrams, it is also evident that some species have very narrow bands of stability, and thus might not be observed experimentally, if the metal oxides were to be reduced. This could be the case for U_3O_7, UO, U_4O_9, Np_2O_5, Cs_2O_2, $MoCl_2O$, TcO_3 and $RhCl_2$.

4.4.1 Comparison of eutectics

It is noticeable from the predominance diagrams that for all spent fuel materials, the region of stability for the pure metal phase is larger in the LiCl-KCl eutectic, than in the NaCl-KCl eutectic, even though the temperature is lower, 500 ˚C and 750 ˚C respectively. The final reduction stage from oxide to metal also appears to be possible at higher O^{2-} ion activities in LiCl-KCl compared to NaCl-KCl. Thus, it seems that the use of LiCl-KCl for molten salt pyroprocessing is more favourable than NaCl-KCl. However, this is purely based on thermodynamics and higher temperatures are likely to benefit from faster kinetics.

4.4.2 Selective electro-reduction

Selective direct reduction is when there is a mixture of different metal oxides and only one, or a subset of them, are selectively reduced and separated via electroplating. This can be very beneficial in the nuclear industry, to enable the

reprocessing and recycling of the useful spent fuel products selectively and separately, and also prevents nuclear proliferation. Thus, it is important to understand how control of electrode potential affects spent fuel products in a molten salt reprocessing reactor; comprehensive predominance diagrams are a starting point for such analyses.

One instance where the possibility of selective electro-reduction is not desired is for U and Pu. This is for anti-proliferation reasons. The predominance diagrams for Pu are superimposed onto those for U, in LiCl-KCl and NaCl-KCl, Figure 4.7. The main region of interest is the interface lines where the reduction from the lowest oxide state to the pure metal phase occurs (e.g. from -3 V and 10 pO^{2-} to -3.5 V and 11 pO^{2-} in Figure 4.7(a)). As seen in Figure 4.7, these boundary lines for the U and the Pu systems are very close to each other. Thus, it would be challenging to selectively reduce one of them exclusively. From Figure 4.7 it is evident that the uranium oxide reduction to uranium metal would occur first.

In principle, the use of predominance diagrams to aid the understanding of the feasibility of selective electro-reduction can be applied to all spent-fuel products, in order to understand the reduction procedure that they would undergo if they were all placed in a molten salt reprocessing reactor. Within each group, transition metals, actinides and lanthanides, difficulties are apparent in the partial reduction of a single species. In the transition metals group, partial reduction is the most likely to be achieved, with the exception of Cd and Mo, as their reduction interlines are too close to each other. In the actinides group, it is more difficult to perform partial reduction, Np being the exception. It is the most difficult to carry out partial direct reductions in the lanthanides group.

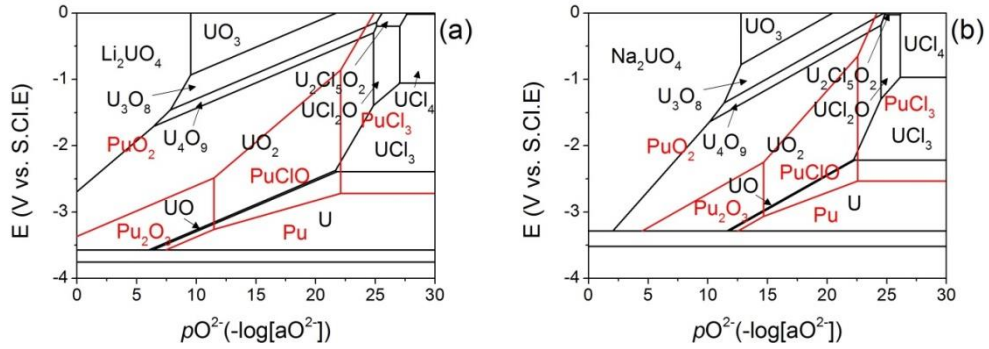

Figure 4.7 - Predominance diagrams of U and Pu species. (a) in LiCl-KCl at 500 °C, (b) in NaCl-KCl at 750 °C.

An example of where selective direct reduction would be useful is for Am and Cm: this is to mimic the EXAm [164] process in solvent extraction nuclear reprocessing. Am and Cm are both high heat emitters; however, Cm has a short half-life, ~ 18 years, and thus, it is not economically viable to reprocess it, as storage options would be cheaper. By contrast, it is desirable to reprocess and recycle Am. The predominance diagrams for Cm are superimposed onto those for Am, in LiCl-KCl and NaCl-KCl, Figure 4.8. From the predominance diagrams, it is evident that selective electro-reduction would be difficult for these two species due to the similarity in reduction potential. However, in this instance, the use of NaCl-KCl eutectic melt as the electrolyte is more favourable as the potentials for reduction of the two species form a larger window.

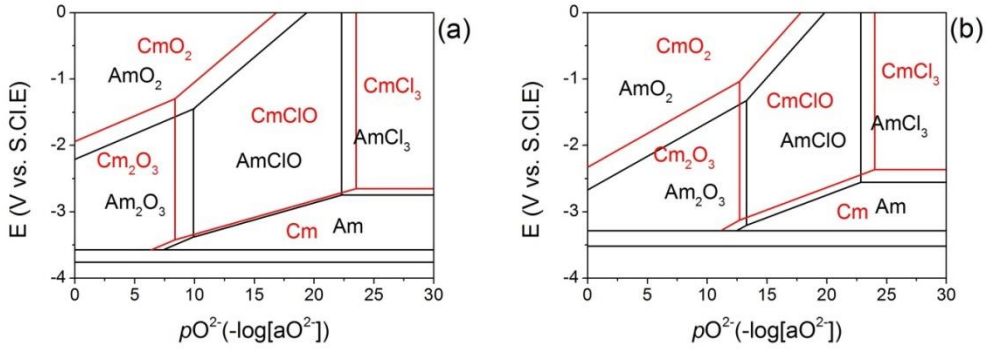

Figure 4.8 - Predominance diagrams of Am and Cm species. (a) in LiCl-KCl at 500 °C, (b) in NaCl-KCl at 750 °C.

4.4.3 Effect of temperature

Temperature is an important parameter that affects the stability zones. At higher temperatures the regions of stability are shifted to the 'left', at higher O^{2-} activity, where oxide reduction reactions occur; however, at higher temperatures, the potential window is smaller. Figure 4.9 and Figure 4.10 present predominance diagrams for uranium species in LiCl-KCl eutectic at 500 °C and 800 °C respectively. When comparing the two diagrams, one can clearly see the effects of temperature on the regions of stability. An interesting feature is also the disappearance of the stability band for UO entirely at the higher temperature, indicating that what could be a very fast 2 step 4-electron transfer process from UO_2 to U becomes a one step process.

From a design point of view, processes at lower temperatures are favourable, as heat requirements would be lower, also, the materials designated for reactor vessels, sealing, handling and maintenance are more practical at lower temperatures. Thus, provided that the fused salt is treated and O^{2-} levels are kept minimal, it is constructive to keep the operating temperatures low. These processes are also possible at lower temperatures as shown in Figure 4.9.

4.5 Conclusions

Predominance diagrams are useful tools for understanding the electrochemistry and phase stability of metal-oxide systems in molten salts. They help in predicting experimental results and give a good indication of whether an electrochemical process is thermodynamically feasible. Predominance diagrams have been generated for the range of spent nuclear fuel materials, based on established thermodynamic properties of the materials published in the literature.

By superimposing the diagrams for U and Pu, and Am and Cm onto each other, the potential for selective electro-reduction can be determined and the most suitable molten salt and temperature selected. It was found that molten salt pyroprocessing provides a promising route for reprocessing nuclear materials, which is also proliferation resistant. However, the approach is not seen to be a replacement for the EXAm process, as the selective reduction and separation of Am species from Cm would be challenging due to similarity in reduction potential.

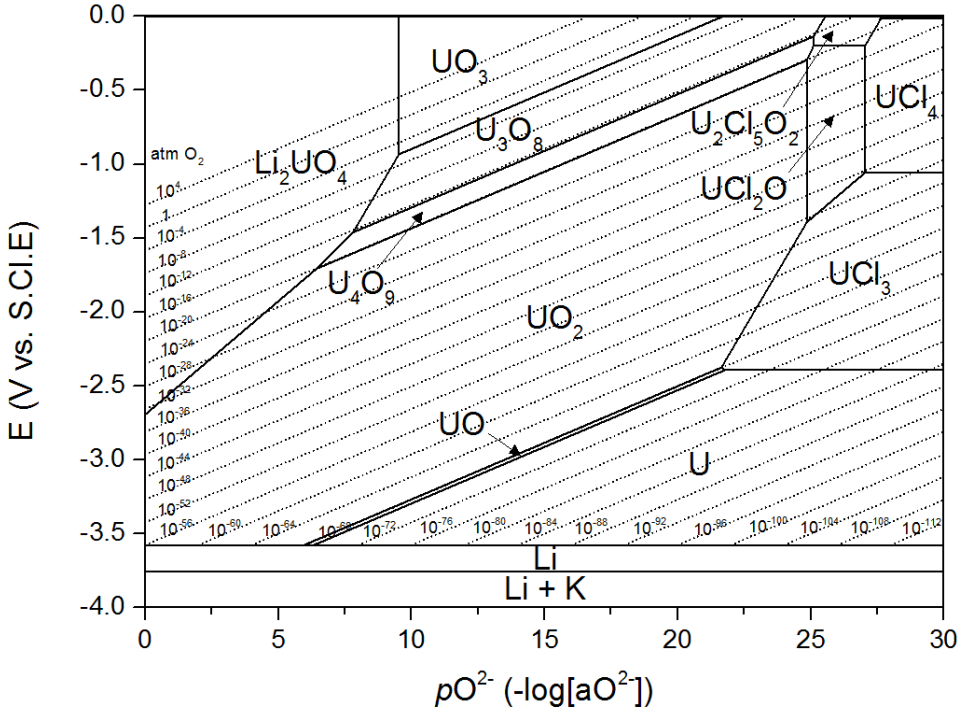

Figure 4.9 - Predominance diagram for the Li-K-U-O-Cl system at 500 °C.

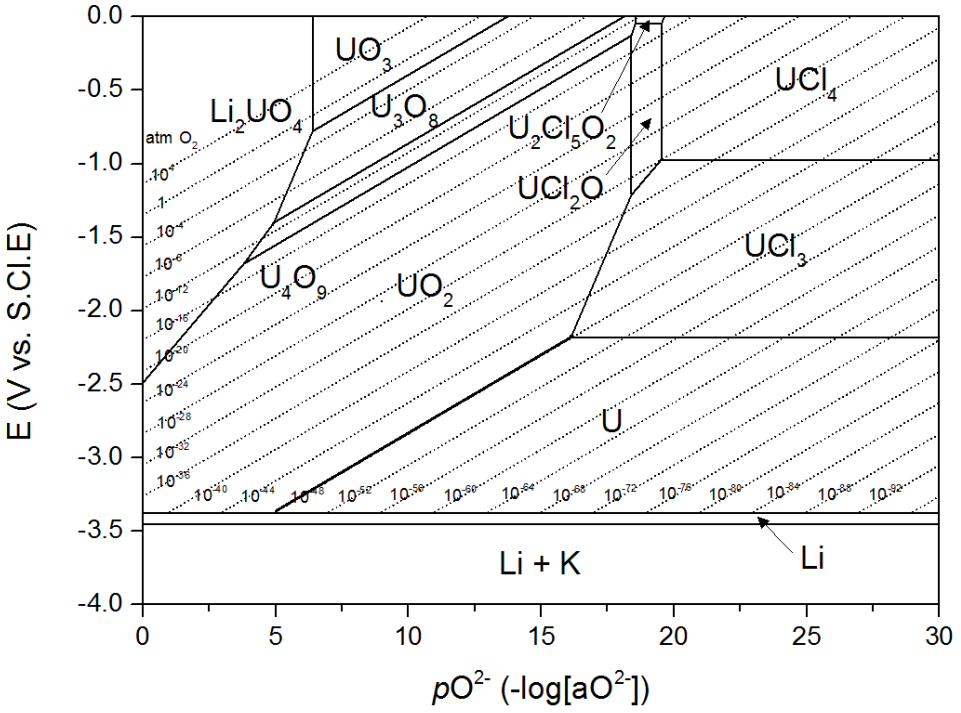

Figure 4.10 - Predominance diagram for the Li-K-U-O-Cl system at 800 °C.

5. The Electrochemical Reduction of Tungsten Oxide

The electrochemical reduction of WO_3 to W metal using a fluidised cathode process was investigated. Voltammetry studies were conducted, and alongside a predominance diagram that was constructed, the reaction path-way was studied. The main reduction potential appeared to be -2.14 V. A complete reduction, through applying constant voltage, was achieved with a Faradaic current efficiency of ~ 82%. The metal product is in the form of particles, either deposited on the electrode surface or settled at the bottom of the crucible. The effects of metal oxide – salt ratio and of fluidisation rate on the process were also investigated. Higher loading of metal oxide particles resulted in an increase in the rate of deposit growth, and in a decrease in particle-current collector collision-reaction spikes. An increase in fluidisation rate resulted in an increase in both rate of growth of deposit, as well as collision-reaction noise.

5.1 Introduction

Tungsten has many applications because of its physical and chemical properties [165]; this has sparked renewed interest in its production in the U.K. recently. Tungsten ore is usually extracted then converted to WO_3, which is in turn reduced to W metal by hydrogen and heating. This process is time and energy intensive [166]. The electrochemical reduction route might prove to be viable for the production of pure tungsten. Studies on the electrochemical reduction of tungsten oxide in molten salts have been published [167-169], mainly for the production of metal alloys [59, 170]. The precursors were porous solids in the form of pellets.

This Chapter reports on the current efficiency and the investigation of different characteristics that affect the fluidised cathode process, using a model system of tungsten oxide and LiCl-KCl molten salt eutectic.

5.2 Experimental

5.2.1 Apparatus

A schematic of the electrolytic cell used is illustrated in Figure 3.13(b). The cathode consists of WO_3 particles that are suspended in the molten salt (LiCl-KCl) eutectic, and a pure tungsten rod current collector. The anode is a graphite rod separated in its own compartment to avoid reoxidation of the reduced tungsten particles; the anode compartment has an opening at the top to allow for gases to escape. The melt is agitated via a flow of argon. A reference electrode (Ag/Ag^+) was used, and the temperature was monitored via a thermocouple that is immersed in the melt. All electrochemical tests were performed using a potentiostat (IviumStat, Ivium Technologies, NL).

The same set-up was used to carry out the thin film experiments. However, no WO_3 particles were employed, the counter electrode was not separated inside a compartment, no argon was bubbled through the melt, and the current collector was replaced with a thin film cathode, Figure 3.13(a).

5.2.2 Chemicals

All preparation steps were carried out under a sealed argon atmosphere. Anhydrous lithium chloride (ACS reagent, ≥99.0% purity, Sigma-Aldrich) and potassium chloride (≥99.5% purity, Sigma-Aldrich) were used for the electrolyte. The salt was dried in a vacuum oven at 200 ˚C for 24 h, then 150 g of 59-41 mol% LiCl-KCl were mixed with WO_3 (99.9% purity, Alfa Aesar). Particle size distribution measurements, Figure 5.1, were conducted using a Beckman Coulter LS13320 laser diffraction particle size analyser. Figure 5.2 shows the x-ray diffraction pattern of the as-received WO_3 powder. 15 g of LiCl-KCl was placed inside the anode compartment. The counter electrode was a high density graphite rod, 3.05 mm in diameter (99.9995% metal basis, Alfa Aesar). The working electrode (current collector) was a tungsten rod, 1.5 mm in diameter (99.95% metal basis, Alfa Aesar). A glass sheath around the shaft of the tungsten rod ensured that a constant surface area of electrode is exposed to the electrolyte, even when being

agitated by the Ar stream. Argon (99.998% purity, BOC) was bubbled through the melt via a ceramic tube (5 mm internal diameter, Alsint).

For the thin film experiments, the electrolyte was composed of 150 g of LiCl-KCl, prepared in the same way as for the fluidised cathode setup, but no WO_3 particles were used. The working electrode was thermally oxidised in air at a temperature ramp rate of 250 ˚C h^{-1}, then held at 700 ˚C for 2 h.

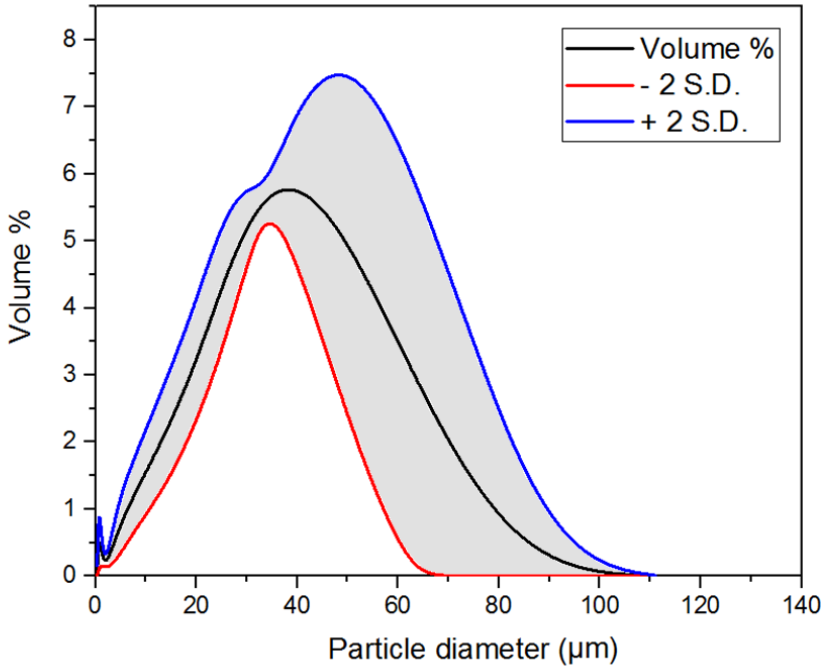

Figure 5.1 - Average particle size distribution of WO_3 powder in terms of volume percentage, also showing the maximum size distribution and the minimum, with a standard deviation of 2. Mean particle diameter: 30.9 µm, median particle diameter: 29.5 µm.

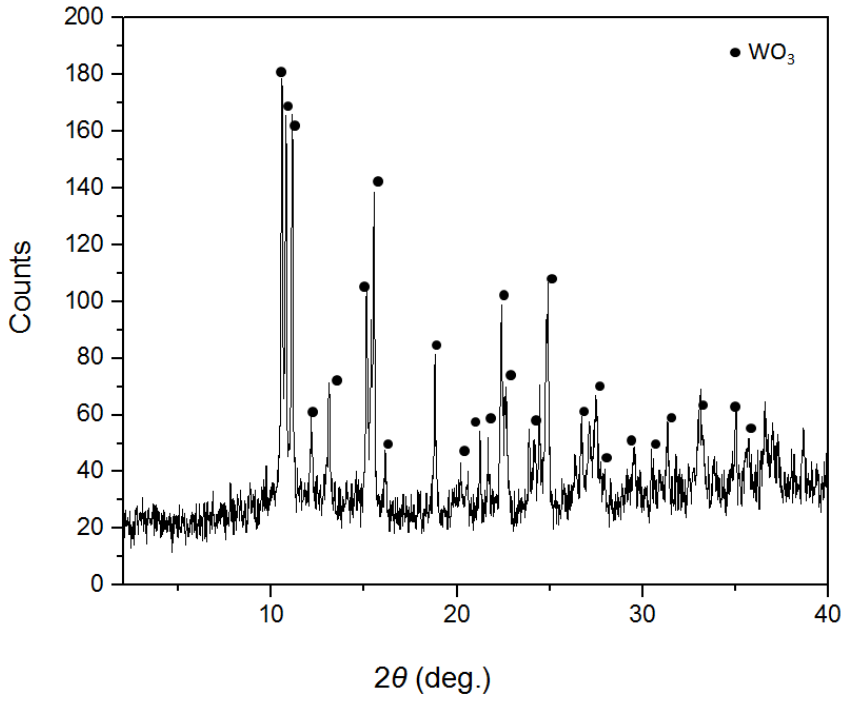

Figure 5.2 - X-ray diffraction spectrum (Mo Kα) of as-received WO_3 powder sample, showing WO_3 (1620-ICSD [171]).

5.2.3 Procedure

Experiments were carried out under a dry argon atmosphere at a melt temperature of 450 ˚C (unless indicated otherwise). Argon was bubbled into the melt, which resulted in a homogeneous distribution of particles as assessed by visual inspection. The current collector, 4 cm length (area of 3.84 cm^2), was immersed in the melt during the fluidised cathode measurements, and 2 cm length (area of 1.96 cm^2) during the thin film measurements. However, absolute currents are reported due to the fact that the electrode surface area changes during experiments.

5.3 Results and discussion

A predominance diagram, Chapter 4, was constructed for the Li-K-W-O-Cl system, relating the potential *E* vs. standard chlorine electrode (S.Cl.E) to the negative logarithm of O^{2-} ions activity, pO^{2-}. All the thermodynamic data used for the

production of the diagram is presented in Table 5.1, and the derived interface equations are presented in Appendix C. A predominance diagram for tungsten species in CaCl has been published [59]; however, this is the first in LiCl-KCl eutectic.

Table 5.1 - Gibbs energy of formation at 500 °C for species in the Li-K-W-O-Cl system.

Species	ΔG^0_f at 500 ˚C (kJ mol^{-1})	References
WO_2	-447.23	[149, 150, 163]
WO_3	-641.66	[150]
WCl_2O_2	-586.35	[146, 147]
WCl_2	-165.85	[146, 147, 150]
WCl_4	-237.11	[146, 150]
LiCl	-344.89	[145, 147, 163]
Li_2O	-498.11	[145, 148, 149]
KCl	-362.42	[153, 154]
K_2O	-255.56	[148, 149]

The predominance diagram in Figure 5.3 shows the different regions of stability for different compounds and oxidation states of tungsten. Thermodynamically, one can deduce that the concentration of O^{2-} ions in the eutectic melt does not hinder the reduction process of WO_3 to W. However, it affects the reaction pathway. Starting with WO_3, two reduction reactions take place to produce W metal. These are presented in Equations 5.1 and 5.2. Equations 5.3 and 5.4 are used to calculate the potential, *E*, needed for each reaction to take place, at different values of O^{2-} ion activity.

$$WO_3 + 2e^- \leftrightarrow WO_2 + O^{2-} \quad 5.1$$

$$WO_2 + 4e^- \leftrightarrow W + 2O^{2-} \quad 5.2$$

$$E_{5.1} = \frac{-\Delta G^0_{5.1}}{2F} + \frac{RTln10}{2F} pO^{2-} \quad 5.3$$

$$E_{5.2} = \frac{-\Delta G^0_{5.2}}{4F} + \frac{2RTln10}{4F} pO^{2-} \quad 5.4$$

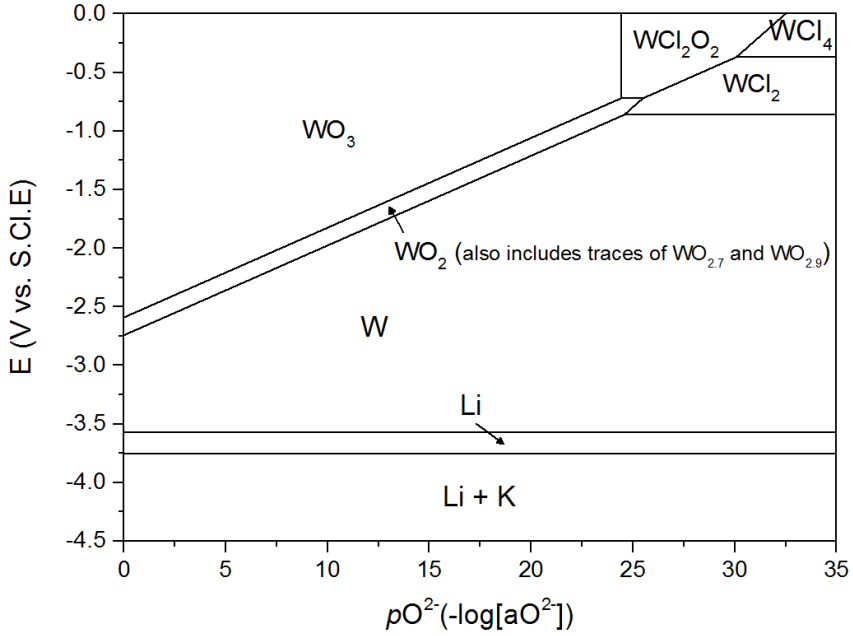

Figure 5.3 - Predominance diagram for the Li-K-W-O-Cl system at 500 °C.

The bands of potentials and pO^{2-} values are presented in Table 5.2. When comparing features in the predominance diagram, such as the evolution of Li or Cl_2, with when they appear in the cyclic voltammogram in Figure 3.17, the difference in potential between the Ag/Ag^+ reference electrode and the S.Cl.E is 1.136 V. The potentials needed for the proceeding of Equations 5.1 and 5.2, with respect to Ag/Ag^+, are also presented in Table 5.2.

Table 5.2 - Thermodynamically calculated values of pO^{2-} and potentials required for Equations 5.1, 5.2, 5.6 and 5.7 to take place.

Reaction	pO^{2-}	*E* (V vs. S.Cl.E)	*E* (V vs. Ag/Ag^+)
5.1	0.000 – 24.411	-2.591 – -0.721	-1.455 – +0.415
5.2	0.000 – 24.575	-2.740 – -0.860	-1.604 – +0.276

Voltammetry measurements were performed on a thermally grown thin film of WO_3 electrode set-up and a fluidised cathode set-up, Figure 5.4 (a) and (b) respectively. Both were scanned from 0 V to -2.7 V, and back to 0 V (vs. Ag/Ag^+ reference electrode). The peaks at 2 represent the reduction of Li^+, and at 3 represent its reoxidation. The smaller peaks appearing after 3 in the positive direction represent the reoxidation of W to WO_x. The peaks at 1 represent the main reduction step in Equation 5.5.

$$WO_3 + 6e^- \leftrightarrow W + 3O^{2-} \qquad 5.5$$

When comparing these two peaks in Figure 5.4 (a) and (b), one can see that the peak in (b) is shifted slightly to the right, and appears at -2.14 V, before peak 1 in (a) which appears at -2.21 V, as indicated by the dashed vertical lines in the diagrams. This is due to the nature of the fluidised cathode process, which provides less resistance. For an electrochemical reaction, a 3PI needs to be present for it to occur. In a molten salt system, this is the current collector (conductor), the fused salt (electrolyte) and the metal oxide (insulator). A 3PI is instantly initiated at the collision point of a particle with the current collector in the fluidised cathode process, thus the reaction extends from this point. In the case of a thin film, there is an insulating sheath of oxide covering the electrode surface, and therefore it is harder for the reaction to take place, resulting in more driving force being required, a higher overpotential. The same is true for peak 2.

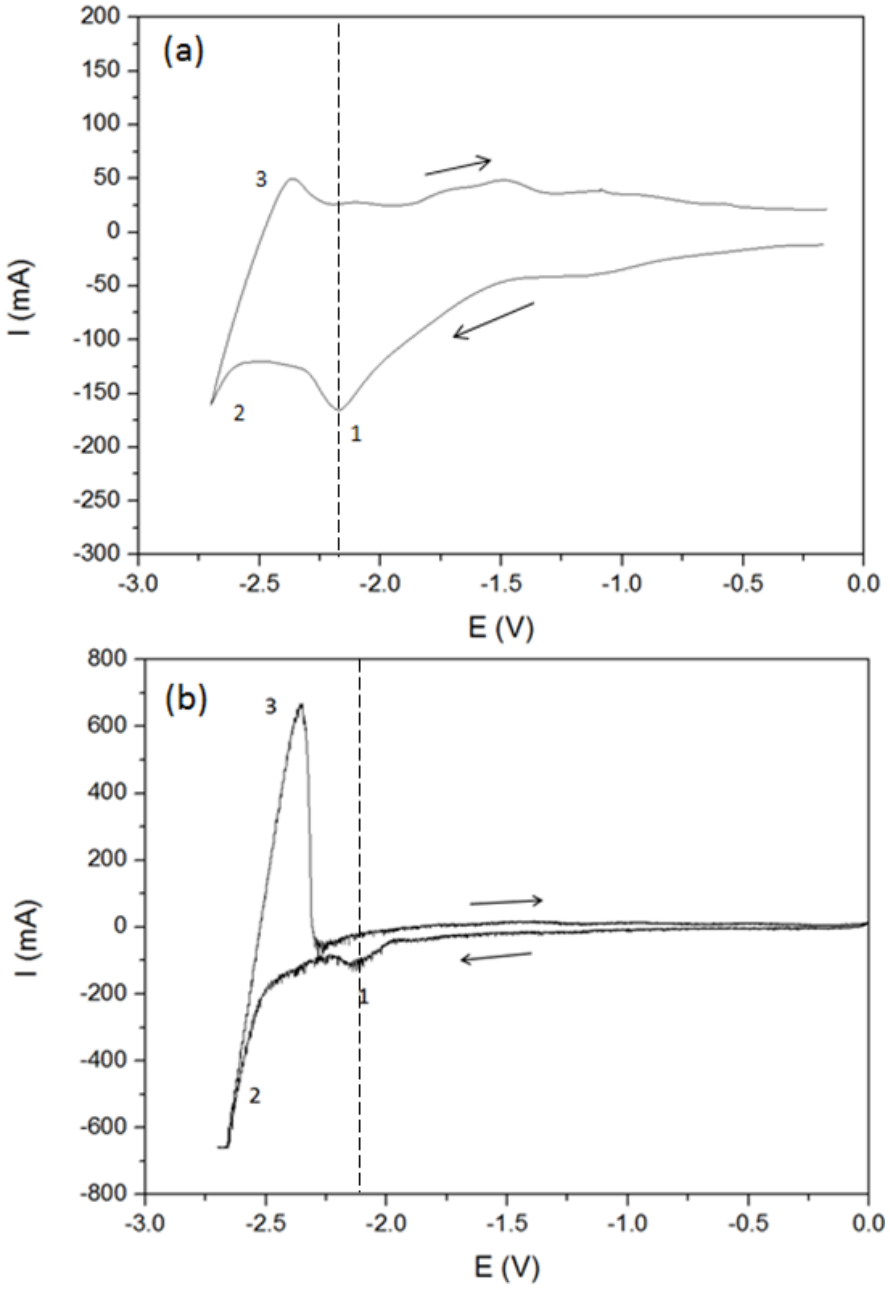

Figure 5.4 - (a) Cyclic voltammogram of WO_3 thin film cathode in LiCl-KCl eutectic at 450 °C, scan rate: 50 mV s^{-1}, reference electrode: Ag/Ag^+. (b) Cyclic voltammogram of WO_3 fluidised cathode in LiCl-KCl eutectic at 450 °C, scan rate 50 mV s^{-1}, reference electrode: Ag/Ag^+.

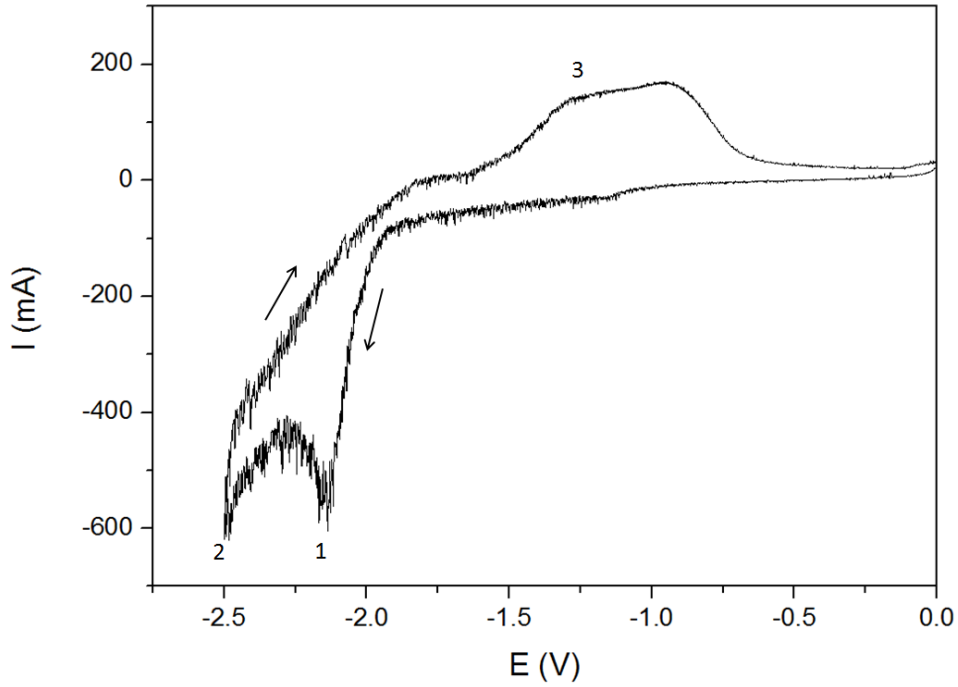

Figure 5.5 - Cyclic voltammogram of WO_3 fluidised cathode in LiCl-KCl eutectic at 450 °C, scan rate: 50 mV s^{-1}, and reference electrode: Ag/Ag^+.

Looking closer at the voltammetry of the fluidised cathode system, scanned from 0 V to -2.5 V and back to 0 V, Figure 5.5, provides a better understanding of the process. The main reduction peak appears at -2.14 V again. The apparent 'noise' or peaks in the voltammetry are due to particle-current collector collisions and reactions. One can see that the collision-reaction features are only evident at voltages where WO_3 can be reduced; indicating that the reoxidation to WO_x is primarily a surface process involving W on the surface and not as a result of reduced W particles colliding and reacting with the electrode. Looking closely at the cyclic voltammogram, one can see that the electrochemical reaction proceeds from actually -1.13 V, the noise in the diagram is also indicative of this. When comparing the voltages involved with the thermodynamically calculated ones and the predominance diagram, it suggests that the process starts with an electrochemical reaction, Equation 5.1, which produces WO_2. This then proceeds to reduce electrochemically to W metal in a 4-electron-transfer step, Equation 5.2.

Usually, an electrochemical reduction process progresses vertically down the predominance diagram; however, in reality it is much more complicated than that, and it normally propagates to the left and down as the reactions resume. Previous studies [55, 58, 59] where solid precursors have been removed from the melt mid-reduction and analysed have shown that; in the case of tungsten reduction seems to occur directly from WO_3 to WO_2 to W metal; and in the case of titanium reduction, the perovskite $CaTiO_3$ is formed in much smaller quantities than predicted by predominance diagrams, at the beginning of the reduction process. This is due to the fact that predominance diagrams fail to take into account the kinetics of processes and the overpotentials involved in refractory metal production.

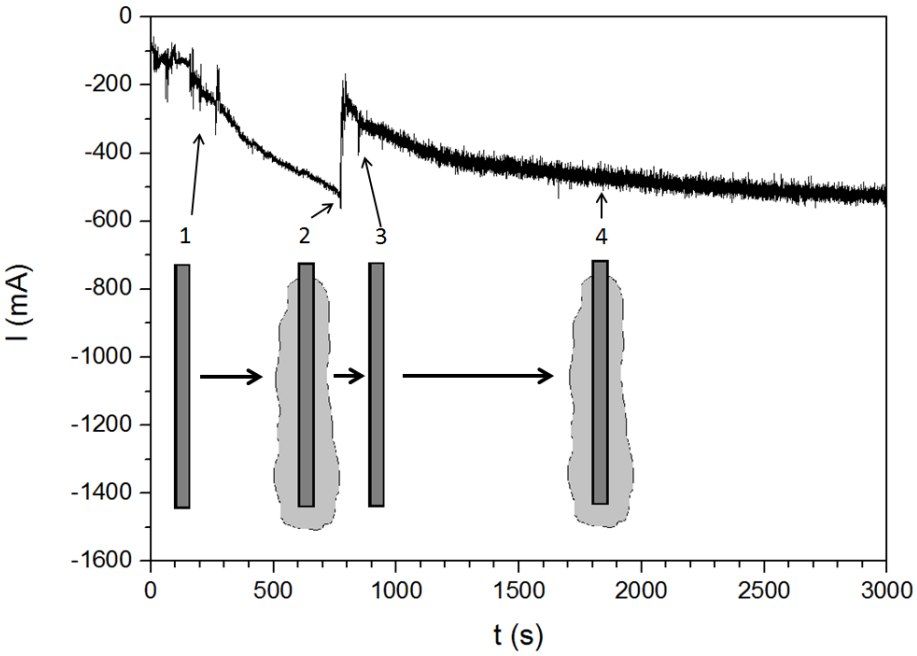

Figure 5.6 - Chronoamperogram of WO_3 fluidised cathode in LiCl-KCl eutectic at 450 °C, 40 g WO_3, argon flow rate: 800 cm^3 min^{-1}, set voltage: -2.14 V, reference electrode Ag/Ag^+. 1 - 4: diagrammatic representation showing the evolution of the cathode's surface area over time.

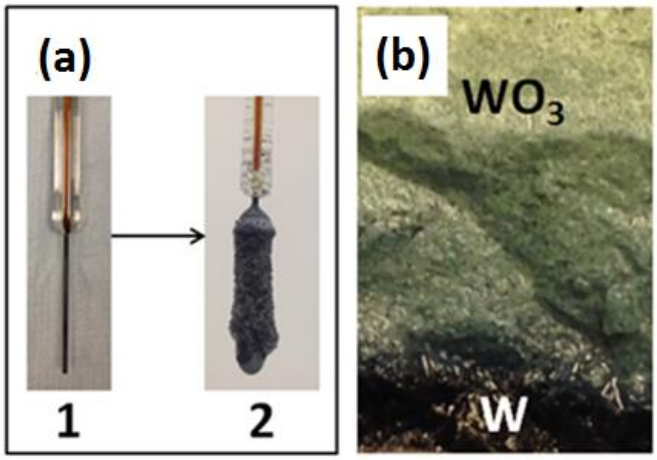

Figure 5.7 - (a) Photographs of current collector before the reduction process, 1, and after, 2, (b) photograph of the solidified melt showing separate layers of WO_3 and W.

Constant potential of -2.14 V, as identified as the reducing potential, (vs. Ag/Ag^+ reference electrode) was applied to the fluidised cathode system, Figure 5.6, this time 40 g of WO_3 powder was fluidised. In previous studies [47, 50, 52, 170] potentials in the range of 2 – 3 V were normally applied for such metal oxide reduction processes. As time passed, the current increased due to an increase in the electrode surface area and the deposit growth of W on the current collector surface, as illustrated in Figure 5.6 (1-2). This growth is visible through the glass electrolytic cell set-up. At (2) in Figure 5.6, there is a rapid reduction in current associated with spalling off of the deposit from the electrode. New growth is then associated with the increase in the current (3-4).

Due to the difference in densities, when the electrolyte is left to solidify, different layers of materials form, Figure 5.7 (b). Dark metallic tungsten metal sinks to the bottom, followed by a layer of green, still to be reduced, tungsten oxide, and finally a layer of LiCl-KCl eutectic. This represents a potentially simple means of separating the product in a technological system. Figure 5.7 (a) shows an image of the current collector before, 1, and after the reduction, 2.

There are two areas from where the final product could be collected, the bottom of the cell crucible, Figure 5.7 (b), and on the surface of the working electrode, Figure 5.7 (a). Samples from both were analysed using SEM and EDS (Carl Zeiss

XB1540, accelerating voltage = 20.00 kV, dwell time = 1.6 min). In the EDS spectrum of the deposit's surface on the working electrode, Figure 5.8, no oxygen was detected. However, there is some salt present. Figure 5.9 (a) shows an SEM image of the as-received WO_3 particles and (b) that of the W product from the solidified melt. No oxygen was detected in the EDS spectrum of the surface of the W product.

A cross-section of the retrieved current collector, where the deposit did not spall off, Figure 5.10, shows that the growth is cylindrical in shape, i.e. it forms at the same rate perpendicular to the current collector surface in all directions. When zoomed in, Figure 5.11, the particles of W metal produced appear homogeneous in size and porosity.

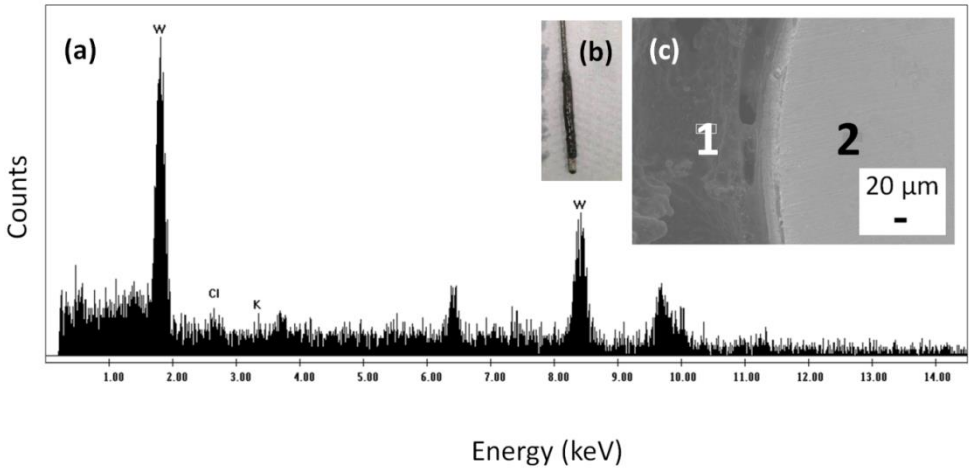

Figure 5.8 - (a) EDS spectrum of the deposit on the current collector's surface. (b) Photograph of the working electrode after the chronoamperometry showing the deposited W. (c) SEM image of the cross-section of the solid W working electrode, 2, and the deposit grown, 1.

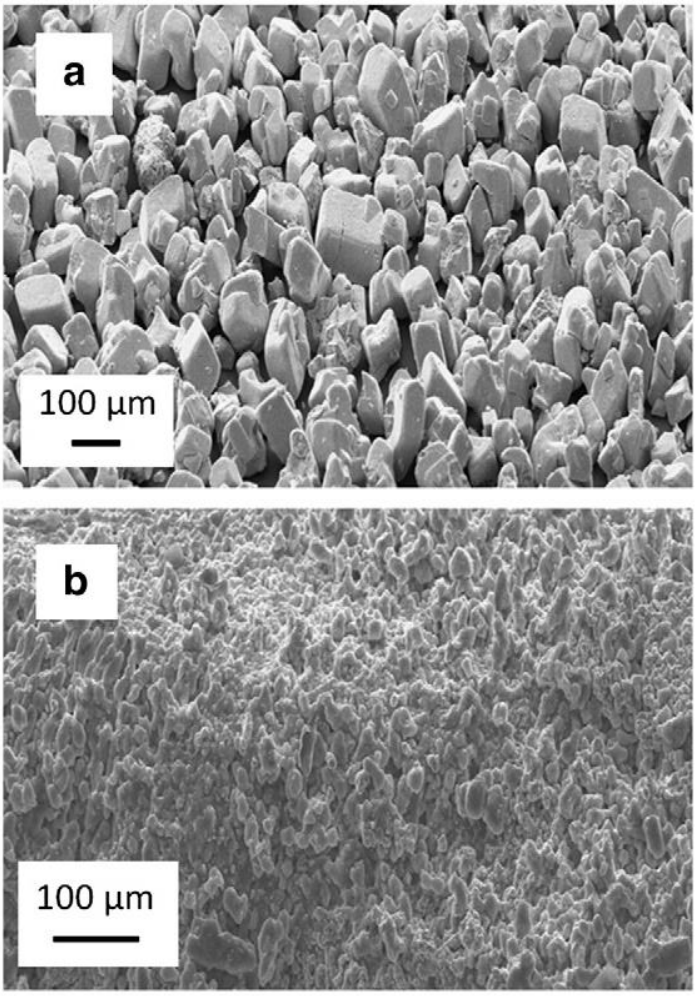

Figure 5.9 – SEM image of the as-received WO_3 particles, and (b) product W obtained from the solidified melt as a separate layer to the LiCl-KCl. EDS spectra (penetration depth ~6 µm) showed the stoichiometric composition of WO_3 in (a), and the absence of oxygen in (b).

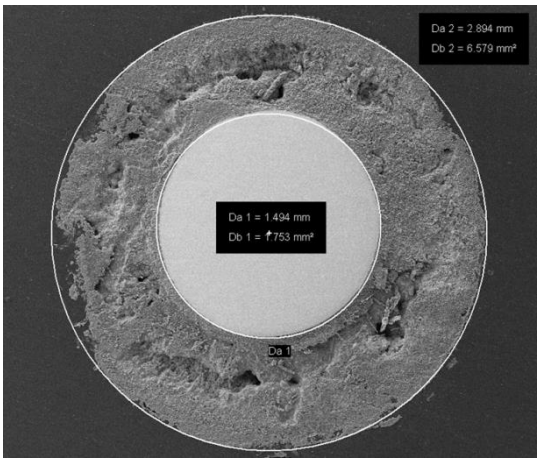

Figure 5.10 - SEM image of the cross-section of the current collector showing the deposited tungsten.

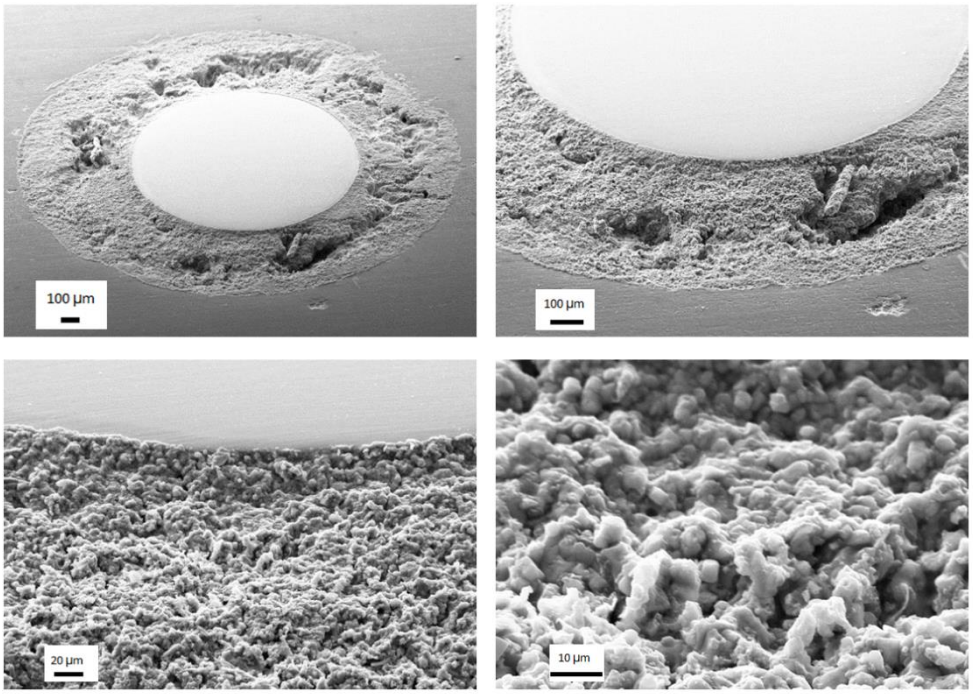

Figure 5.11 - SEM images of the current collector and deposit, at different magnitudes, showing the homogeneity of reduced deposit.

5.3.1 Current efficiency

A constant potential of -2.14 V (vs. Ag/Ag^{+}) was applied to the fluidised cathode set-up to reduce 4 g of WO_3 to W metal, Figure 5.12. The chronoamperogram shows a similar trend to previously published work on electrochemical reduction of metal oxides [58], where the diagram can be segregated into two main sections; the first, where rapid reduction reactions occur and the current increases significantly until it reduces; the second, where the current increases slightly again, then plateaus and slower reactions take place to reduce the final oxides, until the current decreases indicative of the end of the process and the production of pure metal.

Assuming 100% current efficiency, it would require a charge of 9977.5 C to be applied to fully reduce all 4 g of WO_3. The XRD spectrum of the final product, retrieved from the deposit on the current collector, is presented in Figure 5.13. It shows the spectra of W and KCl. Most importantly, the analyses show that there is no WO_3, WO_2 or any other quasi-reduced species. Thus, it confirms that the reduction reaction can reach completion with pure W being the product. The Faradaic efficiency of the process was calculated by dividing the theoretical charge required by the charge passed. The charge passed was calculated by adding the actual charge passed to an assumed charge that would be passed given that the chronoamperometry was allowed to reach zero potential. Experiments concluded that the current efficiency for reducing WO_3 to W in LiCl-KCl using the fluidised cathode process is ~ 82%. The current efficiency was also calculated by subtracting the background current as estimated from the pre-electrolysis, this was 4.3 mA, as presented in Figure 5.12(b). This reduces the errors from the estimated extended current, and gives a new current efficiency of 100%. Thus the current efficiency is 82-100%

When the final product was retrieved, a sample was placed in ethanol to dissolve the salt, under an argon atmosphere. Dissolving the salt in water

was not appropriate in this case, as W, unlike Ti, reacts more readily with water (and air) forming thin films of oxides, which was not desired for analysis. After leaving the sample in ethanol for 24 hr, the ethanol containing salt was filtered out using a small vacuum filtration unit. The sample (powder) was then placed in ethanol again, and the procedure was repeated twice. Finally, the product was dried in a vacuum oven at room temperature. Despite this rigorous cleaning process, the XRD spectrum in Fig. 12 confirms that KCl is still present in the sample. A solution to this could be to employ a vacuum distillation [172, 173] unit at a high temperature to remove the salt whilst still molten. The nature of the fluidised cathode would complement such a filtration technique.

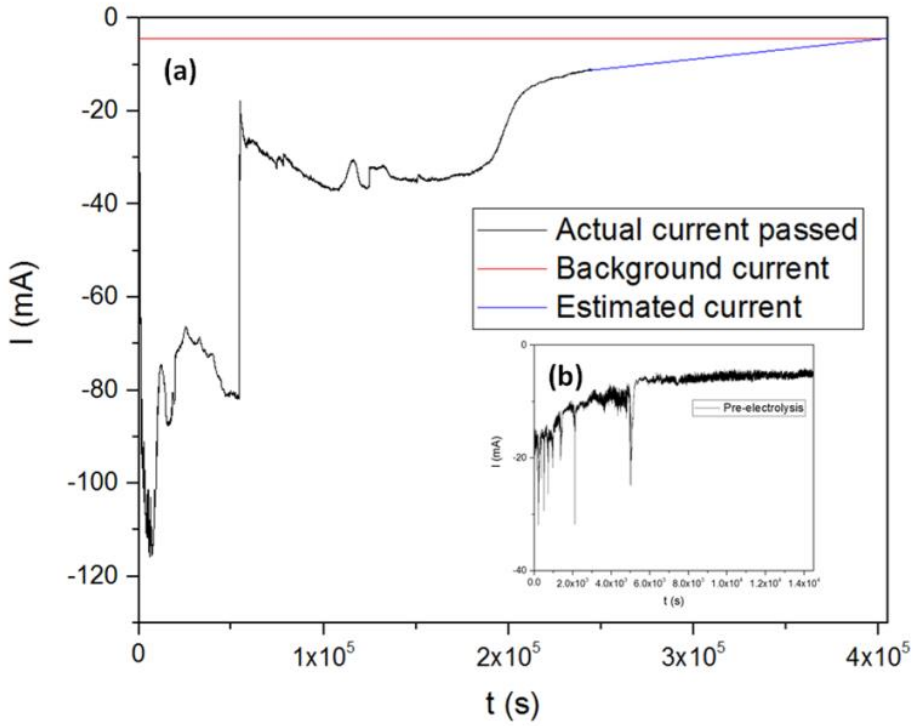

Figure 5.12 - Chronoamperogram of WO_3 fluidised cathode in LiCl-KCl eutectic at 450 ˚C, 4 g WO_3, argon flow rate: 800 cm^3 min^{-1}, reference electrode: Ag/Ag^+, set voltage: -2.135 V.

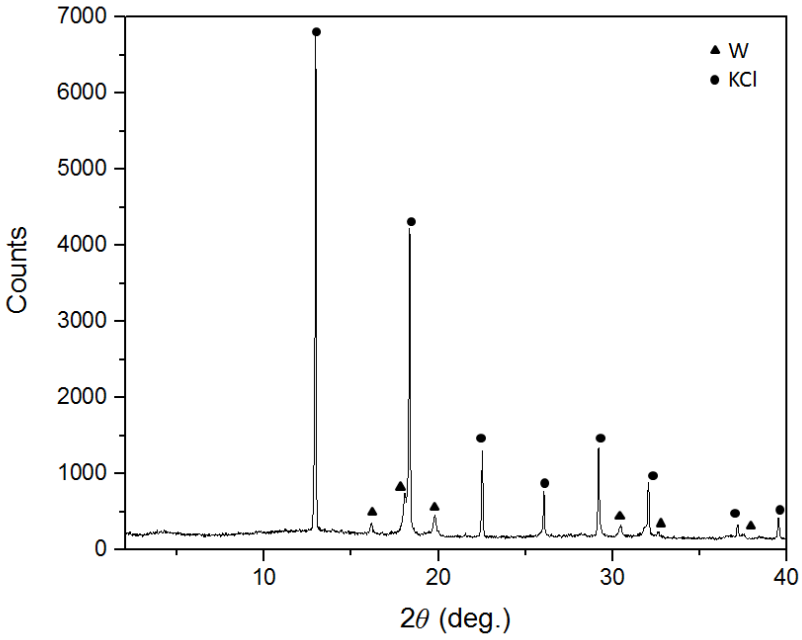

Figure 5.13 – X-ray diffraction spectrum (Mo Kα) of sample of product after complete reduction, showing W (52344-ICSD [174]), and KCl (165593-ICSD [127]).

5.3.2 Effects of metal oxide – salt ratio

Constant potential experiments were carried out on different loadings of WO_3 powder in LiCl-KCl salt eutectic. The voltage was again set to -2.14 V, Figure 5.14. Three chronoamperometry measurements were taken. Masses of WO_3 (0.5, 40 and 60 g) were initially mixed with 150 g of LiCl-KCl in the main cell crucible, with 10 g in the anode compartment, giving weight percentages of 0.312, 20.00 and 27.27 wt%, for the three different experiments. 0.5 g was chosen, as this was the lowest limit at which some product could still be retrieved from the current collector. 60 g was chosen, as this was the highest limit, given the ratio to 150 g of salt, where the fluidisation process was still easily initiated. Although masses of up to 100 g of WO_3 could still be fluidised, they proved difficult for fluidisation initiation and maintaining via gas bubbling.

The chronoamperograms show the same characteristic of an initial increase in current. However, they all stabilise towards different currents, with the lowest weight percentage achieving a lower current, than the higher weight percentage

experiments. Spalling-off is also witnessed, with associated sudden drops in currents passed. The effect of metal oxide concentration in the melt on the electrochemistry is attributed to the fact that statistically there are more frequent interactions of particles with the electrode for a system with higher loading, thus giving a higher total current. The difference in change in current with time is more intriguing. The high oxide concentration leads to a monotonic increase in current with time, while the lower concentrations show more signs of product spalling, evident through the abrupt decrease in current. This would suggest that the product is more stable in the high concentration case, allowing growth to continue and the electrode to grow. At higher loadings the bulk density of the materials in the reaction crucible is higher, which would hinder the current collector from vibrating heavily, due to mechanical agitation via bubbling and collisions, which also contributes to the spalling effect.

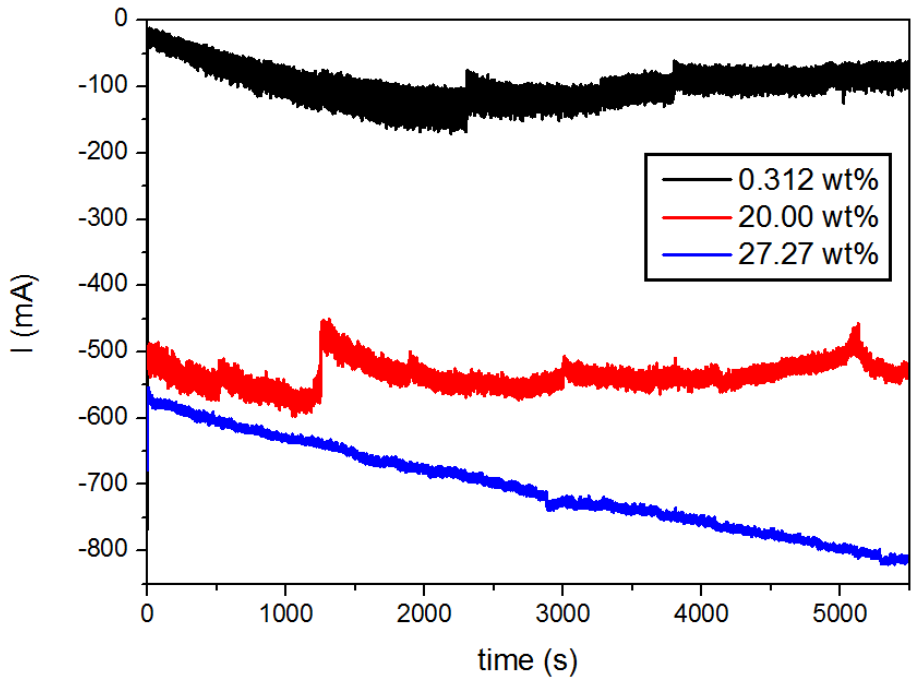

Figure 5.14 - Chronoamperograms of WO_3 fluidised cathode in LiCl-KCl eutectic at 450 °C, argon flow rate: 800 cm^3 min^{-1}, reference electrode: Ag/Ag^+, set voltage: -2.14 V, for different weight percentages of WO_3 in the melt, as indicated.

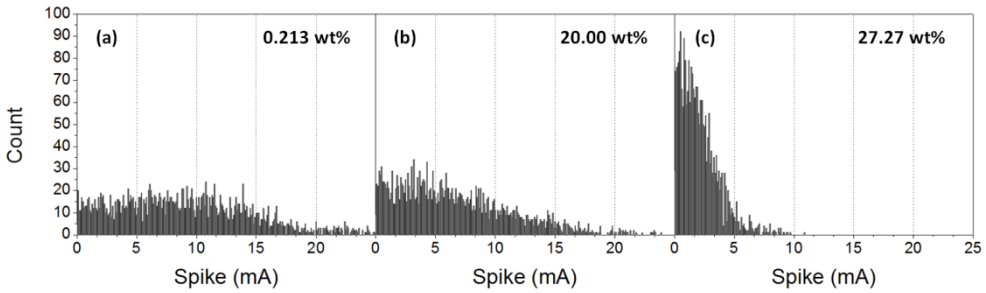

Figure 5.15 - Count of charge per spike relative to a normalised line of best fit, at different WO_3 – LiCl-KCl eutectic ratios. Where, (a) is at 0.312 wt% WO3, (b) 20.00 wt%, and (c) 27.27 wt%.

Figure 5.15 shows the count of charge per spike relative to a normalised line of best fit for the chronoamperograms in Figure 5.14. 2500 points for each WO_3 concentration were used to produce the data. It is very clear that with higher concentrations the spike amplitude is much smaller. The increasing noise with the decreasing oxide particle fraction is also attributed to the greater particle homogeneity in the melt leading to a steadier current response. Thus, the noise feature in the fluidised cathode process is attributed to the velocity (how long a particle stays on the surface) with which the particles collide with the current collector, rather than the number of particles impinging at any given point, although each spike corresponds to more than one particle colliding.

5.3.3 Effects of fluidisation rate

Different argon flow rates were applied to the fluidised cathode process whilst conducting a constant voltage experiment. Figure 5.16 shows the chronoamperogram of the fluidised cathode under different agitation conditions. The reducing potential was set to -2.14 V and the fluidisation rate was altered by changing the argon flow rates from 200 cm^3 min^{-1} to a maximum of 1800 cm^3 min^{-1}, and back to 200 cm^3 min^{-1}. It was increased by 200 cm^3 min^{-1} every 5 minutes. As time passed, the current increased, at each argon flow rate; again this is due to an increase in the surface area of the current collector. It is evident that increasing

the agitation rate causes the current to increase more rapidly, and makes the collision-reaction spikes (noise) greater. This indicates that a higher fluidisation rate increases the likelihood of an encounter of an oxide particle with the electrode, and will also increase the kinetic energy of particle collision with the electrode. These effects are particularly acute above a threshold agitation level induced by an argon flow rate of 1600 $cm^3 min^{-1}$. In fluidised bed chemical engineering, there are two main types of fluidisation regimes, depending on many parameters, but mainly the superficial velocity of the fluid, the fluidisation regime can change from a 'particulate' to an 'aggregative' regime. This could be the explanation for such an obvious change in the chronoamperommetry measurements. Further studies should be conducted on the fluidisation regimes and their parameters, identification and outcomes, to help understand the complexity of this system with three phases of flow (including changes in density and other parameters, when electrochemical alterations are applied).

Figure 5.17 shows the count of charge per spike relative to a line of best fit for the chronoamperogram in Figure 5.16. Three hundred points for each argon flow rate were used to plot the data. Here, one can clearly see that in the case of lower flow rates the spikes are much smaller and lie toward the lower end of the charge per spike spectrum. The opposite is true for higher agitation rates. This complements the theory that the noise feature in the fluidised cathode process is a result of higher impact velocity/kinetic energy. Thus, the effects of altering the fluidisation rates are in agreement with metal oxide loading effects. Higher frequencies of collision-reactions are responsible for electrode growth and current increase; and higher impact velocities are responsible for higher noise, and ultimately spalling effects.

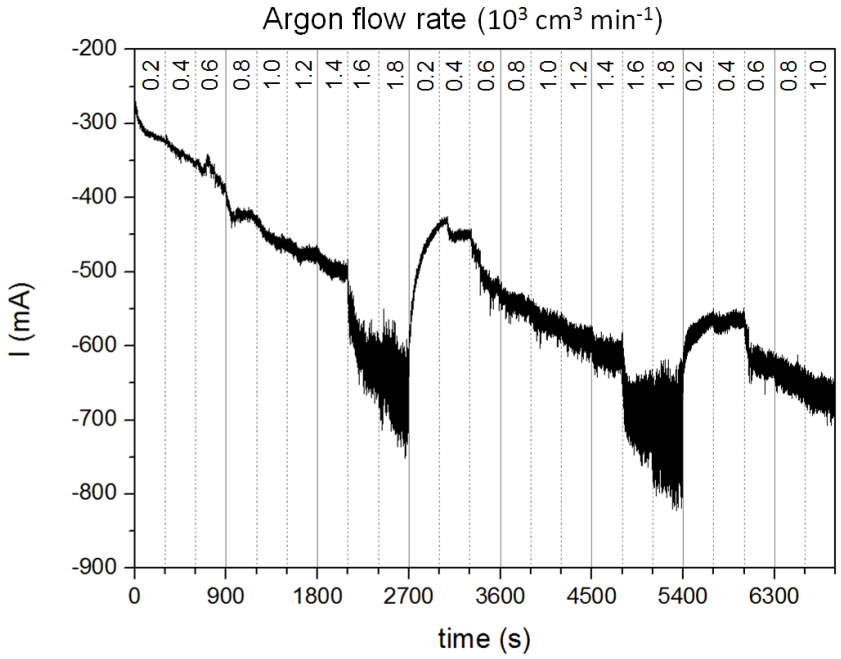

Figure 5.16 - Chronoamperogram of WO_3 fluidised cathode in LiCl-KCl eutectic at 450 ˚C, 40 g WO_3, reference electrode: Ag/Ag^+, set voltage: -2.14 V, showing the effect of different argon flow rates bubbled through the melt.

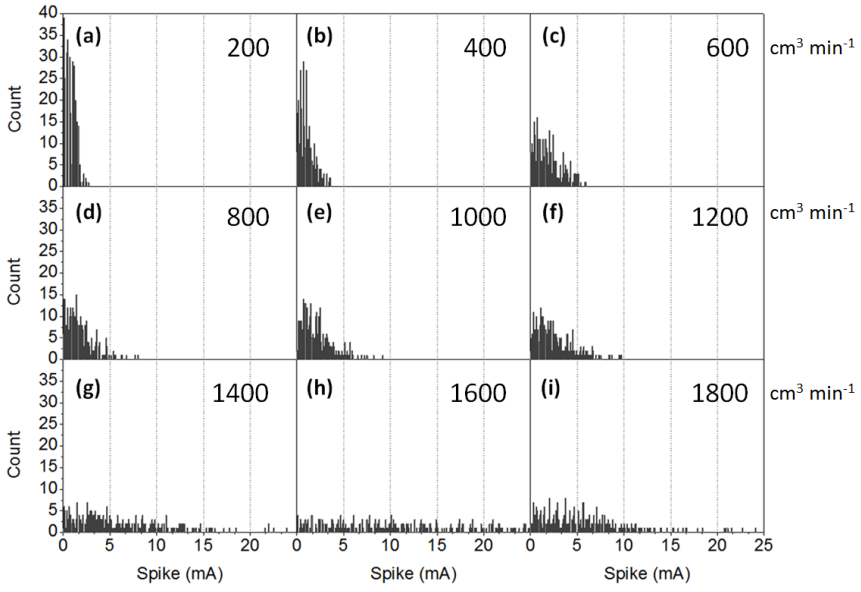

Figure 5.17 - Count of charge per spike relative to line of best fit, at different argon flow rates. Where, (a) is at 200 cm^3 min^{-1}, (b) 400 cm^3 min^{-1}, (c) 600 cm^3 min^{-1}, (d) 800 cm^3 min^{-1}, (e) 1000 cm^3 min^{-1}, (f) 1200 cm^3 min^{-1}, (g) 1400 cm^3 min^{-1}, (h) 1600 cm^3 min^{-1}, and (i) 1800 cm^3 min^{-1}.

5.3.4 Particle coulometric analysis

Particle coulometric analysis [175-178] was carried out on a section of 200 spikes from the chronoamperometry in Figure 5.18 to characterise the particle-electrode interaction dynamics. This section is presented in Figure 5.18 (b). Figure 5.19 (a) shows the relative frequency of spike durations. The modal spike duration time is 0.4 s with a standard deviation of 0.2. Using Equation 5.10, the charge per spike was calculated. This is presented in Figure 5.19 (b). The modal charge per spike is -0.2 C with a standard deviation of 0.1.

$$Q = \int Idt = ezN \tag{5.10}$$

Where I is the current, t the spike duration, e the electronic charge = 1.602×10^{-19} C, z = 6 (the number of transferred electrons per reduced formula unit of WO_3), and N is the number of reduced WO_3 units.

Assuming each spike on the chronoamperogram is only associated with one particle impacting on the current collector, and that the particles are spherical in shape, and fully reduced, Equation 5.11 can be used to estimate the size of the WO_3 particles colliding with the working electrode, via cathodic coulometry.

$$r = \sqrt[3]{\frac{3MQ}{4\pi eN_A z\rho}} \tag{5.11}$$

Where r is the radius of the WO_3 particles, M = 231.84 g mol^{-1} (the molar mass of WO_3), N_A = 6.022×10^{23} mol^{-1} (the Avogadro constant), ρ = 7.16 g cm^{-3} (the density of WO_3).

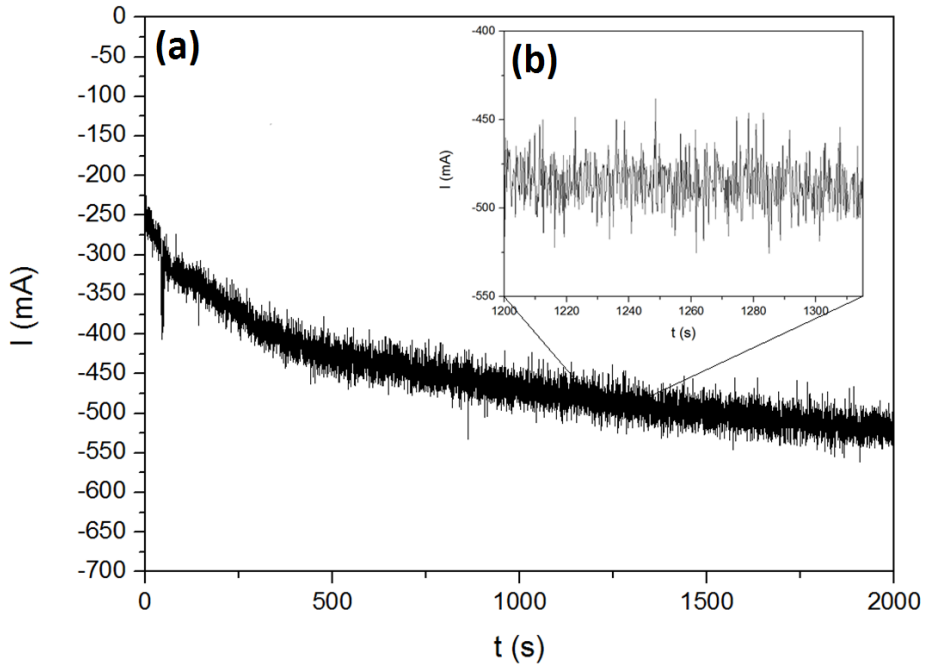

Figure 5.18 - (a) Chronoamperogram of WO_3 fluidised cathode in LiCl-KCl eutectic at 450 ˚C, 40 g WO_3, reference electrode: Ag/Ag^+, set voltage: -2.14 V, (b) zoom-in of a section containing 200 spikes used for coulometric analysis.

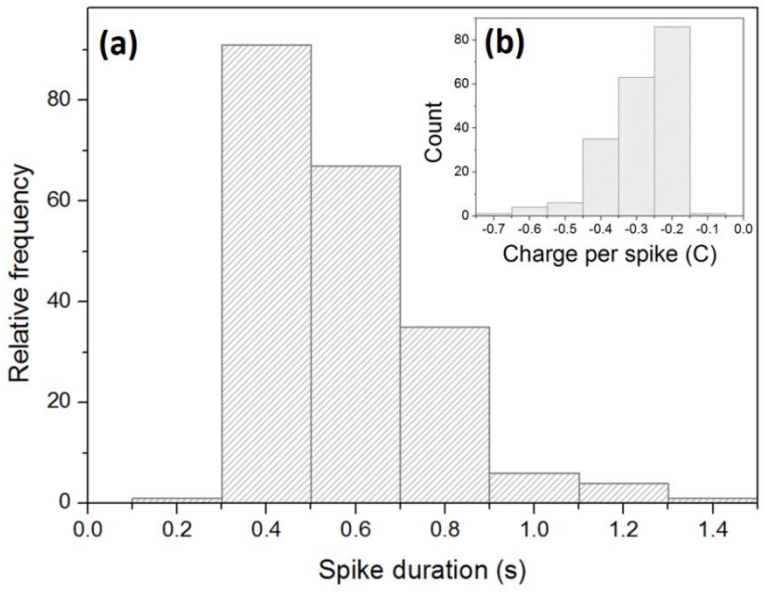

Figure 5.19 - (a) Relative frequency of spike durations in Figure 5.18 (b) from coulometric analysis. (b) Count of charge per spike from coulometric analysis.

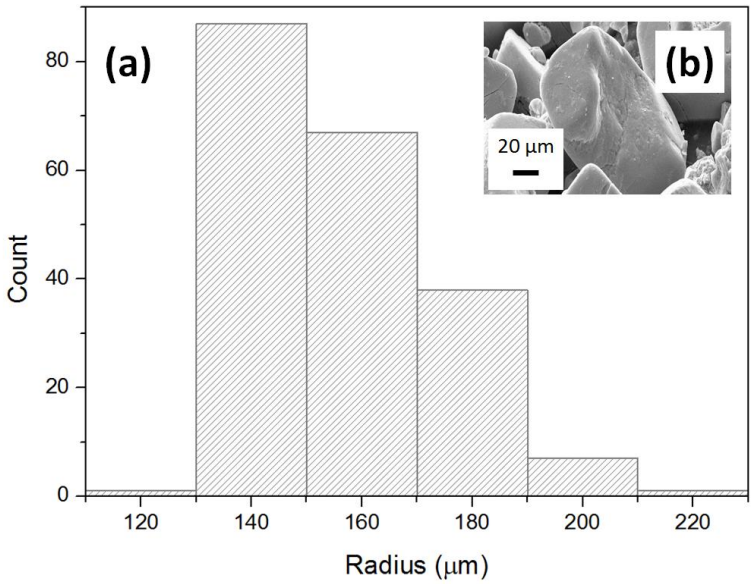

Figure 5.20 - (a) Count of radii sizes of WO_3 reactant particles from particle coulommetry analysis. (b) SEM image of a large WO_3 particle.

Figure 5.20 (a) shows the count of radii sizes as estimated from particle coulometry. The mean radius size of WO_3 is 154.5 μm with a standard deviation of 17. An SEM image of a large WO_3 particle is shown in Figure 5.20 (b).

Particle size distribution analysis, Figure 5.1, showed that the actual mean particle radius size is 15.41 μm. This discrepancy in results is expected because in the literature, particle coulometry was used to predict the size of nano particles impending on electrodes, whereas in the fluidised cathode system, where diffusion of particles (in the micro scale) is enhanced via agitation of the melt, more than one particle would be expected to collide with the current collector at any given stretch of 0.2 s. Nonetheless, particle coulometry still provides a valuable understanding of the system, as it concludes that on average, given the conditions applied in the chronoampergram in Figure 5.18, a number of particles that amount to the size of one spherical particle of 154.5 μm would impenge on the current collector at any time band of 0.2 s and be fully reduced.

5.3.5 Electrochemical deposition model

An electrochemical deposition model for the fluidised cathode process was developed in order to estimate the rate of growth of the deposit on the working electrode, and the porosity characteristic of the deposit.

Assuming that the current density is constant across the entirety of the electrode at different extents of reaction, the current, *i*, is related to the molar accumulation over a given time, *N(t)*, by Equation 5.12.

$$i = nF\frac{d}{dt}N(t) \qquad 5.12$$

Where, *n* is the number of moles and *F* is the Faraday constant.

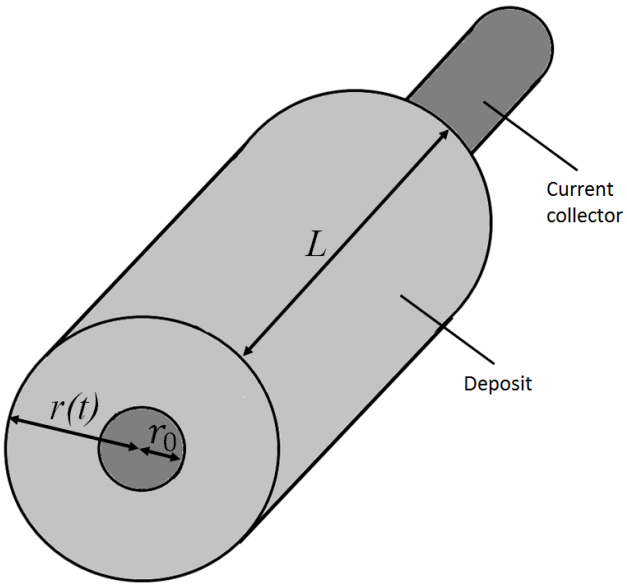

Figure 5.21 – Schematic showing parameters of the current collector and the deposit used in the electrochemical deposition model.

The volume deposited, *V(t)*, is represented in Equation 5.13, and in terms of radii in Equation 5.14, assuming the deposit is cylindrical in shape, perpendicular to the

current collector surface, Figure 5.21, which is in fact the case, as shown in Figure 5.10.

$$V(t) = \frac{N(t)M}{\rho} \quad 5.13$$

$$V(t) = \pi[r(t)^2 - {r_0}^2]L \quad 5.14$$

Where, M is the molar mass, ρ is the density, r_0 is the initial radius of the electrode, *r(t)* is the radius after time, *t*, and *L* is the active length of the electrode. Combining Equations 5.12, 5.13 and 5.14, Equations 5.15 and 5.16 can be derived.

$$\frac{d}{dt}r(t)^2 = \frac{iM}{\pi LnF\rho} = constant\ k \quad 5.15$$

$$r(t) = \sqrt{kt + {r_0}^2} \quad 5.16$$

Figure 5.23 is a plot of the electrochemical deposition model, with data (current) acquired from the chronoamperommetry in Figure 5.22. It shows the evolution of the working electrode's radius size as time passes. With a starting radius of 0.75 mm, the model depicts that the final radius size after the electrolysis process is 1.90 mm. the size of this particular electrode was measured after experimentation with no observed spalling off of the product, however, and was ~ 5.00 mm. This can be attributed to a few reasons, such as the deposition morphology. Thus, the model as it stands is not conclusive. Hence a more comprehensive deposition model should be developed.

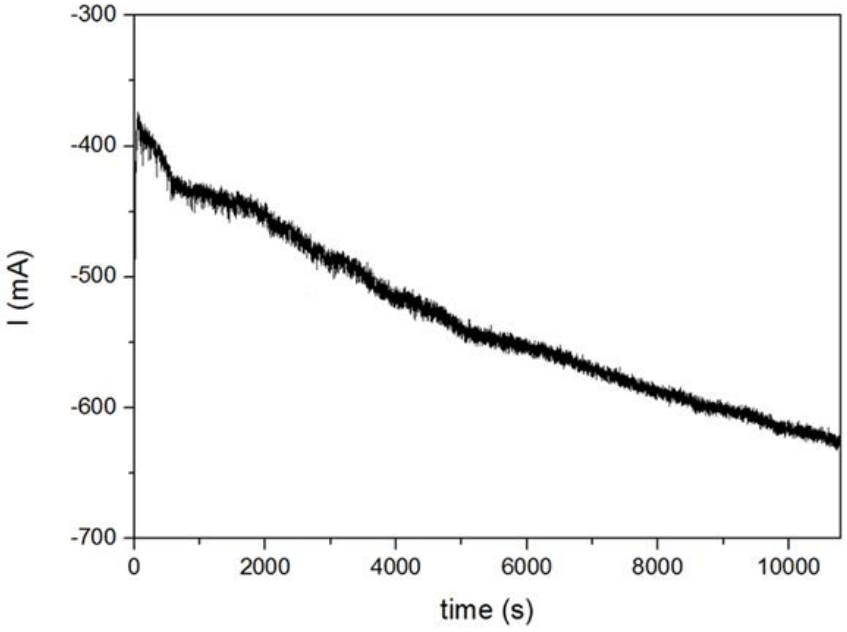

Figure 5.22 - Chronoamperogram of WO_3 fluidised cathode in LiCl-KCl eutectic at 450 ˚C, 40 g WO_3, argon flow rate: 800 cm^3 min^{-1}, reference electrode: Ag/Ag^+, set voltage: -2.14 V.

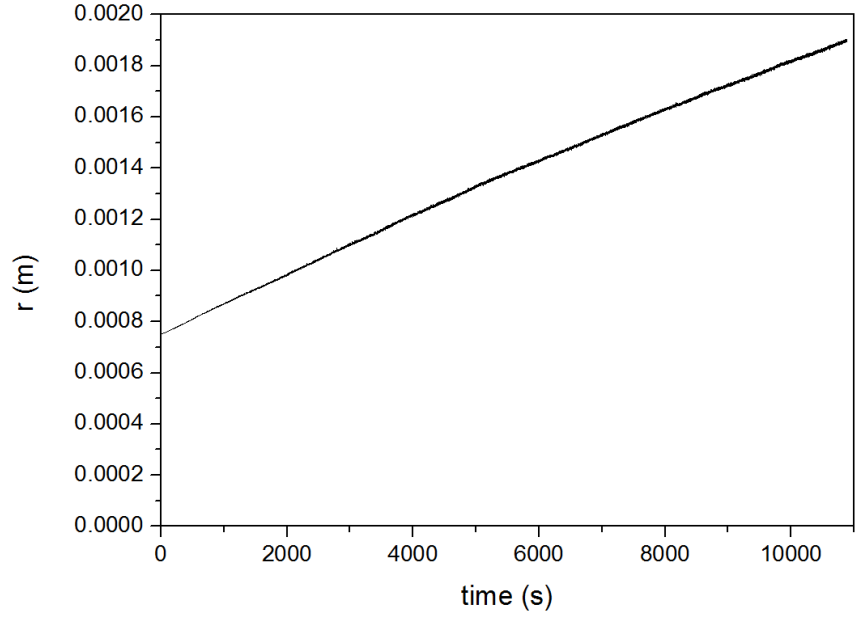

Figure 5.23 – Deposit growth on current collector over time, predicted via electrochemical deposition model.

5.4 Conclusions

The electrochemical reduction of WO_3 to W metal has been assessed, and it likely to occur following the reactions $WO_3 \rightarrow WO_2 \rightarrow W$, Equations 5.1 and 5.2. A full reduction using the fluidised cathode process, with complete conversion of the product to W has been achieved, via applying a constant potential of -2.14 V. The Faradaic current efficiency of the process has been established, and found to be ~ 82%. The reduction process is split into two sections; the first where rapid reduction of WO_3 occurs, the second where a slower reduction of the remaining oxides in the product are removed. The deposited material on the current collector is in the form of homogeneously distributed particles.

Increasing the metal oxide – salt ratio results in increasing current (faster deposit growth on the current collector), and decreasing collision-reaction noise, and in less likelihood for product to spall off. Increasing the fluidisation rate of the process results in an increase in the rate of deposit growth, as well as a greater collision-reaction noise. The two main observations to take from this are:

a. The deposit growth, and ultimately the current increase, is dependent on the frequency of particle – current collector collisions and reactions.

b. The collision-reaction noise (spikes) is dependent on the velocity at which the particles collide with the current collector. Spalling of the product is also highly affected by this.

Thus, depending on the desired means of recovery of the product, i.e. a continuous flow retrieving or batch via removal of electrodes, these conditions can be altered to suit.

Particle coulometric analysis shed some insight onto the process in terms of total volume of particles impending on the current collector at any given time. An electrochemical deposition model was also developed to estimate the porosity of the deposit and the rate of its growth over time.

The fluidised cathode is a robust, three-phase, high efficiency process. It has been studied here for the electrochemical reduction of tungsten oxide, however, it is likely applicable for other refractory metals (such as titanium), and in the nuclear industry for pyroprocessing purposes of spent nuclear materials.

In the following Chapter, the electrochemical reduction of UO_2 to U metal is investigated, the reaction pathways determined, and the fluidised cathode process is used for the reduction process.

6. The Electrochemical Reduction of Uranium Oxide

The electrochemical reduction of UO_2 to U metal using a fluidised cathode process was investigated. Voltammetry studies were conducted, and alongside a predominance diagram that was constructed, the reaction path-way was studied, using both, a fluidised cathode process and a packed metallic cavity electrode precursor set-up. The route that the reduction process follows depends on pO^{2-} and potential, which is highly influenced by the type of metal oxide precursor used.

The main reduction potential using the fluidised cathode appeared to be -2.2 V (vs. Ag/Ag^+ reference electrode). A Faradaic current efficiency for the process was established, and found to be ~ 92%. It is proposed that the reduction process is split into three stages; the first where a seeding process takes place at a low potential to allow for the reduced uranium particles to be deposited onto the tungsten current collector; the second where rapid reduction of UO_2 particles occurs with a growth in electrode size, accompanied by an increase in current total being passed; the third where a slower reduction of the remaining oxides in the product takes place.

6.1 Introduction

High temperature molten salt reprocessing technology (pyroprocessing) offers a range of advantages when compared to aqueous reprocessing techniques. This is due to the fact that the technology is inherently ‘safe’ as it is resistant to proliferation and does not provide an environment for criticality accidents to occur; it also utilises compact easily accessible facilities. Molten salts pyroprocessing is described in more detail in Chapter 2.

There is a clear motivation for implementing Generation IV nuclear reactors, which require metal as start-up fuel and follow a fully integrated and safe reactor and reprocessing design arrangements; hence, advances in the technology are made. A conceptual flowsheet for the pyrochemical treatment of used LWR fuel, as described by ANL [179], is presented in Figure 6.1. The spent nuclear fuel, in the

form of oxide pellets, is chopped and then passed on to an electrolytic reduction step. The uranium is in the form of UO_2; hence, the reduction of UO_2 to U metal is studied in this Chapter. The reduced species are then processed in an electrorefiner, also described in Chapter 2, where U product and other transuranic species are recovered for enriching and recycling into new fuel. The flowsheet comprises some recycling streams and a salt distillation step as well.

Previous studies on the electrochemical reduction of spent nuclear fuel oxides and uranium oxides are reported in detail in Chapter 2. In this Chapter, the electrochemical reduction of UO_2 to U metal in LiCl-KCl molten salt eutectic is investigated, using both metallic cavity electrodes (MCE's) and the fluidised cathode process. The reduction pathways and the current efficiency are also reported.

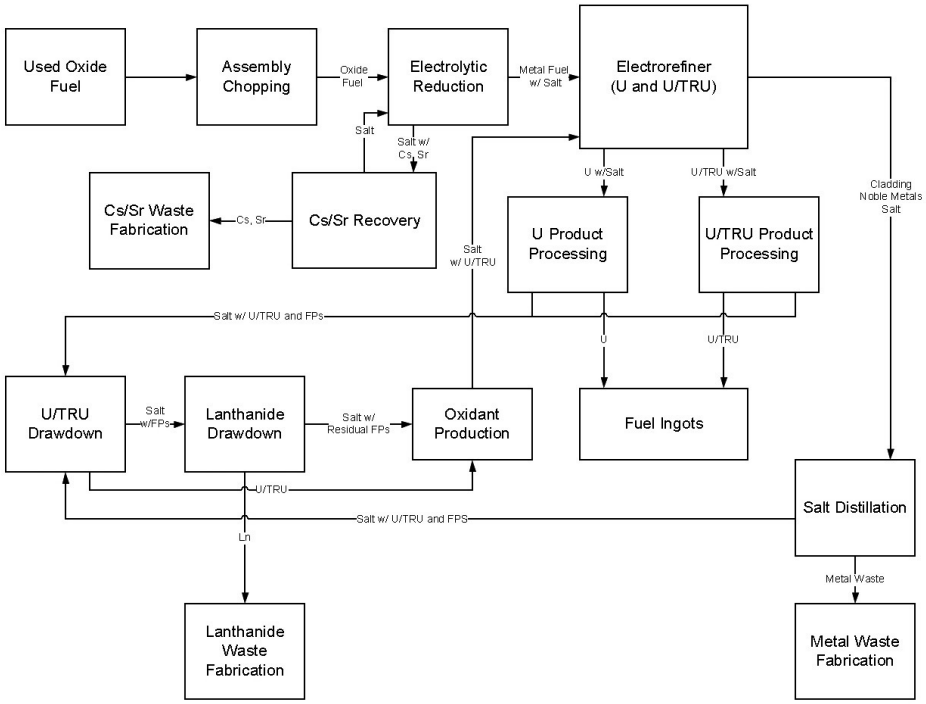

Figure 6.1 – Conceptual flowsheet for the treatment of used LWR fuel [179].

6.2 Experimental

6.2.1 Apparatus

A schematic of the electrolytic cell used is illustrated in Figure 3.13 (b). The cathode consists of UO_2 particles that are suspended in the molten salt (LiCl-KCl) eutectic, and a pure tungsten rod current collector. The anode is a graphite rod separated in its own compartment to avoid reoxidation of the reduced uranium particles. The melt is agitated via a flow of argon. A reference electrode (Ag/Ag^+) was used, and the temperature was monitored via a thermocouple that is immersed in the melt. All electrochemical tests were performed using a potentiostat (IviumStat, Ivium Technologies, NL).

The same set-up was used to carry out the metallic cavity electrode (MCE) experiments, Chapter 3. However, no UO_2 particles were employed, the counter electrode was not separated inside a compartment, no argon was bubbled through the melt, and the current collector was replaced with an MCE, Figure 3.13 (a). The cavities in the MCE were filled with UO_2 powder. The same powder was used for the fluidised cathode experiments.

6.2.2 Chemicals

All preparation steps were carried out under a sealed argon atmosphere. Anhydrous lithium chloride (ACS reagent, ≥99.0% purity, Sigma-Aldrich) and potassium chloride (≥99.5% purity, Sigma-Aldrich) were used for the electrolyte. The salt was dried in a vacuum oven at 200 ˚C for 24 h, then 150 g of 59-41 mol% LiCl-KCl were mixed with UO_2 (as received from the Centre for Radiochemistry Research, School of Chemistry, University of Manchester). Figure 6.2 shows the X-ray diffraction pattern of the as-received UO_2 powder. 15 g of LiCl-KCl was placed inside the anode compartment. The counter electrode was a high density graphite rod, 3.05 mm in diameter (99.9995% metal basis, Alfa Aesar). The working electrode (current collector) was a tungsten rod, 1.5 mm in diameter (99.95% metal basis, Alfa Aesar). A glass sheath around the shaft of the tungsten rod insured that a constant surface area of electrode is exposed to the electrolyte,

even when being agitated by the Ar stream. Argon (99.998% purity, BOC) was bubbled through the melt via a ceramic tube (5 mm internal diameter, Alsint).

For the MCE experiments, the electrolyte was composed of 150 g of LiCl-KCl, prepared in the same way as for the fluidised cathode setup, but no UO_2 particles were agitated in the melt. The cavities in the working electrode were filled with UO_2 powder by 'finger pressing' using two glass slides.

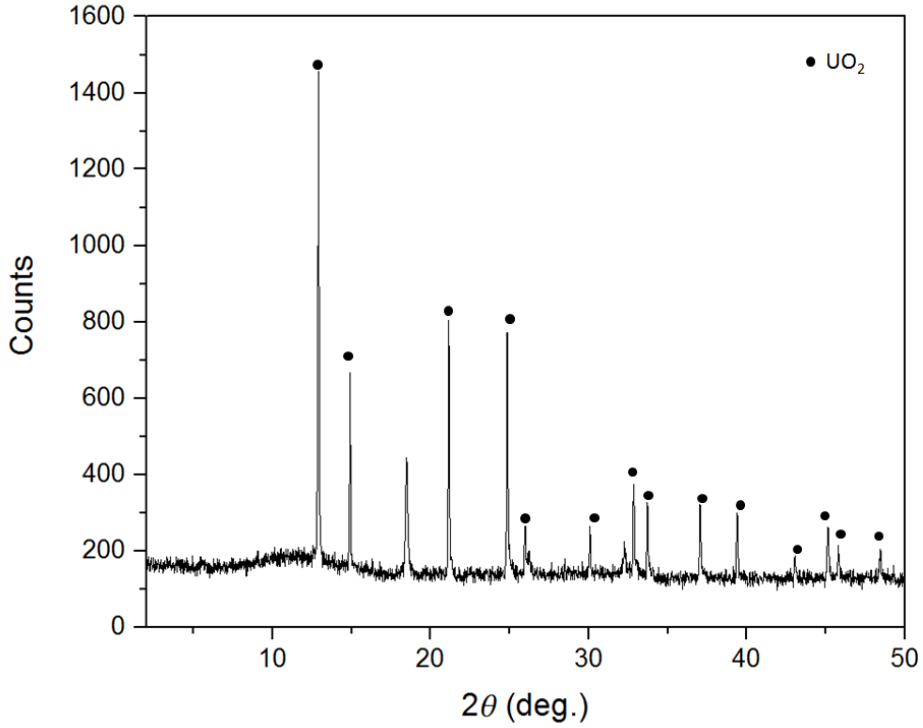

Figure 6.2 - X-ray diffraction spectrum (Mo Kα) of as-received UO_2 powder sample, showing UO_2 (35204-ICSD [180]).

6.2.3 Procedure

Experiments were carried out under a dry argon atmosphere at a melt temperature of 450 ˚C (unless indicated otherwise). Argon was bubbled into the melt, which resulted in a homogeneous distribution of particles as assessed by visual inspection. 4 cm (3.84 cm^2) of the current collector was immersed in the melt during the fluidised cathode measurements, and all the holes in the MCE, making sure that the

Mo wire and W rod stayed outside the melt. Absolute currents are reported due to the fact that the electrode surface area changes during experiments.

6.3 Results and discussion

A predominance diagram, Chapter 4, was constructed for the Li-K-U-O-Cl system, relating the potential *E* vs. standard chlorine electrode (S.Cl.E) to the negative logarithm of O^{2-} ion activity, pO^{2-}. All the thermodynamic data used for the production of the diagram is presented in Table 4.2, and the derived interface equations are presented in Appendix B. A predominance diagram for uranium species in LiCl-KCl has been published [181]; however, it did not consider all the stable species that can form, and the thermodynamic data has been revised and updated since.

The predominance diagram in Figure 4.9 shows the different regions of stability for different compounds and oxidation states of uranium. Thermodynamically, one can deduce that the concentration of O^{2-} ions in the eutectic melt greatly affects the reduction process of UO_2 to U metal. Starting with UO_2, two reduction reactions take place to produce U metal, according to the predominance diagram at 500 °C. These are presented in Equations 6.1 and 6.2. Equations 6.3 and 6.4 are used to calculate the potential, *E*, needed for each reaction to take place, at different values of O^{2-} ion activity.

$$UO_2 + 2e^- \leftrightarrow UO + O^{2-} \quad 6.1$$

$$UO + 2e^- \leftrightarrow U + O^{2-} \quad 6.2$$

$$E_{6.1} = \frac{-\Delta G^0_{6.1}}{2F} + \frac{RTln10}{2F} pO^{2-} \quad 6.3$$

$$E_{6.2} = \frac{-\Delta G^0_{6.2}}{2F} + \frac{RTln10}{2F} pO^{2-} \quad 6.4$$

The pO^{2-} ranges and potential bands (vs. S.Cl.E and Ag/Ag^+ references electrode) are presented in

Table 6.1, for the reactions described in Equations 6.1 and 6.2.

Table 6.1 - Thermodynamically calculated values of pO^{2-} and potentials required for Equations 6.1 and 6.2 to take place.

Reaction	pO^{2-}	E (V vs. S.Cl.E)	E (V vs. Ag/Ag^{+})
6.1	6.200 – 21.650	-3.558 – -2.374	-2.422 – -1.238
6.2	6.500 – 21.750	-3.562 – -2.394	-2.426 – -1.258

Cyclic voltammetry measurements were performed on an MCE molybdenum electrode packed with UO_2 powder; this is presented in Figure 6.3. It was scanned from 0 V to -2.5 V, and back to 0 V (vs. Ag/Ag^{+} reference electrode). The coupled redox potentials at 1, 2, 1' and 2' represent the reduction of a thin film of oxide on the MCE molybdenum strip and its reoxidation. The redox pair A and A' are attributed to the reduction of UO_2 to U metal, and its reoxidation to UO_x (as it was not confirmed what the oxidised species was via analysis), as shown in the overall reaction described in Equation 6.5. This is in line with previous results [182].

$$UO_2 + 4e^- \leftrightarrow U + 2O^{2-} \qquad 6.5$$

Figure 6.4 shows cyclic voltammograms conducted on an MCE molybdenum electrode packed with UO_2 powder. These were scanned from 0 V to -2.5 V and back to 0 V, at a variety of scan rates, as indicated in the diagram. Again, the redox couple A and A' are attributed to the reduction of UO_2 to U metal, and its reoxidation to UO_x, as described in Equation 6.5. The reduction potential appears to be very close to the salt's decomposition potential; hence, indicating a high O^{2-} ion activity. As expected, at higher scan rates the reaction peaks are more predominant.

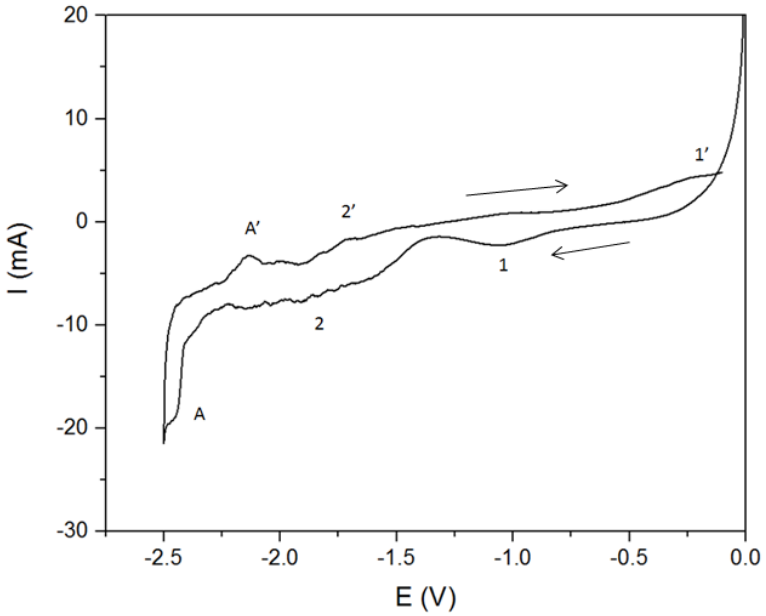

Figure 6.3 - Cyclic voltammogram of UO_2 in molybdenum metallic cavity electrode in LiCl-KCl eutectic at 450 ˚C, scan rate: 20 mV s^{-1}, reference electrode: Ag/Ag^+.

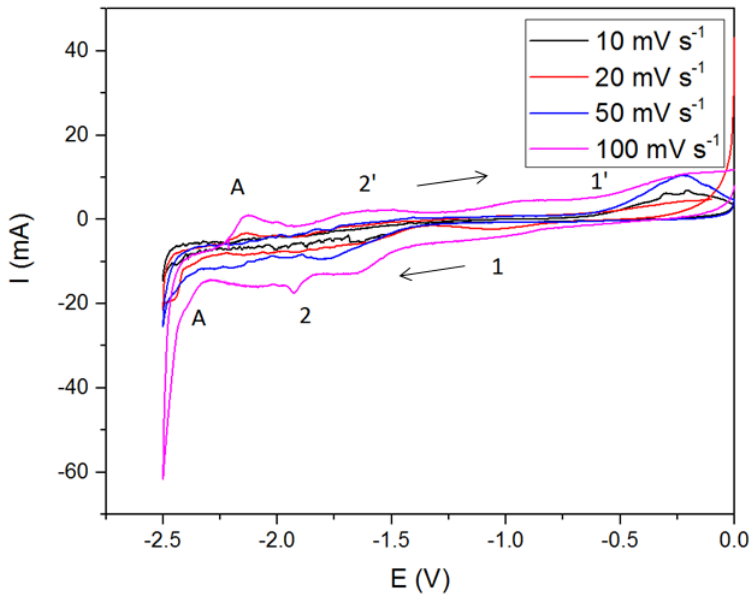

Figure 6.4 - Cyclic voltammograms of UO_2 in molybdenum metallic cavity electrode, at different scan rates, in LiCl-KCl eutectic at 450 ˚C, reference electrode: Ag/Ag^+ (A newly packed MCE was used for each scan).

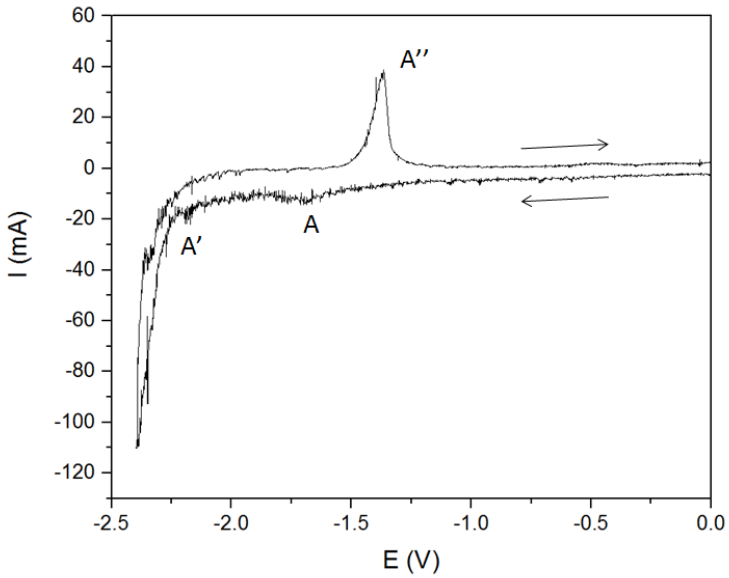

Figure 6.5 – Cyclic voltammetry of UO_2 fluidised cathode in LiCl-KCl eutectic at 450 °C, 5 g UO_2, argon flow rate: 600 cm^3 min^{-1}, reference electrode: Ag/Ag^+.

Voltammetry measurements were performed on a fluidised cathode set-up, Figure 6.5. It was scanned from 0 V to -2.4 V, and back to 0 V (vs. Ag/Ag^+ reference electrode). The combination of the peaks at A and A' represent the overall reduction of UO_2 to U metal as described by Equation 6.5. The peak at A'' represents the reoxidation of U to UO_x.

When comparing the voltammograms in Figure 6.5 (fluidised cathode) and Figure 6.3 (MCE), one can see that both peaks A and A' appear earlier in the negative direction, at ~ -1.7 V and ~ -2.2 V, in Figure 6.5, when compared to peak A in Figure 6.3, which appears at ~ -2.4 V. This is due to the dynamic nature of the fluidised cathode set-up. In the fluidise cathode process, a 3PI is immediately initiated at the collision point of an oxide particle with the current collector, and a reaction extends from this point. When using an MCE, the 3PI is defined at the circumference of the packed metal oxide, where it meets the metal strip current collector and the salt. This 3PI decreases as the reaction proceeds. Thus, in an MCE set-up more driving force is required than when using a fluidised cathode process, a higher overpotential. It is also likely that when using MCE's that the local O^{2-} ion concentration is higher.

Looking at the voltammogram in Figure 6.5 one can deduce that the reduction starts quite early on at ~ -1.7 V and then concludes at ~ -2.2 V. This suggests that using the fluidised cathode process both reactions, Equation 6.1 and 6.2, take place. Thus, the reduction follows two reactions with 2-electron transfer step processes, rather than the usual one 4-electron transfer step reaction (which could also be two reactions with 2-electron transfer step processes that take place rapidly after one another and thus appearing as one). Previous studies [183, 184] suggest that UO can exist in equilibrium in the presence of other uranium oxide states. Using the voltammetry information from Figure 6.3 and Figure 6.5, the reaction pathway for the reduction of UO_2 to U has been plotted on the predominance diagram in Figure 6.6, showing both the potential (vs. S.Cl.E) and the O^{2-} ion activity, as the reaction evolves. One can see that the activity of O^{2-} using the fluidised cathode process is generally lower. Also, it varies as the reaction proceeds, due to the fact that the reaction lasts for a longer time.

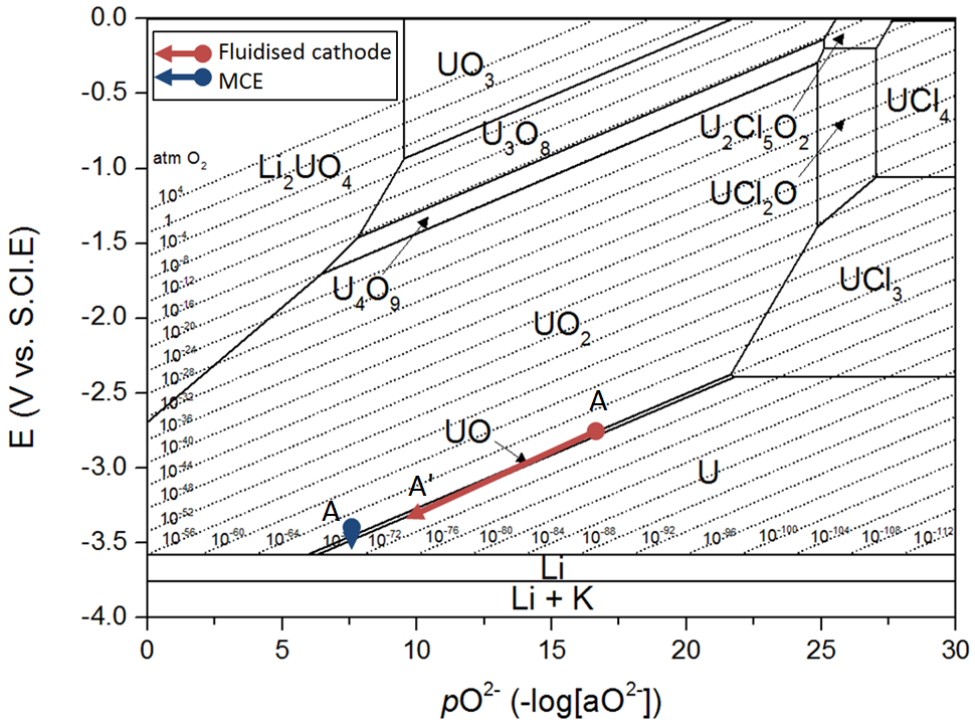

Figure 6.6 - Predominance diagram for the Li-K-U-O-Cl system at 500 °C, showing the reaction pathway for the reduction of UO_2 to U in LiCl-KCl using a fluidised cathode process and a metallic cavity electrode (MCE).

A constant potential of -2.2 V (vs. Ag/Ag^+ reference electrode), as identified as the reducing potential, was applied to the fluidised cathode system, Figure 6.7, 5 g of UO_2 powder was fluidised. As time passed, the current increased due to an increase in the electrode surface area and the deposit growth of U on the current collector surface. This growth is visible through the glass electrolytic cell set-up. At about 90,000 s, there is a rapid reduction in current associated with spalling off of the deposit from the electrode. New growth is then associated with the increase in the current, a similar characteristic of the process as seen for the reduction of WO_3 [70].

When comparing the chronoamperogram to that for the reduction of tungsten oxide, Figure 5.6, one can see that it takes a longer time for the electrode to start growing, observed as an increase in the current. It is possible that a 'seeding' effect whereby uranium metal takes some time to be deposited on the current collector. This is possibly due to the fact that the current collector is made from a different metal from that in the melt, compared with the all-tungsten system which did not have this induction period.

Due to the difference in densities, when the electrolyte is left to solidify, different layers of materials form, Figure 6.8 (c). Dark metallic uranium metal sinks to the bottom, followed by a layer of black, still to be reduced, uranium oxide, and finally a layer of LiCl-KCl eutectic (due to the similarity in appearance of U and UO_2, it was difficult to capture a clear edge between them). This could possibly provide a simple means of separation in a technological system, as is the case with tungsten. Figure 6.8 (a) shows an image of the current collector after the reduction has taken place, and Figure 6.8 (b) shows an image of the cross-section of the reduced U metal at the bottom of the reactor crucible.

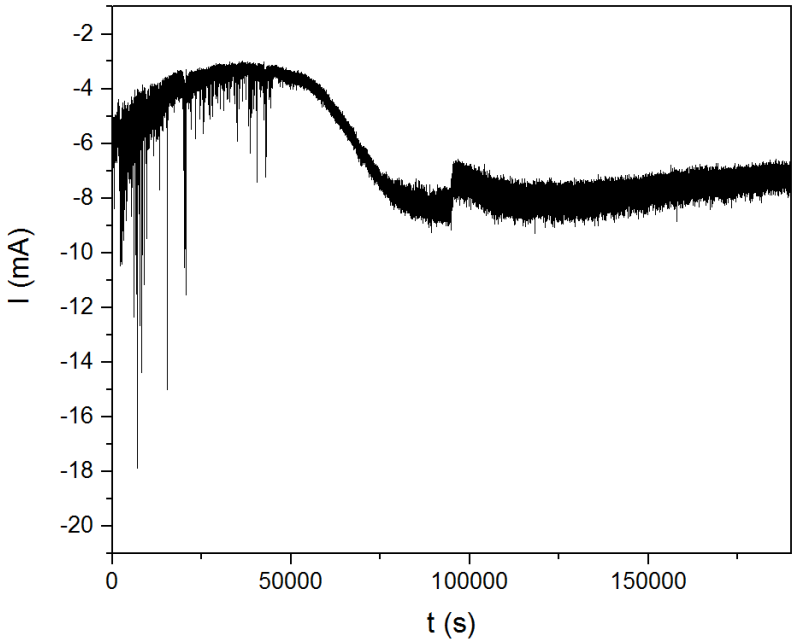

Figure 6.7 - Chronoamperogram of UO_2 fluidised cathode in LiCl-KCl eutectic at 450 °C, 5 g UO_2, argon flow rate: 600 cm^3 min^{-1}, set voltage: -2.2 V, reference electrode Ag/Ag^+.

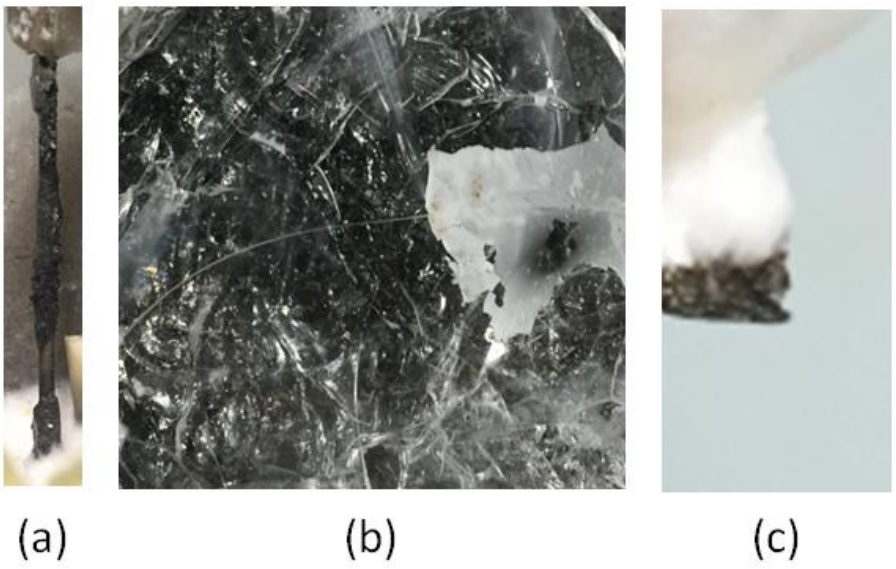

Figure 6.8 – (a) Photograph of reduced uranium deposited on tungsten working electrode, (b) photograph of the cross-section of the uranium product at the bottom of the crucible, (c) photograph of the solidified product, showing two separate layers of salt and uranium metal.

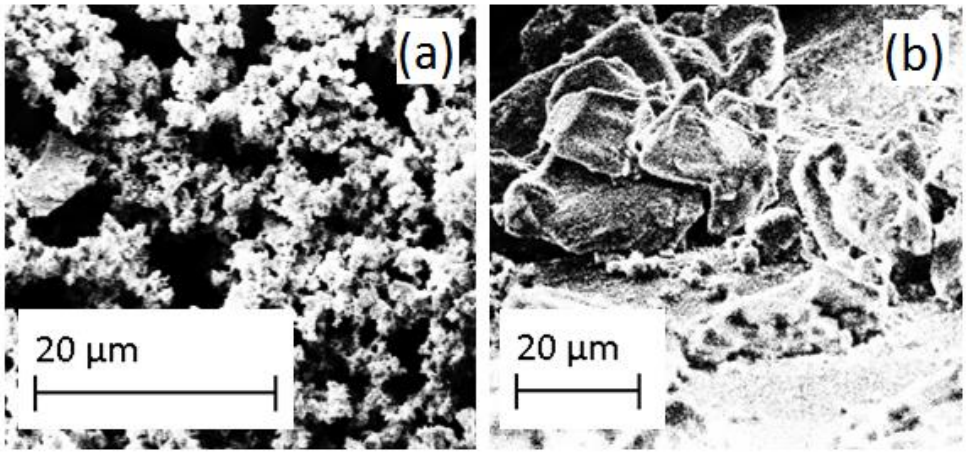

Figure 6.9 – SEM images of (a) the as-received UO_2 particles, and (b) product U obtained from the solidified melt as a separate layer to the LiCl-KCl.

There are two areas from where the final product could be collected, the bottom of the cell crucible and on the surface of the working electrode. Figure 6.9 (a) shows an SEM image of the as-received UO_2 particles and (b) an SEM image of the U metal product from the solidified melt. From the SEM images one can see that the UO_2 powder is very fine with particle sizes of ~1 µm, whereas the U product is in the form of agglomerated particles forming a larger particle size fused with some salt. Here, the use of vacuum distillation to separate the final product from the salt would be beneficial.

6.3.1 Current efficiency

To establish the current efficiency of the process, a constant potential of -2.2 V (vs. Ag/Ag^+ reference electrode) was applied to the fluidised cathode set-up to reduce 4 g of UO_2 to U metal, Figure 6.10. The chronoamperogram shows a similar trend to previously published work on electrochemical reduction of metal oxides [58], where the diagram can be segregated into two main stages; the first, where rapid reduction reactions occur and the current increases significantly. In the second stage, the current increases slightly again, then plateaus and slower reactions take place to reduce the final oxides, until the current decreases indicative of the batch reaction tending towards completion. Again, in Figure 6.10, one notices the

seeding time for the U particles to be deposited on the tungsten rod, as it takes time for the electrode to start growing and the current to increase subsequently.

Assuming 100% current efficiency, it would require a charge of 5717.59 C to be applied to fully reduce all 4 g of UO_2. The final product retrieved from the electrode's surface was analysed via XRD, Figure 6.11. The spectrum shows the spectra of KCl, and peaks associated with α-U. Most importantly, it shows that there is no sign of any uranium oxide species, namely UO_2 or UO. Thus, it confirms that complete conversion is possible via the fluidised cathode electrochemical process (in this case, unreacted oxide particles were presumably in the solidified melt). Calculating an accurate Faradaic efficiency is challenging due to various issues. To estimate the current efficiency, the curve toward the end of the chronoamperometry, Figure 6.10, was extended to reach zero current, estimating a constant gradient calculated from two points in the graph (7.52×10^5, -6.10×10^{-3} and 8.64×10^5, -5.60×10^{-3}). The x-intercept was found to be 2.375×10^6 s. The extended line was integrated to calculate the area, the hypothetical charge passed, which was found to be 4566.24 C. This was added to the actual charge passed, 1290 C, giving a total of 6230.10 C. The Faradaic efficiency of the process was calculated by dividing the theoretical charge by the charge passed (actual and hypothetical). Experiment concluded that the estimated current efficiency for reducing UO_2 to U in LiCl-KCl using the fluidised cathode process is ~ 92%. However, this is a very rough value, that would probably vary a lot.

When the final product was retrieved, a sample was placed in ethanol to dissolve the salt, under an argon atmosphere, to avoid any reoxidation via reaction with air or water, which was not desired for analysis. After leaving the sample in ethanol for 24 hr, the ethanol containing salt was filtered out using a small vacuum filtration unit. The sample (powder) was then placed in ethanol again, and the procedure was repeated twice. Finally, the product was dried in a vacuum oven at room temperature until dry. Despite this rigorous cleaning process, the XRD spectrum in Figure 6.11 confirms that some KCl is still present in the sample. A solution to this could be to employ vacuum distillation [172, 173] at high temperature to remove the salt whilst still molten. The nature of the fluidised cathode would complement such a filtration technique.

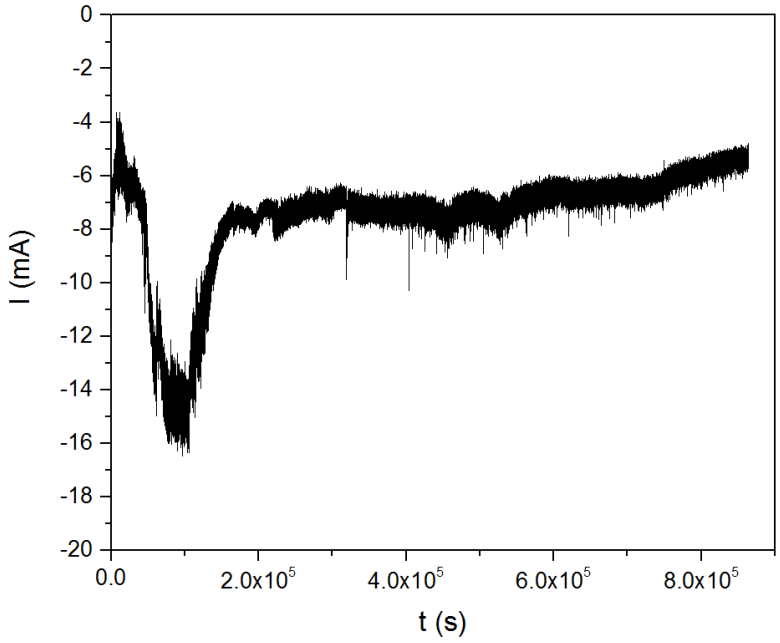

Figure 6.10 - Chronoamperogram of UO_2 fluidised cathode in LiCl-KCl eutectic at 450 ˚C, 4 g UO_2, argon flow rate: 600 cm^3 min^{-1}, reference electrode: Ag/Ag^+, set voltage: -2.2 V.

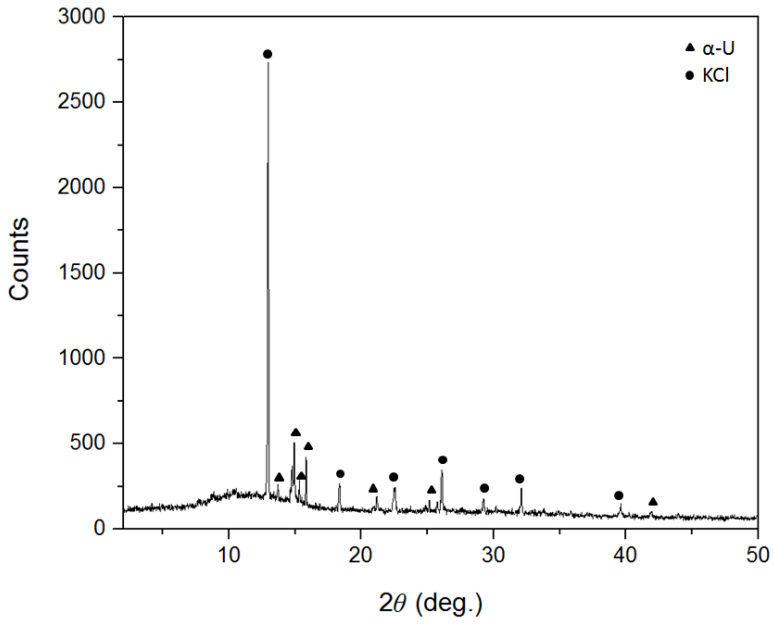

Figure 6.11 - X-ray diffraction spectrum (Mo Kα) of sample of product after complete reduction, showing peaks for α-U (43419-ICSD [185]), and KCl (165593-ICSD [127]).

6.4 Conclusions

The electrochemical reduction of UO_2 to U metal has been assessed, and it is likely to take place following two different reaction mechanisms; Equation 6.5, via a 4-electron transfer step reaction; and Equations 6.1 and 6.2, via two 2-electron step reactions. The route the reduction process follows depends on pO^{2-} and potential, which is highly influenced by the type of metal oxide precursor used, MCE packed electrode or a fluidised cathode.

The Faradaic current efficiency of the process has been estimated, via applying a constant potential of -2.2 V, as identified by voltammetry measurements, and found to be ~92%. The reduction process is split into three sections; the first where a seeding process takes place at a low potential to allow for the reduced uranium particles to be deposited onto the tungsten current collector; the second where rapid reduction of UO_2 particles occurs with a growth in electrode size accompanied by an increase in current being passed; the third where a slower reduction of the remaining oxides in the product occurs. The reduced product can be collected from two areas; the deposit of the current collector and the bottom of the reactor crucible.

The fluidised cathode is a robust, three-phase, high efficiency process. It has been studied here for the electrochemical reduction of UO_2; however, it might be applicable for other spent fuel oxides (such as UO_3 and PuO_2), and in the production of refractory metals, such as titanium. Further studies need to be undertaken to validate this.

7. Conclusions and Future Work

The aim of this research was to develop the understanding of spent nuclear materials behaviour in molten salts, via thermodynamic and electrochemical techniques, and to investigate electrochemical reduction processes from oxides to metals, which can prove to be significant in future generation IV nuclear power plants. New reactor designs are investigated as well, to improve the efficiency of such processes. The main findings and suggested future work are summarised in the Chapter.

7.1 Conclusions

7.1.1 Predominance Diagrams

Predominance phase diagrams for metal-molten salt systems are diagrams relating the potential to the negative logarithm of the O^{2-} ion activity (E-pO^{2-}). They are a useful tool for understanding the phase stability and electrochemistry of metal-oxide systems in molten salts. They assist in predicting reaction pathways and experimental results. They also give a good indication of whether a reaction is feasible in a molten salt system.

Diagrams were produced for the range of spent nuclear materials (based on the content of PWR MOX spent fuel). Thus, for U, Pu, Np, Am, Cm, Cs, Nd, Sm, Eu, Gd, Mo, Tc, Ru, Rh, Ag and Cd species. The diagrams were constructed for two salt systems; LiCl-KCl at 500 °C and NaCl-KCl at 750 °C. The two salt systems were chosen as they are the two main systems used for pyroprocessing research by ANL and RIAR, respectively. The temperatures were chosen within each salt's operating range.

All of the diagrams show regions of stability for the different metal species, their oxides and chlorides at unit activity; nonetheless, the activity can be changed in accordance to the equations that were derived.

The potential for selective direct reduction was also studied by superimposing the diagrams of U and Pu, and Am and Cm onto each other, for both salt systems at the two different temperatures. From the diagrams it was found that molten salt pyroprocessing provides a valuable route for the reprocessing of nuclear materials that is also resistant to proliferation, as it shows that it would be very challenging to separate Pu from U. However, the approach is not seen to be a replacement for the EXAm process, as the selective reduction and separation of Am from Cm would also be challenging due to the similarity in reduction potential. The effect of changing the operating temperature of the same salt system on the stability regions was also examined. At higher temperatures, the stability zones are shifted to the 'left', at higher O^{2-} ion activities; however, at higher temperatures, the potential window of the salt is smaller.

7.1.2 The electrochemical reduction of tungsten oxide

The electrochemical reduction of WO_3 to W metal has been assessed, and is likely to occur following the reaction mechanism $WO_3 \rightarrow WO_2 \rightarrow W$. A full reduction using the fluidised cathode process was achieved, with complete conversion of the product to W, as established via XRD analysis, by applying a constant potential of -2.14 V. The Faradaic efficiency of the process was found to be ~ 82%. The reduction process is split into two sections; the first where rapid reduction occurs, and the second where a slower reduction of the remaining tungsten oxide particles takes place. The product can be collected from the deposit on the current collector and the bottom of the reaction crucible, and is in the form of homogenously distributed particles.

Parameters, such as the fluidisation rate and the metal oxide – salt ratio, that affect the fluidised cathode process were investigated. Experiments concluded that increasing the fluidisation rate of the process results in an increase in the rate of deposit growth, as well as a greater collision-reaction noise. Whilst increasing the metal oxide – salt ratio results in increasing the rate at which the deposit growth (and hence, the current), but in decreasing the collision-reaction noise, and thus, decreasing the likelihood of product spall off. Therefore, the two main observations from investigating these two parameters are: a) the deposit growth, and the current

increase, are dependent on the frequency of particle – current collector collisions and reactions; b) the collision-reaction noise is dependent on the kinetic energy at which the particles collide with the current collector (spalling off of the product is highly related to this). Thus depending on the desired means of product recovery, e.g. a contentious flow retrieving or batch via the removal of electrodes, these conditions can be altered to suit.

Particle coulometric analyses has been carried out, which shed insight into the process in terms of total volume of particles impending on the current collector and being reduced at any given time. An electrochemical deposition model was also developed to estimate the porosity of the deposited product on the current collector, and the rate of its growth over time.

7.1.3 The electrochemical reduction of uranium oxide

The electrochemical reduction of UO_2 to U metal was studied, and it is likely to occur following two different reaction mechanisms; two 2-electron transfer reactions from $UO_2 \rightarrow UO \rightarrow U$, or one 4-electron reaction from $UO_2 \rightarrow U$. The pathway for the reactions depends highly on the pO^{2-} and the potential, which is greatly influenced by the type of uranium oxide precursor used; a fluidised cathode or a packed MCE. Using the fluidised cathode provides a much larger potential range at which the reduction reactions can occur.

The Faradaic efficiency of the reduction process using the fluidised cathode method was estimated, via applying a constant potential of -2.2 V and extrapolating the final decay to zero current, this was found to be ~ 92%. This process is inexact and requires refinement of our ability to measure the converted product with accuracy. An oxygen content analyser (LECO, St Joseph, MI, USA) would be very beneficial to get accurate readings.

The reduction process is split into three stages; the first, contrary to reducing WO_3 particles, involves an induction period, where low current is passed; this proposed to be due to a ‘seeding’ step where a U layer is formed on the tungsten current collector, onto which further reduction is more favourable. The second stage involves rapid reduction of UO_2 particles, as observed by the increase of current (and growth of deposit on the current collector). The third stage shows a slower

reduction of the remaining uranium oxide particles as the reactant oxide is exhausted. The reduced U product can, as is the case with tungsten, be collected from the deposit on the current collector and the bottom of reactor crucible.

The fluidised cathode process is a robust three-dimensional, high efficiency process. It also has other advantages, such as shortening the FFC process scheme, with associated cost reductions, and the flexibility of deciding whether to apply it for a contentious or a batch system. It has been studied for the electrochemical reduction of WO_3 and UO_2 to their pure metal forms; however, it is likely applicable for other spent oxide fuel materials (such as UO_3 and PuO_2), and in the production of other refractory metals, such as titanium and tantalum.

7.2 Future work

7.2.1 Three dimensional microstructural analyses

Three dimensional microstructural analyses [186-191] of the deposit on the current collector, using techniques such as X-ray computed tomography (X-ray CT) or FIB/SEM, would be very beneficial, as it would provide parameters, such as the porosity, for the electrochemical deposition model. This would be very useful for defining different parameters for experiments, especially if a batch process was to be employed, as this would help in defining the final electrode size with the product deposit to be retrieved.

7.2.2 Single particle reduction analyses

Studying how a single particle of metal oxide would reduce and attach to the current collector would be very interesting. Factors such as particle size and geometry could be changed and investigated. Using techniques such as non-destructive X-ray tomography and high speed filming, effects such as the change in particle morphology via the reduction reaction and the ‘necking’ of the particle to the current collector surface can be analysed.

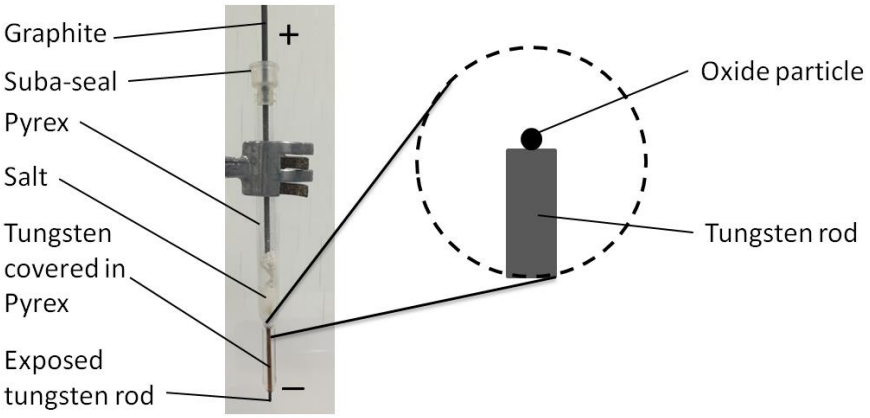

Figure 0.1 – Experimental set-up for single particle reduction studies.

An experimental set-up for single particles studies has been designed, and is presented in Figure 0.1. Here, a tungsten rod is covered in a Pyrex sheath, which then widens, only exposing the top of the electrode, into a narrow well, where the electrolyte and the particles to be reduced can be placed. The top of the well is sealed with a suba-seal through which a graphite anode is pushed and immersed into the fused salt. The exposed tungsten rod from the bottom and the graphite rod at the top are connected to potentiostat leads, so that electrochemical experiments can be carried out. The salt would be melted using an infrared laser, which based on lab trial experiments is sufficient to reach desired temperatures.

7.2.3 ABBIS process

The ABBIS (Abdulaziz, Brett, Brown, Inman, Shearing) process is described in the schematic shown in Figure 0.2. This is a concept that is an advancement of the fluidised cathode process that aims to simplify it and make it more robust. Here, the anode is a metal paste (potentially carbon or platinum) that is painted on the outside of a crucible made of a suitable ion conductor. The idea is that the oxide particles inside this crucible are reduced, whilst being agitated, and the O^{2-} ions created via the reduction process would migrate through the salt melt and the ion conductor and react with the anode on the outside, creating O_2.

This process would benefit from simpler reactor design, easier retrieval of final product, and possibly the reusability of the anode without degrading it. Foreseen challenges include the use of an appropriate oxide ion conductor (that operates at a relatively low temperature), molten salt electrolyte, temperature of process, pO^{2-} of the melt, and metal oxide to be reduced. Nonetheless, there is a large amount of literature to help in the design process, especially in choosing the right ion conductor and metal-oxide system for the desired parameters [192, 193].

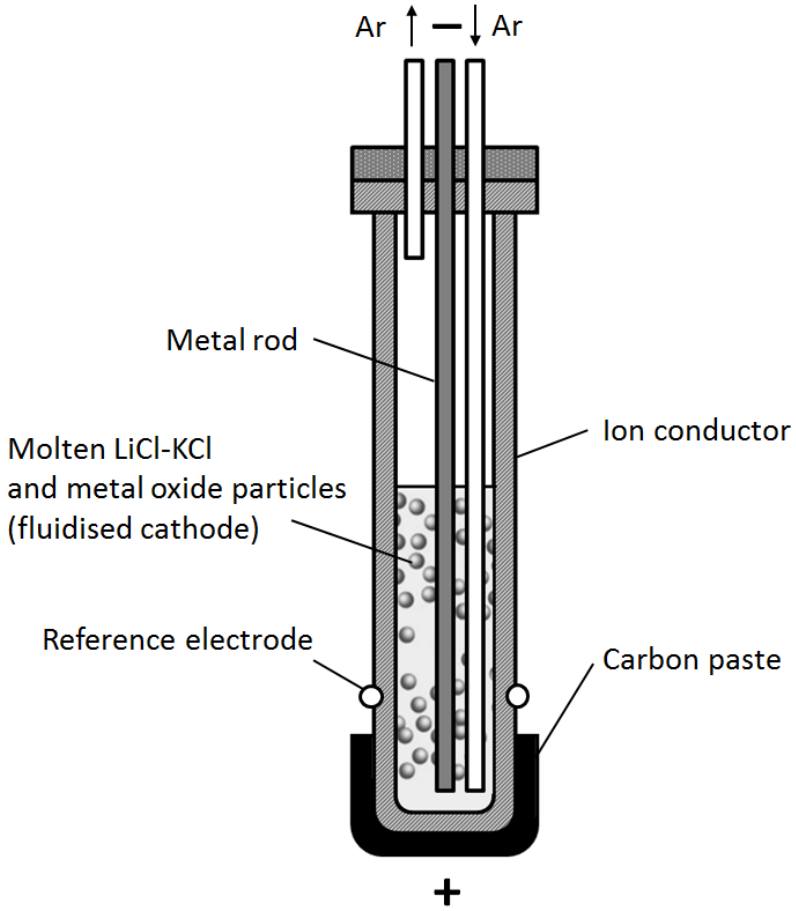

Figure 0.2 – Schematic for ABBIS process (with LiCl-KCl eutectic as an example).

7.2.4 Micro-electrode studies

It would be very beneficial to carry out studies on the fluidised cathode system using micro-electrodes for molten salts [194, 195]. Using different salts and metal oxides, these electrodes would be very beneficial in determining the types of reactions that occur; reversible, quasi or non-reversible, when reducing a metal oxide, as the reaction propagate downwards on a predominance diagram. This would also help indicating whether activities of certain species change, thus shifting equilibria, and ultimately result in making amendments to thermodynamic predictions.

7.2.5 TRISO fuel pyroprocessing

Tristructural-isotropic (TRISO) fuel, the schematic of which is presented in Figure 0.3, is a micro particle fuel designed to be used in Generation VI very-high-temperature reactors (VHTRs). It consists of an outer layer of pyrolytic carbon, followed by a layer of silicon carbide, followed by an inner layer of pyrolytic carbon, then a layer of porous carbon buffer that contains the fuel kernel, which is typically composed of UO_x, UC or UCO [196]. The TRISO particle is designed to withstand the most catastrophic accidents without releasing the fuel.

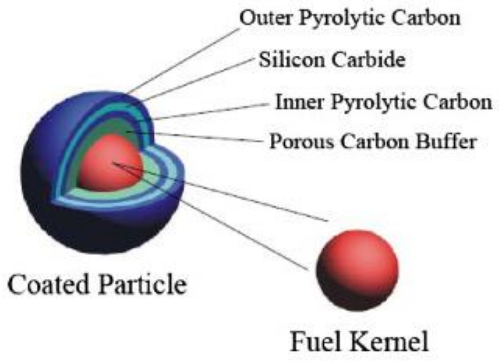

Figure 0.3 – Illustrative cutaway drawing of a TRISO fuel particle [196].

Numerous studies on the manufacturing and integrity of TRISO particles have been carried out; however, research in the processing of spent particles is deficient.

Previous studies of processing of TRISO particles were based on crushing the graphite fuel blocks and manually separating the fuel particles from the graphite. The outer carbon layer was then burned, followed by crushing of the silicon carbide layer. The inner carbon layers were then oxidised as well. The remaining ashes were then removed via leaching with nitric acid. The fuel was then removed from the solution via conventional solvent extraction techniques [197-199]. This technology involves many processing steps, and hence, it is costly. Some laboratory scale pyroprocessing methods have been developed employing electrorefining techniques [199]. The fluidised cathode process could prove very efficient in the pyroprocessing of spent TRISO particles, where the different layers could be stripped away at different potentials, ending with the fuel kernel particles, which could then be reduced to their pure metal form and extracted to be reused for metal fuelled Generation VI reactors.

7.2.6 Electrochemical reduction of UO_3, PuO_2 and mixed oxide fuels

Further studies on the reduction of spent nuclear materials can be carried out integrating the fluidised cathode in the reprocessing scheme. Studying the electrochemical reduction of UO_3 and PuO_2 is of particular interest, especially if an integrated reprocessing scheme is to be adopted (pyroprocessing with solvent extraction). With the help of predominance diagrams, the reaction pathways can be determined, and the process optimised. Employing the fluidised cathode for selective or full reduction of mixed actinides would be very interesting. Studying the separation process to follow would also be interesting; whether by mixing and settling in the reactor to see if different metals with different densities precipitate in separate layers, or are split after if a contentious process is employed. This could prove sufficient in the reprocessing cycle, eliminating steps such as centrifusion with associated cost reductions.

7.2.7 Electrochemical reduction of ThO_2

The use of thorium as a nuclear power fuel in new reactors has been suggested and studied for some time [200, 201]. Thorium is a promising alternative to conventional fuel types, as it contains a large amount of energy, is proliferation

resistant, and is more equally distributed worldwide. Bench scale experiments have been carried out for the recovery of thorium fuel using solvent extraction technology [202, 203]. One of the suggested Generation IV reactor designs is the thorium molten salt reactor [204-206]. Thus, a natural choice for the recovery of fuel from such a reactor would be by pyroprocessing. Here, the use of a fluidised cathode might prove useful, and hence, investigating the technique would be beneficial.

7.2.8 Electrochemical reduction of TiO_2

Employing the fluidised cathode process for the reduction of refractory metal oxides could prove beneficial, given its high Faradaic efficiency for the reduction of WO_3 and UO_2. One such refractory metal to apply the process to is titanium. The current efficiency for producing it via the FFC Cambridge process is quite low (10-40% [51]). Hence, it would be very interesting to produce titanium using the fluidised cathode process and comparing the efficiencies. Most of the studies on the electrochemical reduction of TiO_2 have been in $CaCl_2$. It would be also worth investigating the reduction in other molten salts such as LiCl-KCl eutectic, which benefits from a lower operating temperature.

Preliminary studies on the electrochemical reduction of TiO_2 to Ti metal in LiCl-KCl have been carried out. A predominance diagram, Chapter 4, was constructed for the Li-K-Ti-O-Cl system, Figure 0.4, relating the potential *E* vs. standard chlorine electrode (S.Cl.E) to the negative logarithm of O^{2-} ions activity, pO^{2-}. The derived interface equations are presented in Appendix D. A predominance diagram for titanium species in $CaCl_2$ has been published [131]; however, this is the first in LiCl-KCl eutectic. Cyclic voltammetry measurements on thermally grown thin TiO_2 films were conducted as well, Figure 0.5. These show clear reduction and reoxidation peaks (1, 2, 2’ and 1’, 3 and 3’ represent the reductive limit of the salt), thus suggesting that the direct electrochemical reduction of titanium oxide in LiCl-KCl is feasible. Further studies should be carried out to conclude the reduction pathway, and finally, to utilise the fluidised cathode process and asses its efficiency.

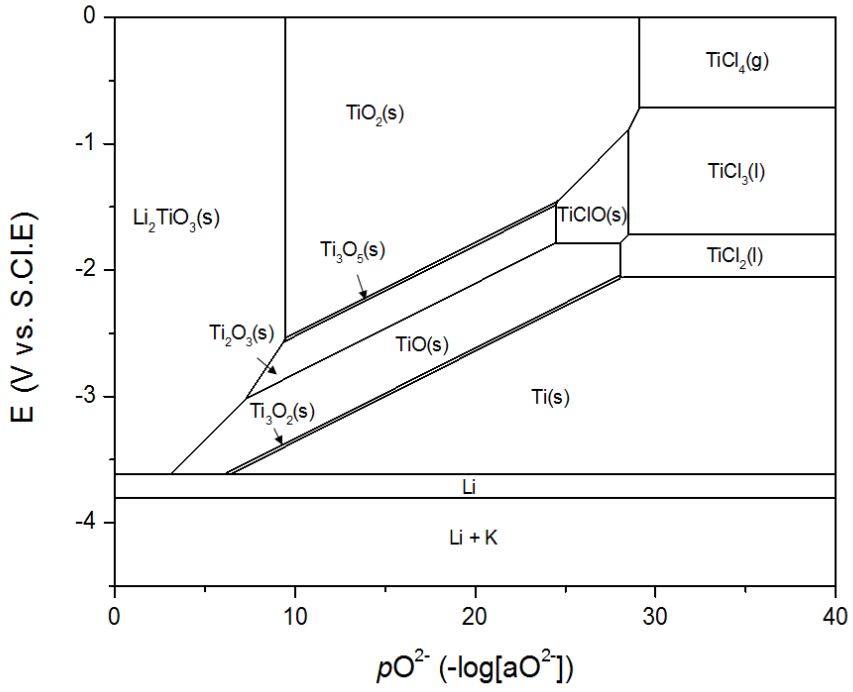

Figure 0.4 - Predominance diagram for the Li-K-Ti-O-Cl system at 500 °C.

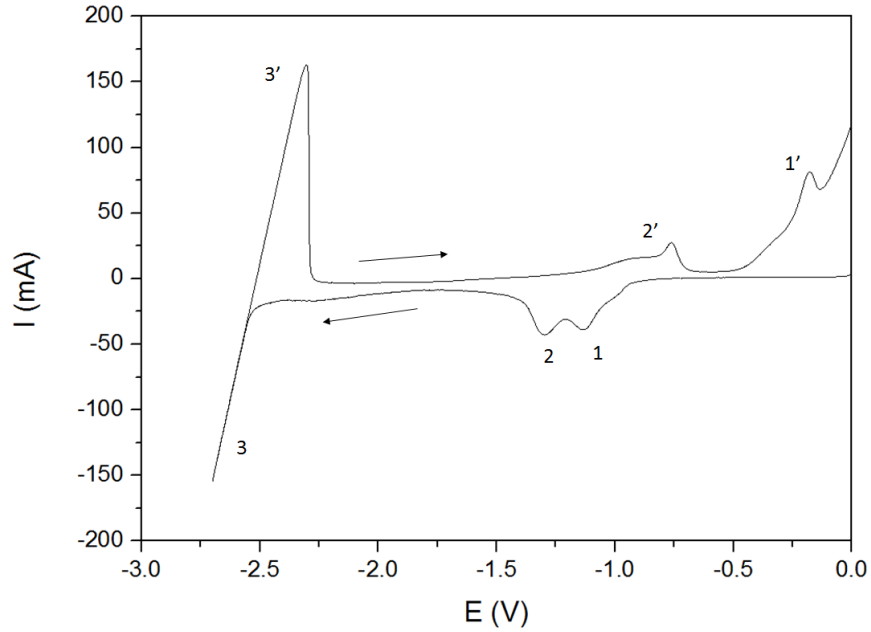

Figure 0.5 - Cyclic voltammogram of TiO_2 thin film cathode in LiCl-KCl eutectic at 450 °C, scan rate: 50 mV s^{-1}, reference electrode: Ag/Ag^+.

Dissemination

Peer-reviewd publications

Abdulaziz, R., Brown, L. D., Inman, D., Simons, S. J., Shearing, P. R., Brett, D. J. L. (2014). Effects of Process Conditions on the Fluidised Cathode Electrochemical Reduction of Tungsten Oxide in Molten LiCl-KCl Eutectic. *ECS Transactions*, 64(4), 323-331.

Abdulaziz, R., Brown, L. D., Inman, D., Simons, S., Shearing, P. R., Brett, D. J. L. (2014). A fluidised cathode process for the electrochemical reduction of tungsten oxide in a molten LiCl-KCl eutectic. *ECS Transactions*, 58 (19), 65-74.

Abdulaziz, R., Brown, L. D., Inman, D., Simons, S., Shearing, P. R., Brett, D. J. L. (2014). Novel fluidised cathode approach for the electrochemical reduction of tungsten oxide in molten LiCl-KCl eutectic. *Electrochemistry Communications*, 41(0), 44-46.

Brown, L. D., Abdulaziz, R., Jervis, R., Bharath, V., Attwood, R., Reinhard, C., Connor, L.D., Simons, S.J.R., Inman, D., Brett, D.J.L. Shearing, P. R. (2015). Following the electroreduction of uranium dioxide to uranium in LiCl-KCl eutectic in situ using synchrotron radiation. *Journal of Nuclear Materials*. 464, 256-262.

Brown, L. D., Abdulaziz, R., Simons, S., Inman, D., Brett, D. J. L., Shearing, P. R. (2013). Predominance diagrams of uranium and plutonum species in both lithium chloride_potassium chloride eutectic and calcium chloride. *Journal of Applied Electrochemistry*, 43(12), 1235-1241.

Conference presentations (oral)

Abdulaziz, R., Brown, L. D., Inman, D., Simons, S., Shearing, P. R., Brett, D. J. L. (2015). Effects of Process Conditions on the Fluidised Cathode Electrochemical Reduction of Tungsten Oxide in Molten LiCl-KCl Eutectic. *Molten Salts Discussion Group Summer Meeting, Cambridge.*

Abdulaziz, R., Brown, L. D., Inman, D., Simons, S., Shearing, P. R., Brett, D. J. L. (2014). Effects of Process Conditions on the Fluidised Cathode Electrochemical Reduction of Tungsten Oxide in Molten LiCl-KCl Eutectic. *ECS 226th Meeting, Cancun.*

Abdulaziz, R., Brown, L. D., Inman, D., Simons, S., Shearing, P. R., Brett, D. J. L. (2013). A fluidised Cathode Process for the Direct Electrochemical Reduction of Tungsten Oxide in Molten LiCl-KCl Eutectic. *Molten Salts Discussion Group Christmas Meeting, London.*

Abdulaziz, R., Brown, L. D., Inman, D., Simons, S., Shearing, P. R., Brett, D. J. L. (2013). Electrochemical Reduction of Tungsten Oxide in Molten LiCl-KCl Using a Novel Fluidised Bed Electrode Approach. *ECS 224th Meeting, San Francisco.*

Conference presentations (poster)

Abdulaziz, R., Brown, L. D., Inman, D., Simons, S., Shearing, P. R., Brett, D. J. L. (2014). Coulometric Analysis and the Effects of Fluidisation Rate on a Fluidised Cathode for the electrochemical Reduction of Tungsten Oxide in a Molten LiCl-KCl Eutectic. *ChemEngDayUK 2014, Manchester.*

Abdulaziz, R., Brown, L. D., Inman, D., Simons, S., Shearing, P. R., Brett, D. J. L. (2013). Predominance Diagrams for U and Pu in LiCl-KCl. *Electrochem 2013, Southhampton.*

Abdulaziz, R., Brown, L. D., Inman, D., Simons, S., Shearing, P. R., Brett, D. J. L. (2013). Predominance Diagrams for U and Pu in LiCl-KCl. *Molten Salts Discussion Group Summer Meeting, Cambridge.*

Appendices

Appendix A – calculations for immersion heater

To calculate the heat input needed to increase the temperature of the thermostatic salt bath Equations A.1 and A.2 are used.

$$Q = mc\Delta T + mL \quad \text{A.1}$$

$$Q = mc\Delta T \quad \text{A.2}$$

Where, Q is heat input in J;
m is mass of thermostatic salt used = 3000 g;
c is specific heat capacity of the salt = 1.592 J g^{-1} $^{\circ}C^{-1}$;
ΔT is change in temperature of the salt = T_f – T_s = desired temperature in ˚C - 20˚C (temperature of the salt at the start);
L is latent heat of the salt = 97 J g^{-1}.

Equation A.1 is used when the required final temperature of the molten salt mixture is higher than 220 °C, and Equation A.2 is used when the desired temperature is lower than 220 °C. Thus, Q is the heat output needed to be transferred from the nichrome wire of the immersion heater to the salt eutectic. The nichrome wire is 4 m long and 0.46 mm in diameter. Hence, its resistance is 26.63 Ω. To allow sufficient time for the wire and the salt bath to heat up, 1.5 hrs heating time is assigned. Hence:

$$P = \frac{Q}{60 \times 90 seconds} \quad \text{A.3}$$

Where, P is power in J s^{-1}.

Equation A.4, rearranged as A.5, is then used to calculate the voltage needed.

$$P = I^2 R = \left(\frac{V}{R}\right)^2 R \quad \text{A.4}$$

$$V = R\sqrt{\frac{P}{R}} \quad \text{A.5}$$

Where, I is current in A;

R is resistance in Ω.

Table 0.1, shows the calculated heat, power and voltage for a given final temperature of the thermostatic salt bath. Heat loss to the environment is not accounted for; however these values give a good indication for the range of voltage needed to be supplied through the variac.

Table 0.1 - Voltage, power and heat needed to reach specified temperatures of the thermostatic salt bath.

T (˚C)	Q (J)	P (J s^{-1})	V (V)
600	3061000	567	123
500	2583000	478	113
400	2106000	390	102
300	1628000	302	90
200	860000	159	65
100	382000	71	44

Appendix B – Electrode potential and pO^{2-} equations for predominance diagrams of spent nuclear materials

Uranium (U) species

$UO + 2e^- \leftrightarrow U + O^{2-}$	$E = \frac{-\Delta G^o}{2F} + \frac{RTln10}{2F} pO^{2-}$
$UO_2 + 2e^- \leftrightarrow UO + O^{2-}$	$E = \frac{-\Delta G^o}{2F} + \frac{RTln10}{2F} pO^{2-}$
$U_4O_9 + 2e^- \leftrightarrow 4UO_2 + O^{2-}$	$E = \frac{-\Delta G^o}{2F} + \frac{RTln10}{2F} pO^{2-}$
$4U_3O_8 + 10e^- \leftrightarrow 3U_4O_9 + 5O^{2-}$	$E = \frac{-\Delta G^o}{10F} + \frac{5RTln10}{10F} pO^{2-}$
$3UO_3 + 2e^- \leftrightarrow U_3O_8 + O^{2-}$	$E = \frac{-\Delta G^o}{2F} + \frac{RTln10}{2F} pO^{2-}$
$U_2Cl_5O_2 + e^- \leftrightarrow 2UCl_2O + Cl^-$	$E = \frac{-\Delta G^o}{F}$
$2UO_3 + 5Cl^- + 3e^- \leftrightarrow U_2Cl_5O_2 + 4O^{2-}$	$E = \frac{-\Delta G^o}{3F} + \frac{4RTln10}{3F} pO^{2-}$
$2U_3O_8 + 15Cl^- + 5e^- \leftrightarrow 3U_2Cl_5O_2 + 10O^{2-}$	$E = \frac{-\Delta G^o}{5F} + \frac{10RTln10}{5F} pO^{2-}$
$UO_2 + 2Cl^- \leftrightarrow UCl_2O + O^{2-}$	$pO^{2-} = \frac{\Delta G^o}{RTln10}$
$UO + 2Cl^- - 2e^- \leftrightarrow UCl_2O$	$E = \frac{\Delta G^o}{2F}$
$UCl_2O + 4e^- \leftrightarrow U + O^{2-} + 2Cl^-$	$E = \frac{-\Delta G^o}{4F} + \frac{RTln10}{4F} pO^{2-}$
$U^{3+} + 3e^- \leftrightarrow U$	$E = \frac{-\Delta G^o}{3F}$
$U^{4+} + e^- \leftrightarrow U^{3+}$	$E = \frac{-\Delta G^o}{F}$
$UO + 3Cl^- - e^- \leftrightarrow UCl_3 + O^{2-}$	$E = \frac{\Delta G^o}{F} - \frac{RTln10}{F} pO^{2-}$
$UO_2 + 3Cl^- + e^- \leftrightarrow UCl_3 + 2O^{2-}$	$E = \frac{-\Delta G^o}{F} + \frac{2RTln10}{F} pO^{2-}$
$UCl_2O + Cl^- + e^- \leftrightarrow UCl_3 + O^{2-}$	$E = \frac{-\Delta G^o}{F} + \frac{RTln10}{F} pO^{2-}$
$UCl_2O + 2Cl^- \leftrightarrow UCl_4 + O^{2-}$	$pO^{2-} = \frac{\Delta G^o}{RTln10}$
$U_2Cl_5O_2 + 3Cl^- + e^- \leftrightarrow 2UCl_4 + 2O^{2-}$	$E = \frac{-\Delta G^o}{F} + \frac{2RTln10}{F} pO^{2-}$
$U_4O_9 + 8Cl^- + 2e^- \leftrightarrow 4UCl_2O + 5O^{2-}$	$E = \frac{-\Delta G^o}{2F} + \frac{5RTln10}{2F} pO^{2-}$
$U_4O_9 + 10Cl^- \leftrightarrow 2U_2Cl_5O_2 + 5O^{2-}$	$pO^{2-} = \frac{\Delta G^o}{5RTln10}$

$Li_2UO_4 + 2e^- \leftrightarrow UO_2 + Li_2O + O^{2-}$ $E = \frac{-\Delta G^o}{2F} + \frac{2RTln10}{2F} pO^{2-}$

$4Li_2UO_4 + 6e^- \leftrightarrow U_4O_9 + 4Li_2O + 3O^{2-}$ $E = \frac{-\Delta G^o}{6F} + \frac{7RTln10}{6F} pO^{2-}$

$3Li_2UO_4 + 2e^- \leftrightarrow U_3O_8 + 3Li_2O + O^{2-}$ $E = \frac{-\Delta G^o}{2F} + \frac{4RTln10}{2F} pO^{2-}$

$Li_2UO_4 \leftrightarrow UO_3 + Li_2O$ $pO^{2-} = \frac{\Delta G^o}{RTln10}$

Plutonium (Pu) species

$Pu_2O_3 + 6e^- \leftrightarrow 2Pu + 3O^{2-}$ $E = \frac{-\Delta G^o}{6F} + \frac{3RTln10}{6F} pO^{2-}$

$2PuO_2 + 2e^- \leftrightarrow Pu_2O_3 + O^{2-}$ $E = \frac{-\Delta G^o}{2F} + \frac{RTln10}{2F} pO^{2-}$

$Pu^{3+} + 3e^- \leftrightarrow Pu$ $E = \frac{-\Delta G^o}{3F}$

$Pu_2O_3 + 2Cl^- \leftrightarrow 2PuClO + O^{2-}$ $pO^{2-} = \frac{\Delta G^o}{RTln10}$

$PuO_2 + Cl^- + e^- \leftrightarrow PuClO + O^{2-}$ $E = \frac{-\Delta G^o}{F} + \frac{RTln10}{F} pO^{2-}$

$PuClO + 2Cl^- \leftrightarrow PuCl_3 + O^{2-}$ $pO^{2-} = \frac{\Delta G^o}{RTln10}$

$PuClO + 3e^- \leftrightarrow Pu + Cl^- + O^{2-}$ $E = \frac{-\Delta G^o}{3F} + \frac{RTln10}{3F} pO^{2-}$

$PuO_2 + 3Cl^- + e^- \leftrightarrow PuCl_3 + 2O^{2-}$ $E = \frac{-\Delta G^o}{F} + \frac{2RTln10}{F} pO^{2-}$

Neptunium (Np) species

$Np + 2O^{2-} \leftrightarrow NpO_2 + 4e^-$ $E = \frac{-\Delta G^0}{4F} + \frac{2RTln10}{4F} pO^{2-}$

$2NpO_2 + O^{2-} \leftrightarrow Np_2O_5 + 2e^-$ $E = \frac{-\Delta G^0}{2F} + \frac{RTln10}{2F} pO^{2-}$

$NpO_2 + Li_2O + 3O^{2-} \leftrightarrow Li_2NpO_6 + 6e^-$ $E = \frac{-\Delta G^0}{6F} + \frac{4RTln10}{6F} pO^{2-}$

$Np_2O_5 + 2Li_2O + 5O^{2-} \leftrightarrow 2Li_2NpO_6 + 10e^-$ $E = \frac{-\Delta G^0}{10F} + \frac{7RTln10}{10F} pO^{2-}$

$Np \leftrightarrow Np^{3+} + 3e^-$ $E = \frac{-\Delta G^0}{3F}$

$Np^{3+} \leftrightarrow Np^{4+} + e^-$ $E = \frac{-\Delta G^0}{F}$

$NpCl_3 + 2O^{2-} \leftrightarrow NpO_2 + 3Cl^- + e^-$ $E = \frac{-\Delta G^0}{F} + \frac{2RTln10}{F} pO^{2-}$

$NpCl_4 + 2O^{2-} \leftrightarrow NpO_2 + 4Cl^-$ $\quad pO^{2-} = \frac{\Delta G^0}{2RTln10}$

Americium (Am) species

$2Am + 3O^{2-} \leftrightarrow Am_2O_3 + 6e^-$ $\quad E = \frac{-\Delta G^0}{6F} + \frac{3RTln10}{6F} pO^{2-}$

$Am_2O_3 + O^{2-} \leftrightarrow 2AmO_2 + 2e^-$ $\quad E = \frac{-\Delta G^0}{2F} + \frac{RTln10}{2F} pO^{2-}$

$Am \leftrightarrow Am^{3+} + 3e^-$ $\quad E = \frac{-\Delta G^0}{3F}$

$Am + O^{2-} + Cl^- \leftrightarrow AmClO + 3e^-$ $\quad E = \frac{-\Delta G^0}{3F} + \frac{RTln10}{3F} pO^{2-}$

$2AmClO + O^{2-} \leftrightarrow Am_2O_3 + 2Cl^-$ $\quad pO^{2-} = \frac{\Delta G^0}{RTln10}$

$AmClO + O^{2-} \leftrightarrow AmO_2 + Cl^- + e^-$ $\quad E = \frac{-\Delta G^0}{F} + \frac{RTln10}{F} pO^{2-}$

$AmCl_3 + O^{2-} \leftrightarrow AmClO + 2Cl^-$ $\quad pO^{2-} = \frac{\Delta G^0}{RTln10}$

Curium (Cm) species

$2Cm + 3O^{2-} \leftrightarrow Cm_2O_3 + 6e^-$ $\quad E = \frac{-\Delta G^0}{6F} + \frac{3RTln10}{6F} pO^{2-}$

$Cm_2O_3 + O^{2-} \leftrightarrow 2CmO_2 + 2e^-$ $\quad E = \frac{-\Delta G^0}{2F} + \frac{RTln10}{2F} pO^{2-}$

$Cm \leftrightarrow Cm^{3+} + 3e^-$ $\quad E = \frac{-\Delta G^0}{3F}$

$Cm + O^{2-} + Cl^- \leftrightarrow CmClO + 3e^-$ $\quad E = \frac{-\Delta G^0}{3F} + \frac{RTln10}{3F} pO^{2-}$

$2CmClO + O^{2-} \leftrightarrow Cm_2O_3 + 2Cl^-$ $\quad pO^{2-} = \frac{\Delta G^0}{RTln10}$

$CmClO + O^{2-} \leftrightarrow CmO_2 + Cl^- + e^-$ $\quad E = \frac{-\Delta G^0}{F} + \frac{RTln10}{F} pO^{2-}$

$CmCl_3 + O^{2-} \leftrightarrow CmClO + 2Cl^-$ $\quad pO^{2-} = \frac{\Delta G^0}{RTln10}$

Caesium (Cs) species

$2Cs + O^{2-} \leftrightarrow Cs_2O + 2e^-$ $\quad E = \frac{-\Delta G^0}{2F} + \frac{RTln10}{2F} pO^{2-}$

$Cs_2O + O^{2-} \leftrightarrow Cs_2O_2 + 2e^-$ $\quad E = \frac{-\Delta G^0}{2F} + \frac{RTln10}{2F} pO^{2-}$

$Cs_2O_2 + O^{2-} \leftrightarrow Cs_2O_3 + 2e^-$ $E = \frac{-\Delta G^0}{2F} + \frac{RTln10}{2F} pO^{2-}$

$Cs_2O_3 + O^{2-} \leftrightarrow CsO_2 + 2e^-$ $E = \frac{-\Delta G^0}{2F} + \frac{RTln10}{2F} pO^{2-}$

Neodymium (Nd) species

$2Nd + 3O^{2-} \leftrightarrow Nd_2O_3 + 6e^-$ $E = \frac{-\Delta G^0}{6F} + \frac{3RTln10}{6F} pO^{2-}$

$Nd_2O_3 + O^{2-} \leftrightarrow 2NdO_2 + 2e^-$ $E = \frac{-\Delta G^0}{2F} + \frac{RTln10}{2F} pO^{2-}$

$Nd + O^{2-} + Cl^- \leftrightarrow NdClO + 3e^-$ $E = \frac{-\Delta G^0}{3F} + \frac{RTln10}{3F} pO^{2-}$

$2NdClO + O^{2-} \leftrightarrow Nd_2O_3 + 2Cl^-$ $pO^{2-} = \frac{\Delta G^0}{RTln10}$

$NdCl_3 + O^{2-} \leftrightarrow NdClO + 2Cl^-$ $pO^{2-} = \frac{\Delta G^0}{RTln10}$

$Nd \leftrightarrow Nd^{3+} + 3e^-$ $E = \frac{-\Delta G^0}{3F}$

Samarium (Sm) species

$2Sm + 3O^{2-} \leftrightarrow Sm_2O_3 + 6e^-$ $E = \frac{-\Delta G^0}{6F} + \frac{3RTln10}{6F} pO^{2-}$

$Sm + O^{2-} + Cl^- \leftrightarrow SmClO + 3e^-$ $E = \frac{-\Delta G^0}{3F} + \frac{RTln10}{3F} pO^{2-}$

$2SmClO + O^{2-} \leftrightarrow Sm_2O_3 + 2Cl^-$ $pO^{2-} = \frac{\Delta G^0}{RTln10}$

$SmCl_3 + O^{2-} \leftrightarrow SmClO + 2Cl^-$ $pO^{2-} = \frac{\Delta G^0}{RTln10}$

$Sm \leftrightarrow Sm^{3+} + 3e^-$ $E = \frac{-\Delta G^0}{3F}$

Europium (Eu) species

$Eu + O^{2-} \leftrightarrow EuO + 2e^-$ $E = \frac{-\Delta G^0}{2F} + \frac{RTln10}{2F} pO^{2-}$

$2EuO + O^{2-} \leftrightarrow Eu_2O_3 + 2e^-$ $E = \frac{-\Delta G^0}{2F} + \frac{RTln10}{2F} pO^{2-}$

$Eu \leftrightarrow Eu^{3+} + 3e^-$ $E = \frac{-\Delta G^0}{3F}$

$EuO + Cl^- \leftrightarrow EuClO + e^-$ $E = \frac{-\Delta G^0}{F}$

$EuCl_3 + O^{2-} \leftrightarrow EuClO + 2Cl^-$ $pO^{2-} = \frac{\Delta G^0}{RTln10}$

$2EuClO + O^{2-} \leftrightarrow Eu_2O_3 + 2Cl^-$ $pO^{2-} = \frac{\Delta G^0}{RTln10}$

$EuCl_3 + O^{2-} \leftrightarrow EuO + 3Cl^- - e^-$ $E = \frac{\Delta G^0}{F} - \frac{RTln10}{F} pO^{2-}$

Gadolinium (Gd) species

$2Gd + 3O^{2-} \leftrightarrow Gd_2O_3 + 6e^-$ $E = \frac{-\Delta G^0}{6F} + \frac{3RTln10}{6F} pO^{2-}$

$Gd + O^{2-} + Cl^- \leftrightarrow GdClO + 3e^-$ $E = \frac{-\Delta G^0}{3F} + \frac{RTln10}{3F} pO^{2-}$

$2GdClO + O^{2-} \leftrightarrow Gd_2O_3 + 2Cl^-$ $pO^{2-} = \frac{\Delta G^0}{RTln10}$

$GdCl_3 + O^{2-} \leftrightarrow GdClO + 2Cl^-$ $pO^{2-} = \frac{\Delta G^0}{RTln10}$

$Gd \leftrightarrow Gd^{3+} + 3e^-$ $E = \frac{-\Delta G^0}{3F}$

Molybdenum (Mo) species

$Mo + 2O^{2-} \leftrightarrow MoO_2 + 4e^-$ $E = \frac{-\Delta G^0}{4F} + \frac{2RTln10}{4F} pO^{2-}$

$MoO_2 + O^{2-} \leftrightarrow MO_3 + 2e^-$ $E = \frac{-\Delta G^0}{2F} + \frac{RTln10}{2F} pO^{2-}$

$MoO_2 + Li_2O + O^{2-} \leftrightarrow Li_2MoO_4 + 2e^-$ $E = \frac{-\Delta G^0}{2F} + \frac{2RTln10}{2F} pO^{2-}$

$MoO_3 + Li_2O \leftrightarrow Li_2MoO_4$ $pO^{2-} = \frac{\Delta G^0}{RTln10}$

$Mo + Li_2O + 3O^{2-} \leftrightarrow Li_2MoO_4 + 6e^-$ $E = \frac{-\Delta G^0}{6F} + \frac{4RTln10}{6F} pO^{2-}$

$MoCl_2O + O^{2-} \leftrightarrow MoO_2 + 2Cl^-$ $pO^{2-} = \frac{\Delta G^0}{RTln10}$

$Mo \leftrightarrow Mo^{2+} + 2e^-$ $E = \frac{-\Delta G^0}{2F}$

$Mo^{2+} \leftrightarrow Mo^{5+} + 3e^-$ $E = \frac{-\Delta G^0}{3F}$

$MoCl_2 + 2O^{2-} \leftrightarrow MoO_2 + 2Cl^- + 2e^-$ $E = \frac{-\Delta G^0}{2F} + \frac{2RTln10}{2F} pO^{2-}$

$MoCl_5 + 2O^{2-} \leftrightarrow MoO_2 + 5Cl^- - e^-$ $E = \frac{\Delta G^0}{F} - \frac{2RTln10}{F} pO^{2-}$

$MoCl_2 + O^{2-} \leftrightarrow MoCl_2O + 2e^-$ $E = \frac{-\Delta G^0}{2F} + \frac{RTln10}{2F} pO^{2-}$

$MoCl_5 + O^{2-} \leftrightarrow MoCl_2O + 3Cl^- - e^-$ $E = \frac{\Delta G^0}{F} - \frac{RTln10}{F} pO^{2-}$

$MoCl_5 + 3O^{2-} \leftrightarrow MoO_3 + 5Cl^- + e^-$ $E = \frac{-\Delta G^0}{F} + \frac{3RTln10}{F} pO^{2-}$

Technetium (Tc) species

$Tc + 2O^{2-} \leftrightarrow TcO_2 + 4e^-$ $E = \frac{-\Delta G^0}{4F} + \frac{2RTln10}{4F} pO^{2-}$

$TcO_2 + O^{2-} \leftrightarrow TcO_3 + 2e^-$ $E = \frac{-\Delta G^0}{2F} + \frac{RTln10}{2F} pO^{2-}$

$2TcO_3 + O^{2-} \leftrightarrow Tc_2O_7 + 2e^-$ $E = \frac{-\Delta G^0}{2F} + \frac{RTln10}{2F} pO^{2-}$

$Tc \leftrightarrow Tc^{3+} + 3e^-$ $E = \frac{-\Delta G^0}{3F}$

$TcCl_3 + 2O^{2-} \leftrightarrow TcO_2 + 3Cl^- + e^-$ $E = \frac{-\Delta G^0}{F} + \frac{2RTln10}{F} pO^{2-}$

Ruthenium (Ru) species

$Ru + 2O^{2-} \leftrightarrow RuO_2 + 4e^-$ $E = \frac{-\Delta G^0}{4F} + \frac{2RTln10}{4F} pO^{2-}$

$RuO_2 + 2O^{2-} \leftrightarrow RuO_4 + 4e^-$ $E = \frac{-\Delta G^0}{4F} + \frac{2RTln10}{4F} pO^{2-}$

$Ru \leftrightarrow Ru^{3+} + 3e^-$ $E = \frac{-\Delta G^0}{3F}$

$RuCl_3 + 2O^{2-} \leftrightarrow RuO_2 + 3Cl^- + e^-$ $E = \frac{-\Delta G^0}{F} + \frac{2RTln10}{F} pO^{2-}$

Rhodium (Rh) species

$2Rh + O^{2-} \leftrightarrow Rh_2O + 2e^-$ $E = \frac{-\Delta G^0}{2F} + \frac{RTln10}{2F} pO^{2-}$

$Rh_2O + O^{2-} \leftrightarrow 2RhO + 2e^-$ $E = \frac{-\Delta G^0}{2F} + \frac{RTln10}{2F} pO^{2-}$

$Rh \leftrightarrow Rh^+ + e^-$ $E = \frac{-\Delta G^0}{F}$

$Rh^+ \leftrightarrow Rh^{2+} + e^-$ $E = \frac{-\Delta G^0}{F}$

$Rh^{2+} \leftrightarrow Rh^{3+} + e^-$ $E = \frac{-\Delta G^0}{F}$

$2RhCl + O^{2-} \leftrightarrow Rh_2O + 2Cl^-$ $pO^{2-} = \frac{\Delta G^0}{RTln10}$

$2RhCl_3 + O^{2-} \leftrightarrow Rh_2O + 6Cl^- - 4e^-$ $E = \frac{\Delta G^0}{4F} - \frac{RTln10}{4F} pO^{2-}$

$RhCl_3 + O^{2-} \leftrightarrow RhO + 3Cl^- - e^-$ $E = \frac{\Delta G^0}{F} - \frac{RTln10}{F} pO^{2-}$

Cadmium (Cd) species

$Cd + O^{2-} \leftrightarrow CdO + 2e^-$ $E = \frac{-\Delta G^0}{2F} + \frac{RTln10}{2F} pO^{2-}$

$Cd \leftrightarrow Cd^{2+} + 2e^-$ $E = \frac{-\Delta G^0}{2F}$

$CdCl_2 + O^{2-} \leftrightarrow CdO + 2Cl^-$ $pO^{2-} = \frac{\Delta G^0}{RTln10}$

Appendix C - Electrode potential and $p\mathrm{O}^{2-}$ equations for the Li-K-W-O-Cl system's predominance diagram

$WO_2 + 4e^- \leftrightarrow W + 2O^{2-}$	$E = \frac{-\Delta G^0}{4F} + \frac{2RTln10}{4F} pO^{2-}$
$WO_3 + 2e^- \leftrightarrow WO_2 + O^{2-}$	$E = \frac{-\Delta G^0}{2F} + \frac{RTln10}{2F} pO^{2-}$
$W^{2+} + 2e^- \leftrightarrow W$	$E = \frac{-\Delta G^0}{2F}$
$W^{4+} + 2e^- \leftrightarrow W^{2+}$	$E = \frac{-\Delta G^0}{2F}$
$WO_3 + 2Cl^- \leftrightarrow WO_2Cl_2 + O^{2-}$	$pO^{2-} = \frac{\Delta G^0}{RTln10}$
$WO_2 + 2Cl^- - 2e^- \leftrightarrow WO_2Cl_2$	$E = \frac{\Delta G^0}{2F}$
$WO_2Cl_2 + 6e^- \leftrightarrow W + 2O^{2-} + 2Cl^-$	$E = \frac{-\Delta G^0}{6F} + \frac{2RTln10}{6F} pO^{2-}$
$WO_2Cl_2 + 2Cl^- + 2e^- \leftrightarrow WCl_4 + 2O^{2-}$	$E = \frac{-\Delta G^0}{2F} + \frac{2RTln10}{2F} pO^{2-}$
$WO_2Cl_2 + 4e^- \leftrightarrow WCl_2 + 2O^{2-}$	$E = \frac{-\Delta G^0}{4F} + \frac{2RTln10}{4F} pO^{2-}$
$WO_2 + 2Cl^- + 2e^- \leftrightarrow WCl_2 + 2O^{2-}$	$E = \frac{-\Delta G^0}{2F} + \frac{2RTln10}{2F} pO^{2-}$

Appendix D - Electrode potential and pO^{2-} equations for the Li-K-Ti-O-Cl system's predominance diagram

$3Ti + 2O^{2-} \leftrightarrow Ti_3O_2 + 4e^-$	$E = \frac{-\Delta G^0}{4F} + \frac{RTln10}{2F} pO^{2-}$
$Ti_3O_2 + O^{2-} \leftrightarrow 3TiO + 2e^-$	$E = \frac{-\Delta G^0}{2F} + \frac{RTln10}{2F} pO^{2-}$
$2TiO + O^{2-} \leftrightarrow Ti_2O_3 + 2e^-$	$E = \frac{-\Delta G^0}{2F} + \frac{RTln10}{2F} pO^{2-}$
$3Ti_2O_3 + O^{2-} \leftrightarrow 2Ti_3O_5 + 2e^-$	$E = \frac{-\Delta G^0}{2F} + \frac{RTln10}{2F} pO^{2-}$
$Ti_3O_5 + O^{2-} \leftrightarrow 3TiO_2 + 2e^-$	$E = \frac{-\Delta G^0}{2F} + \frac{RTln10}{2F} pO^{2-}$
$Li_2TiO_3 \leftrightarrow TiO_2 + Li_2O$	$pO^{2-} = \frac{\Delta G^0}{RTln10}$
$3Li_2TiO_3 + 2e^- \leftrightarrow Ti_3O_5 + 3Li_2O + O^{2-}$	$E = \frac{-\Delta G^0}{2F} + \frac{4RTln10}{2F} pO^{2-}$
$2Li_2TiO_3 + 2e^- \leftrightarrow Ti_2O_3 + 2Li_2O + O^{2-}$	$E = \frac{-\Delta G^0}{2F} + \frac{3RTln10}{2F} pO^{2-}$
$Li_2TiO_3 + 2e^- \leftrightarrow TiO + Li_2O + O^{2-}$	$E = \frac{-\Delta G^0}{2F} + \frac{2RTln10}{2F} pO^{2-}$
$3Li_2TiO_3 + 6e^- \leftrightarrow Ti_3O_2 + 3Li_2O + 3O^{2-}$	$E = \frac{-\Delta G^0}{6F} + \frac{6RTln10}{6F} pO^{2-}$
$Li_2TiO_3 + 4e^- \leftrightarrow Ti + Li_2O + 2O^{2-}$	$E = \frac{-\Delta G^0}{4F} + \frac{3RTln10}{4F} pO^{2-}$
$TiO_2 + Cl^- + e^- \leftrightarrow TiClO + O^{2-}$	$E = \frac{-\Delta G^0}{F} + \frac{RTln10}{F} pO^{2-}$
$Ti_3O_5 + 3Cl^- + e^- \leftrightarrow 3TiClO + 2O^{2-}$	$E = \frac{-\Delta G^0}{F} + \frac{2RTln10}{F} pO^{2-}$
$Ti_2O_3 + 2Cl^- \leftrightarrow 2TiClO + O^{2-}$	$pO^{2-} = \frac{\Delta G^0}{RTln10}$
$TiClO + e^- \leftrightarrow TiO + Cl^-$	$E = \frac{-\Delta G^0}{F}$
$TiClO + 3Cl^- - e^- \leftrightarrow TiCl_4 + O^{2-}$	$E = \frac{\Delta G^0}{F} - \frac{RTln10}{F} pO^{2-}$
$TiClO + 2Cl^- \leftrightarrow TiCl_3 + O^{2-}$	$pO^{2-} = \frac{\Delta G^0}{RTln10}$
$TiClO + Cl^- + e^- \leftrightarrow TiCl_2 + O^{2-}$	$E = \frac{-\Delta G^0}{F} + \frac{RTln10}{F} pO^{2-}$
$TiO + 2Cl^- \leftrightarrow TiCl_2 + O^{2-}$	$pO^{2-} = \frac{\Delta G^0}{RTln10}$

$Ti_3O_2 + 6Cl^- - 2e^- \leftrightarrow 3TiCl_2 + 2O^{2-}$	$E = \frac{\Delta G^0}{2F} - \frac{2RTln10}{2F} pO^{2-}$
$Ti^{4+} + e^- \leftrightarrow Ti^{3+}$	$E = \frac{-\Delta G^0}{F}$
$Ti^{3+} + e^- \leftrightarrow Ti^{2+}$	$E = \frac{-\Delta G^0}{F}$
$Ti^{2+} + 2e^- \leftrightarrow Ti$	$E = \frac{-\Delta G^0}{2F}$
$TiO_2 + 4Cl^- \leftrightarrow TiCl_4 + 2O^{2-}$	$pO^{2-} = \frac{\Delta G^0}{2RTln10}$
$TiO_2 + 3Cl^- + e^- \leftrightarrow TiCl_3 + 2O^{2-}$	$E = \frac{-\Delta G^0}{F} + \frac{2RTln10}{F} pO^{2-}$

References

[1] IAEA, Nuclear Energy Development in the 21st Century: Global Scenarios and Regional Trends, IAEA Nuclear Energy Series, Vienna, 2010.

[2] IEA, OECD, Key World Energy Statistics, Paris, 2014.

[3] IAEA, Nuclear Safety and Security, IAEA Annual Report, Vienna, 2010.

[4] C. Poinssot, S. Bourg, N. Ouvrier, N. Combernoux, C. Rostaing, M. Vargas-Gonzalez, J. Bruno, Assessment of the Environmental Footprint of Nuclear Energy Systems. Comparison between Closed and Open Fuel Cycles, Energy, 69 (2014) 199-211.

[5] OECD, OECD Factbook: Economic, Environmental and Social Statistics, Paris, 2013.

[6] P.D. Wilson, The Nuclear Fuel Cycle: From Ore to Waste, Oxford University Press, 1996.

[7] M. Benedict, T.H. Pigford, H.W. Levi, Nuclear Chemical Engineering, 2 ed., McGraw-Hill, 1981.

[8] IAEA, PRIS Database, Vienna, 2015.

[9] G.F. Hewitt, J.G. Collier, Introduction to Nuclear Power, Taylor & Francis, 2000.

[10] E.R. Irish, W.H. Reas, The PUREX Process - a Solvent Extraction Reprocessing Method for Irradiated Uranium, Symposiua on the Reprocessing of Irradiated Fuels Held at Brussels, 20 (1957) 25.

[11] K.L. Nash, G.J. Lumetta, Advanced Separation Techniques for Nuclear Fuel Reprocessing and Radioactive Waste Treatment, Woodhead Publishing, 2011.

[12] IEA, OECD, Nuclear Energy Data, Paris, 2014.

[13] D. Magnusson, B. Christiansen, J.P. Glatz, R. Malmbeck, G. Modolo, D. Serrano-Purroy, C. Sorel, Demonstration of a TODGA Based Extraction Process for the Partitioning of Minor Actinides from a PUREX Raffinate, Solvent Extraction and Ion Exchange, 27 (2009) 26-35.

[14] J.J. Laidler, J.E. Battles, W.E. Miller, J.P. Ackerman, E.L. Carls, Development of Pyroprocessing Technology, Progress in Nuclear Energy, 31 (1997) 131-140.

[15] NEA, Pyrochemical Separations in Nuclear Applications, (2004).

[16] A.I. Bhatt, H. Kinoshita, A.L. Koster, I. May, C.A. Sharrad, V.A. Volkovich, O.D. Fox, C.J. Jones, B.G. Lewin, J.M. Charnock, Actinide, Lanthanide and Fission Product Speciation and Electrochemistry in High and Low Temperature Ionic Melts, Centre for Radiochemistry Research, Department of Chemistry, University of Manchester, Oxford Road, Manchester, M13 9PL (United Kingdom), 2004.

[17] Oak Ridge National Laboratory, Advanced Head-End Processing of Spent Fuel: A Progress Report, ANS Annual Meeting, (2005).

[18] A. Landsberg, C.L. Hoatson, F.E. Block, The Chlorination Kinetics of Zirconium Dioxide in the Presence of Carbon and Carbon Monoxide, Metallurgical Transactions, 3 (1972) 521-527.

[19] M. Iizuka, T. Koyama, N. Kondo, R. Fujita, H. Tanaka, Actinides Recovery from Molten Salt/Liquid Metal System by Electrochemical Methods, Journal of Nuclear Materials, 247 (1997) 183-190.

[20] T. Koyama, M. Iizuka, N. Kondo, R. Fujita, H. Tanaka, Electrodeposition of Uranium in Stirred Liquid Cadmium Cathode, Journal of Nuclear Materials, 247 (1997) 227-231.

[21] S.A. Kuznetsov, M. Gaune-Escard, Redox Electrochemistry and Formal Standard Redox Potentials of the Eu(III)/Eu(II) Redox Couple in an Equimolar Mixture of Molten NaCl-KCl, Electrochimica Acta, 46 (2001) 1101-1111.

[22] P. Masset, R.J.M. Konings, R. Malmbeck, J. Serp, J.-P. Glatz, Thermochemical Properties of Lanthanides (Ln = La, Nd) and Actinides (An = U, Np, Pu, Am) in the Molten LiCl–KCl Eutectic, Journal of Nuclear Materials, 344 (2005) 173-179.

[23] D. Lambertin, J. Lacquement, S. Sanchez, G.S. Picard, Americium Chemical Properties in Molten LiCl–KCl Eutectic at 743 K, Plasmas & Ions, 3 (2000) 65-72.

[24] D. Lambertin, J. Lacquement, S. Sanchez, G. Picard, Determination of the Solubility Product of Plutonium Sesquioxide in the NaCl+$CaCl_2$ Eutectic and Calculation of a Potential–pO^{2-} Diagram, Electrochemistry Communications, 4 (2002) 447-450.

[25] A.V. Bychkov, O.V. Skiba, S.K. Vavilov, M.V. Kormilitzyn, A.G. Osipenco, Overview of RIAR Activity on Pyroprocess Development and Application to Oxide Fuel and Plans in the Coming Decade, Pyrochemical Separations OECD Workshop Proceedings, (2000) 37-46.

[26] M. Gaune-Escard, Molten Salts: From Fundamentals to Applications, Kluwer Academic, 2002.

[27] D.R. Sadoway, New Opportunities for Metals Extraction and Waste Treatment by Electrochemical Processing in Molten Salts, Journal of Materials Research, 10 (1995) 487.

[28] D. Inman, S.H. White, The Production of Refractory Metals by the Electrolysis of Molten Salts; Design Factors and Limitations, Journal of Applied Electrochemistry, 8 (1978) 375.

[29] B. Mishra, D.L. Olson, Molten Salt Applications in Materials Processing, Journal of Physics and Chemistry of Solids, 66 (2005) 396.

[30] Y. Ito, T. Nohira, Non-conventional Electrolytes for Electrochemical Applications, Electrochimica Acta, 45 (2000) 2611.

[31] G.J. Janz, Molten Salts Handbook, Academic Press, 1967.

[32] D. Sadoway, The Electrochemical Processing of Refractory Metals, Journal of the Minerals, Metals and Materials Society, 43 (1991) 15-19.

[33] M. Galopin, J.S. Daniel, Molten Salts in Metal Treating: Present Uses and Future Trends, Electrodeposition and Surface Treatment, 3 (1975) 1-31.

[34] D.J. Fray, Emerging Molten Salt Technologies for Metals Production, Journal of the Minerals, Metals and Materials Society, 53 (2001) 27.

[35] B. Trémillon, Reactions in Solution: An Applied Analytical Approach, John Wiley & Sons, 1997.

[36] L. Brunet, J. Caillard, P. André, Thermodynamic Calculation of n-Component Eutectic Mixtures, International Journal of Modern Physics C, 15 (2004) 675-687.

[37] E. Van Artsdalen, I. Yaffe, Electrical Conductance and Density of Molten Salt Systems: KCl–LiCl, KCl–NaCl and KCl–KI, The Journal of Physical Chemistry, 59 (1955) 118-127.

[38] H. Ito, Y. Hasegawa, Densities of Eutectic Mixtures of Molten Alkali Chlorides below 673 K, Journal of Chemical & Engineering Data, 46 (2001) 1203-1205.

[39] G.Z. Chen, D.J. Fray, T.W. Farthing, Direct Electrochemical Reduction of Titanium Dioxide to Titanium in Molten Calcium Chloride, Nature, 407 (2000) 361-364.

[40] S.J. Oosthuizen, In Search of Low Cost Titanium: The Fray Farthing Chen (FFC) Cambridge Process, The Journal of the South African Institute of Mining and Metallurgy, 111 (2011) 1-6.

[41] W. Kroll, The Production of Ductile Titanium, Transactions of the Electrochemical Society, 78 (1940) 35.

[42] A.J. Fenn, G. Cooley, D.J. Fray, Exploiting the FFC Cambridge Process, Advanced Materials and Processes, 162 (2004) 51-53.

[43] Z. Chen, T.W. Farthing, D.J. Fray, Removal of Oxygen from Metal Oxides and Solid Solutions by Electrolysis in a Fused Salt, Google Patents, 1999.

[44] R.O. Suzuki, Direct Reduction Processes for Titanium Oxide in Molten Salt, Journal of the Minerals, Metals and Materials Society , 59 (2007) 68.

[45] R.O. Suzuki, S. Inoue, Calciothermic Reduction of Titanium Oxide in Molten $CaCl_2$, Metallurgical and Materials Transactions B, 34 (2003) 277.

[46] R. Suzuki, K. Ono, K. Teranuma, Calciothermic Reduction of Titanium Oxide and in-situ Electrolysis in Molten $CaCl_2$, Metallurgical and Materials Transactions B, 34 (2003) 287-295.

[47] C. Schwandt, D.J. Fray, Determination of the Kinetic Pathway in the Electrochemical Reduction of Titanium Dioxide in Molten Calcium Chloride, Electrochimica Acta, 51 (2005) 66-76.

[48] K. Dring, Electrochemical Reduction of Titanium Dioxide in Molten Calcium Chloride, Ph.D. Dissertation, Imperial College London, London, 2005.

[49] K. Dring, R. Dashwood, D. Inman, Voltammetry of Titanium Dioxide in Molten Calcium Chloride at 900 °C, Journal of the Electrochemical Society, 152 (2005) E104-E113.

[50] R. Bhagat, D. Dye, S.L. Raghunathan, R.J. Talling, D. Inman, B.K. Jackson, K.K. Rao, R.J. Dashwood, In-situ Synchrotron Diffraction of the Electrochemical Reduction Pathway of TiO_2, Acta Materialia, 58 (2010) 5057-5062.

[51] C. Schwandt, D.T.L. Alexander, D.J. Fray, The Electro-deoxidation of Porous Titanium Dioxide Precursors in Molten Calcium Chloride under Cathodic Potential Control, Electrochimica Acta, 54 (2009) 3819-3829.

[52] D.T.L. Alexander, C. Schwandt, D.J. Fray, The Electro-deoxidation of Dense Titanium Dioxide Precursors in Molten Calcium Chloride giving a New Reaction Pathway, Electrochimica Acta, 56 (2011) 3286-3295.

[53] D. Hu, W. Xiao, G. Chen, Near-net-shape Production of Hollow Titanium Alloy Components via Electrochemical Reduction of Metal Oxide Precursors in Molten Salts, Metallurgical and Materials Transactions B, 44 (2013) 272-282.

[54] M. Ma, D. Wang, W. Wang, X. Hu, X. Jin, G.Z. Chen, Extraction of Titanium from Different Titania Precursors by the FFC Cambridge Process, Journal of Alloys and Compounds, 420 (2006) 37.

[55] B. Jackson, M. Jackson, D. Dye, D. Inman, R. Dashwood, Production of NiTi via the FFC Cambridge Process, Journal of the Electrochemical Society, 155 (2008) E171-E177.

[56] B.K. Jackson, The production of NiTi via the Fray Farthing Chen Cambridge Process, Ph.D. Dissertation, Imperial College London, London, 2009.

[57] B. Jackson, D. Dye, D. Inman, R. Bhagat, R. Talling, S. Raghunathan, M. Jackson, R. Dashwood, Characterisation of the FFC Cambridge Process for NiTi Production using In-situ X-ray Synchrotron Diffraction, Journal of the Electrochemical Society, 157 (2010) E57-E63.

[58] R. Bhagat, M. Jackson, D. Inman, R. Dashwood, The Production of Ti–Mo Alloys from Mixed Oxide Precursors via the FFC Cambridge Process, Journal of the Electrochemical Society, 155 (2008) E63.

[59] R. Bhagat, M. Jackson, D. Inman, R. Dashwood, Production of Ti–W Alloys from Mixed Oxide Precursors via the FFC Cambridge Process, Journal of the Electrochemical Society, 156 (2009) E1.

[60] K.S. Mohandas, D.J. Fray, FFC Cambridge Process and Removal of Oxygen from Metal-Oxygen Systems by Molten Salt Electrolysis: An Overview, Transactions of the Indian Institute of Metals, 57 (2004) 579.

[61] G. Chen, E. Gordo, D. Fray, Direct Electrolytic Preparation of Chromium Powder, Metallurgical and Materials Transactions B, 35 (2004) 223-233.

[62] Y. Deng, Wang, W. Xiao, Jin, Hu, G.Z. Chen, Electrochemistry at Conductor/Insulator/Electrolyte Three-Phase Interlines: A Thin Layer Model, The Journal of Physical Chemistry B, 109 (2005) 14043-14051.

[63] P. Kar, J.W. Evans, A Model for the Electrochemical Reduction of Metal Oxides in Molten Salt Electrolytes, Electrochimica Acta, 54 (2008) 835-843.

[64] K. Jiang, X. Hu, M. Ma, D. Wang, G. Qiu, X. Jin, G.Z. Chen, "Perovskitization"-Assisted Electrochemical Reduction of Solid TiO_2 in Molten $CaCl_2$, Angewandte Chemie International Edition, 45 (2005) 428-432.

[65] G. Garcia-Belmonte, J. Garcia Belmonte, Bisquert, Impedance Analysis of Galvanostatically Synthesized Polypyrrole Films. Correlation of Ionic Diffusion and Capacitance Parameters with the Electrode Morphology, Electrochimica Acta, 47 (2002) 4263-4272.

[66] G. Garcia Belmonte, V. Garciabelmonte, J. Vikhrenko, J. Garciacanadas, Bisquert, Interpretation of Variations of Jump Diffusion Coefficient of Lithium Intercalated into Amorphous WO_3 Electrochromic Films, Solid State Ionics, 170 (2004) 123-127.

[67] E. Krasicka-Cydzik, Deoxidation of Titania Foams, ECS Transactions, 50 (2013) 39-44.

[68] M.A. Henderson, Mechanism for the Bulk-Assisted Reoxidation of Ion Sputtered TiO_2 Surfaces: Diffusion of Oxygen to the Surface or Titanium to the bulk?, Surface Science, 343 (1995) L1156-L1160.

[69] M.A. Henderson, A Surface Perspective on Self-Diffusion in Rutile TiO_2, Surface Science, 419 (1999) 174-187.

[70] R. Abdulaziz, L.D. Brown, D. Inman, S. Simons, P.R. Shearing, D.J.L. Brett, Novel Fluidised Cathode Approach for the Electrochemical Reduction of Tungsten Oxide in Molten LiCl–KCl Eutectic, Electrochemistry Communications, 41 (2014) 44-46.

[71] J.N. Hiddleston, A.F. Douglas, Fluidized Bed Electrodes - Fundamental Measurements and Implications, Nature, 218 (1968) 601-602.

[72] J.R. Backhurst, J.M. Coulson, F. Goodridge, R.E. Plimley, M. Fleischmann, A Preliminary Investigation of Fluidized Bed Electrodes, Journal of the Electrochemical Society, 116 (1969) 1600-1607.

[73] T. Berent, I. Fells, R. Mason, Fluidized Bed Fuel Cell Electrodes, Nature, 223 (1969) 1054-1055.

[74] T. Berent, R. Mason, I. Fells, Fluidised-Bed Fuel-Cell Electrodes, Journal of Applied Chemistry and Biotechnology, 21 (1971) 71-76.

[75] M. Fleischmann, J.W. Oldfield, L. Tennakoon, Fluidized Bed Electrodes Part IV. Electrodeposition of Copper in a Fluidized Bed of Copper-Coated Spheres, Journal of Applied Electrochemistry, 1 (1971) 103-112.

[76] L.J.J. Janssen, On Oxygen Reduction at a Fluidized Bed Electrode, Electrochimica Acta, 16 (1971) 151-155.

[77] A.J. Monhemius, P.L.N. Costa, Interactions of Variables in the Fluidised-Bed Electrowinning of Copper, Hydrometallurgy, 1 (1975) 183-203.

[78] D. Hutin, F. Coeuret, Experimental Study of Copper Deposition in a Fluidized Bed Electrode, Journal of Applied Electrochemistry, 7 (1977) 463-471.

[79] B.J. Sabacky, J.W. Evans, Electrodeposition of Metals in Fluidized Bed Electrodes: Part II . An Experimental Investigation of Copper Electrodeposition at High Current Density, Journal of the Electrochemical Society, 126 (1979) 1180-1187.

[80] F. Coeuret, The Fluidized Bed Electrode for the Continuous Recovery of Metals, Journal of Applied Electrochemistry, 10 (1980) 687-696.

[81] C. Oloman, A.P. Watkinson, Hydrogen Peroxide Production in Trickle-Bed Electrochemical Reactors, Journal of Applied Electrochemistry, 9 (1979) 117-123.

[82] Y. Xiong, H.T. Karlsson, An Experimental Investigation of Chemical Oxygen Demand Removal from the Wastewater Containing Oxalic Acid using Three-Phase Three-Dimensional Electrode Reactor, Advances in Environmental Research, 7 (2002) 139-145.

[83] S. Germain, F. Goodridge, Copper Deposition in a Fluidised Bed Cell, Electrochimica Acta, 21 (1976) 545-550.

[84] F. Goodridge, C.J.H. King, A.R. Wright, Performance Studies on a Bipolar Fluidised Bed Electrode, Electrochimica Acta, 22 (1977) 1087-1091.

[85] Y. Matsuno, A. Tsutsumi, K. Yoshida, Characteristics of Three-Dimensional Electrodes for a Molten Carbonate Fuel Cell Anode, International Journal of Hydrogen Energy, 20 (1995) 601-605.

[86] A.C. Lee, S. Li, R.E. Mitchell, T.M. Gür, Conversion of Solid Carbonaceous Fuels in a Fluidized Bed Fuel Cell, Electrochemical and Solid-State Letters, 11 (2008) B20-B23.

[87] S. Li, A.C. Lee, R.E. Mitchell, T.M. Gür, Direct Carbon Conversion in a Helium Fluidized Bed Fuel Cell, Solid State Ionics, 179 (2008) 1549-1552.

[88] J. Zhang, Z. Zhong, D. Shen, J. Xiao, Z. Fu, H. Zhang, J. Zhao, W. Li, M. Yang, Characteristics of a Fluidized Bed Electrode for a Direct Carbon Fuel Cell Anode, Journal of Power Sources, 196 (2011) 3054-3059.

[89] Y. Matsuno, K. Suzawa, A. Tsutsumi, K. Yoshida, Characteristics of Three-Phase Fluidized-Bed Electrodes for an Alkaline Fuel Cell Cathode, International Journal of Hydrogen Energy, 21 (1996) 195-199.

[90] Y. Matsuno, A. Tsutsumi, K. Yoshida, Improvement in Electrode Performance of Three-Phase Fluidized-Bed Electrodes for an Alkaline Fuel Cell Cathode, International Journal of Hydrogen Energy, 22 (1997) 615-620.

[91] J. Grimm, D. Bessarabov, R. Sanderson, Review of Electro-Assisted Methods for Water Purification, Desalination, 115 (1998) 285-294.

[92] L. Neužil, F. Procháska, V. Bejček, M. Mocek, Modelling a Two-Stage Countercurrent Fluidized Bed Reactor for Removing SO_2 from Gases by Active Soda, Computers & Chemical Engineering, 12 (1988) 205-208.

[93] F. Goodridge, C.J. Vance, Copper Deposition in a Pilot-Plant-Scale Fluidized Bed Cell, Electrochimica Acta, 24 (1979) 1237-1242.

[94] K. Jüttner, U. Galla, H. Schmieder, Electrochemical Approaches to Environmental Problems in the Process Industry, Electrochimica Acta, 45 (2000) 2575-2594.

[95] M. Fleischmann, F. Goodridge, J.R. Backhurst, 1194181, British Patent, 1970.

[96] W. Xiao, X. Xiao, H. Wang, H. Yin, X. Zhu, D. Mao, Wang, Verification and Implications of the Dissolution–Electrodeposition Process During the Electro-Reduction of Solid Silica in Molten $CaCl_2$, RSC Advances, 2 (2012) 7588.

[97] W. Xiao, X. Xiao, G. Jin, Chen, Up-Scalable and Controllable Electrolytic Production of Photo-Responsive Nanostructured Silicon, Journal of Materials Chemistry A: Materials for Energy and Sustainability, 1 (2013) 10243.

[98] A. Boika, S.N. Thorgaard, A.J. Bard, Monitoring the Electrophoretic Migration and Adsorption of Single Insulating Nanoparticles at Ultramicroelectrodes, The Journal of Physical Chemistry B, 117 (2012) 4371-4380.

[99] D. Inman, G.J. Hills, L. Young, J.O.M. Bockris, Some Thermodynamic Aspects of Molten Salts: Halides of Uranium, Zirconium, Thorium, and Cerium in Alkali Halide Eutectics*, Annals of the New York Academy of Sciences, 79 (1960) 803-829.

[100] S. Kuznetsov, H. Hayashi, K. Minato, M. Gaune-Escard, Electrochemical Transient Techniques for Determination of Uranium and Rare-Earth Metal Separation Coefficients in Molten Salts, Electrochimica Acta, 51 (2006) 2463-2470.

[101] J. Laidler, J. Battles, W. Miller, J. Ackerman, E. Carls, Development of Pyroprocessing Technology, Progress in Nuclear Energy, 31 (1997) 131-140.

[102] J. Willit, W. Miller, J. Battles, Electrorefining of Uranium and Plutonium - A Literature Review, Journal of Nuclear Materials, 195 (1992) 229-249.

[103] Z. Tomczuk, J.P. Ackerman, R.D. Wolson, W.E. Miller, Uranium Transport to Solid Electrodes in Pyrochemical Reprocessing of Nuclear Fuel, Journal of The Electrochemical Society, 139 (1992) 3523-3528.

[104] T. Koyama, M. Iizuka, Y. Shoji, R. Fujita, H. Tanaka, T. Kobayashi, M. Tokiwai, An Experimental Study of Molten Salt Electrorefining of Uranium Using Solid Iron Cathode and Liquid Cadmium Cathode for Development of Pyrometallurgical Reprocessing, Journal of Nuclear Science and Technology, 34 (1997) 384-393.

[105] Y. Sakamura, T. Hijikata, K. Kinoshita, T. Inoue, T.S. Storvick, C.L. Krueger, L.F. Grantham, S.P. Fusselman, D.L. Grimmett, J.J. Roy, Separation of Actinides from Rare Earth Elements by Electrorefining in LiC1-KC1 Eutectic Salt, Journal of Nuclear Science and Technology, 35 (1998) 49-59.

[106] J. Roy, L. Grantham, D. Grimmett, S. Fusselman, C. Krueger, T. Storvick, T. Inoue, Y. Sakamura, N. Takahashi, Thermodynamic Properties of U, Np, Pu, and Am in Molten LiCl-KCl Eutectic and Liquid Cadmium, Journal of the Electrochemical Society, 143 (1996) 2487-2492.

[107] J.A. Plambeck, Encyclopedia of Electrochemistry of the Elements: Fused Salt Systems, Dekker, 1976.

[108] J.E. Kelly, Generation IV International Forum: A decade of Progress Through International Cooperation, Progress in Nuclear Energy, 77 (2014) 240-246.

[109] S. Herrmann, S. Li, M. Simpson, S. Phongikaroon, Electrolytic Reduction of Spent Nuclear Oxide Fuel as Part of an Integral Process to Separate and Recover Actinides from Fission Products, Separation Science and Technology, 41 (2006) 1965-1983.

[110] E.-Y. Choi, J.-M. Hur, I.-K. Choi, S.G. Kwon, D.-S. Kang, S.S. Hong, H.-S. Shin, M.A. Yoo, S.M. Jeong, Electrochemical Reduction of Porous 17 kg Uranium

Oxide Pellets by Selection of an Optimal Cathode/Anode Surface Area Ratio, Journal of Nuclear Materials, 418 (2011) 87-92.

[111] C.S. Seo, S.B. Park, B.H. Park, K.J. Jung, S.W. Park, S.H. Kim, Electrochemical Study on the Reduction Mechanism of Uranium Oxide in a LiCl-Li_2O Molten Salt, Journal of Nuclear Science and Technology, 43 (2006) 587-595.

[112] S.M. Jeong, S.B. Park, S.S. Hong, C.S. Seo, S.W. Park, Electrolytic Production of Metallic Uranium from U_3O_8 in a 20 kg Batch Scale Reactor, Journal of Radioanalytical and Nuclear Chemistry, 268 (2006) 349-356.

[113] Y. Sakamura, M. Kurata, T. Inoue, Electrochemical Reduction of UO_2 in Molten $CaCl_2$ or LiCl, Journal of The Electrochemical Society, 153 (2006) D31-D39.

[114] J.-M. Hur, S.-S. Hong, H. Lee, Electrochemical Reduction of UO_2 to U in a LiCl–KCl-Li_2O Molten Salt, Journal of Radioanalytical and Nuclear Chemistry, 295 (2013) 851-854.

[115] D. Inman, J.O.M. Bockris, The Application of the Galvanostatic Potential-Time Technique to Analysis in Molten Salts, Journal of Electroanalytical Chemistry (1959), 3 (1962) 126-145.

[116] A. Baraka, A.I. Abdel-Rohman, A.A.E. Hosary, Corrosion of Mild Steel in Molten Sodium Nitrate-Potassium Nitrate Eutectic, British Corrosion Journal, 11 (1976) 44-46.

[117] R.W. Bradshaw, N.P. Siegel, Molten Nitrate Salt Development for Thermal Energy Storage in Parabolic Trough Solar Power Systems, Proceedings of Energy Sustainability, (2008) 10-14.

[118] K. Coscia, S. Neti, A. Oztekin, S. Nelle, S. Mohapatra, T. Elliott, The Thermophysical Properties of the $NaNO_3$-KNO_3, $LiNO_3$-$NaNO_3$, and $LiNO_3$-KNO_3 Systems, Proceedings of the ASME 2011 International Mechanical Engineering Congress and Exposition, Denveer, Colorado, (2011).

[119] D.A. Nissen, Thermophysical Properties of the Equimolar Mixture Sodium Nitrate-Potassium Nitrate from 300 to 600 °C, Journal of Chemical & Engineering Data, 27 (1982) 269-273.

[120] D.J. Rogers, G.J. Janz, Melting-Crystallization and Premelting Properties of Sodium Nitrate-Potassium Nitrate. Enthalpies and heat capacities, Journal of Chemical & Engineering Data, 27 (1982) 424-428.

[121] J.O.M. Bockris, G.J. Hills, D. Inman, L. Young, An All-Glass Reference Electrode for Molten Salt Systems, Journal of Scientific Instruments (1950), 33 (1956) 438-439.

[122] G. Qiu, M. Ma, D. Wang, X. Jin, X. Hu, G.Z. Chen, Metallic Cavity Electrodes for Investigation of Powders Electrochemical Reduction of NiO and Cr_2O_3 Powders in Molten $CaCl_2$, Journal of the Electrochemical Society, 152 (2005) E328-E336.

[123] G. Qiu, X. Feng, M. Liu, W. Tan, F. Liu, Investigation on Electrochemical Reduction Process of Nb_2O_5 Powder in Molten $CaCl_2$ with Metallic Cavity Electrode, Electrochimica Acta, 53 (2008) 4074-4081.

[124] J. Peng, Y. Deng, D. Wang, X. Jin, G.Z. Chen, Cyclic Voltammetry of Electroactive and Insulative Compounds in Solid State: A Revisit of AgCl in Aqueous Solutions Assisted by Metallic Cavity Electrode and Chemically Modified Electrode, Journal of Electroanalytical Chemistry, 627 (2009) 28-40.

[125] J. Peng, G. Li, H. Chen, D. Wang, X. Jin, G.Z. Chen, Cyclic Voltammetry of ZrO_2 Powder in the Metallic Cavity Electrode in Molten $CaCl_2$, Journal of the Electrochemical Society, 157 (2010) F1-F9.

[126] G. Qiu, D. Wang, X. Jin, G.Z. Chen, A Direct Electrochemical Route from Oxide Precursors to the Terbium–Nickel Intermetallic Compound $TbNi_5$, Electrochimica Acta, 51 (2006) 5785-5793.

[127] V.N. Baumer, S.S. Galkin, L.V. Glushkova, T.P. Rebrova, Z.V. Shtitelman, Solubility of Al_2O_3 in Some Chloride−Fluoride Melts, Inorganic Chemistry, 45 (2006) 7367-7371.

[128] A. Levin'sh, M. Straumanis, K. Karlsons, Praezisionsbestimmung von Gitterkonstanten Hygroskopischer Verbindungen (LiCl, NaBr), Zeitschrift für Physikalische Chemie. Abteilung B Chemie der Elementarprozesse, Aufbau der Materie, 40 (1938) 146-150.

[129] R. Littlewood, Diagrammatic Representation of the Thermodynamics of Metal-Fused Chloride Systems, Journal of the Electrochemical Society, 109 (1962) 525.

[130] M. Pourbaix, Thermodynamics of Dilute Aqueous Solutions, E. Arnold, London, 1949.

[131] K. Dring, R. Dashwood, D. Inman, Predominance Diagrams for Electrochemical Reduction of Titanium Oxides in Molten $CaCl_2$, Journal of the Electrochemical Society, 152 (2005) D184.

[132] L.D. Brown, R. Abdulaziz, S. Simons, D. Inman, D.J.L. Brett, P.R. Shearing, Predominance Diagrams of Uranium and Plutonium Species in Both Lithium Chloride–Potassium Chloride Eutectic and Calcium Chloride, Journal of Applied Electrochemistry, 43 (2013) 1235-1241.

[133] D. Inman, N.S. Wrench, Corrosion in Fused Salts, British Corrosion Journal, 1 (1966) 246.

[134] A. Conte, M.D. Ingram, Corrosion of Silver in Fused Nitrates: Applications of E/pO^{2-} Diagrams, Electrochimica Acta, 13 (1968) 1551.

[135] G. Picard, F. Seon, B. Trémillon, Reactions of Formation and Stability of Iron (II) and (III) Oxides in LiCl-KCl Eutectic Melt at 470 °C, Journal of the Electrochemical Society, 129 (1982) 1450.

[136] T.H. Okabe, Y. Waseda, Producing Titanium Through an Electronically Mediated Reaction, Journal of the Minerals, Metals and Materials Society, 49 (1997) 28.

[137] A.M. Martínez, Y. Castrillejo, E. Barrado, G.M. Haarberg, G. Picard, A Chemical and Electrochemical Study of Titanium Ions in the Molten Equimolar $CaCl_2$ + NaCl Mixture at 550 °C, Journal of Electroanalytical Chemistry, 449 (1998) 67.

[138] T. Abiko, I. Park, T.H. Okabe, Reduction of Titanium Oxide in Molten Salt Medium, Ti-2003 10th World Conference on Titanium, Hamburg, 2003, 253.

[139] C. Caravaca, A. Laplace, J. Vermeulen, J. Lacquement, Determination of the E-pO^{2-} Stability Diagram of Plutonium in the Molten LiCl–KCl Eutectic at 450 °C, Journal of Nuclear Materials, 377 (2008) 340.

[140] X.Y. Yan, D.J. Fray, Direct Electrolytic Reduction of Solid Alumina Using Molten Calcium Chloride-Alkali Chloride Electrolytes, Journal of Applied Electrochemistry, 39 (2009) 1349.

[141] S. Wang, Y. Li, Reaction Mechanism of Direct Electro-Reduction of Titanium Dioxide in Molten Calcium Chloride, Journal of Electroanalytical Chemistry, 571 (2004) 37-42.

[142] NEA, Spent Nuclear Fuel Assay Data for Isotopic Validation State-of-the-Art Report, (2011).

[143] G. Radulescu, D.E. Mueller, J.C. Wagner, Sensitivity and Uncertainty Analysis of Commercial Reactor Criticals for Burnup Credit, U.S. Nuclear Regulatory Commision, (2008).

[144] V. Smolenski, A. Smolenski, J. Laplace, Lacquement, A Potentiometric Study of the Interaction of Zr(IV) and O(II) Ions in the LiCl-KCl Eutectic Molten Salt, Journal of the Electrochemical Society, 151 (2004) E302.

[145] I. Barin, Thermodynamical Data of Pure Substances, VCH Verlags Gesellschaft, Weinheim, 1993.

[146] M.W. Chase, JANAF thermochemical tables, American Institute of Physics, New York, 1985.

[147] Landolt-Bornstein, Thermodynamic Properties of Inorganic Materials, Springer-Verlag, Berlin-Heidelberg, 1999.

[148] V. Glushko, Thermocenter of the Russian Academy of Sciences, IVTAN Association, Izhorskaya, 13 (1994) 127412.

[149] Landolt-Bornstein, Thermodynamic Properties of Inorganic Materials, Springer-Verlag, Berlin-Heidelberg, 2001.

[150] I. Barin, Thermodynamical Data of Pure Substances, VCH Verlags Gesellschaft, Weinheim, 1989.

[151] O. Knacke, O. Kubaschewski, K. Hesselmann, Thermodynamic Properties of Inorganic Substances, Springer Verlag, Düsseldorf, Germany, (1991) 1.

[152] M. Binnewies, E. Milke, Thermochemical data of elements and compounds, Wiley-VCH, 2002.

[153] D.G. Archera, Thermodynamic Properties of the KCl+ H_2O System, Journal of Physical and Chemical Reference Data, 28 (1999).

[154] I. Barin, Thermodynamical Data of Pure Substances, VCH Verlags Gesellschaft, Weinheim, 1995.

[155] NEA, R. Guillaumont, F.J. Mompean, Update on the Chemical Thermodynamics of Uranium, Neptunium, Plutonium, Americium and Technetium., Elsevier, 2003.

[156] L.P. Ruzinov, B.S. Gulyanitskii, Equilibrium Transformations of Metallurgical Reactions, Moscow, 1975.

[157] I. Barin, Thermodynamical Data of Pure Substances, VCH Verlags Gesellschaft, Weinheim, 1977.

[158] Landolt-Bornstein, Thermodynamic Properties of Inorganic Materials, Springer-Verlag, Berlin-Heidelberg, 2000.

[159] A.J. Bard, R. Parsons, J. Jordan, Standard Potentials in Aqueous Solution, Taylor & Francis, 1985.

[160] M.K. Karapet'iants, M.L. Karapet'iants, Thermodynamic constants of inorganic and organic compounds, Humphrey Science Publishers, 1970.

[161] J.R. Haas, E.L. Shock, D.C. Sassani, Rare Earth Elements in Hydrothermal Systems: Estimates of Standard Partial Molal Thermodynamic Properties of Aqueous Complexes of the Rare Earth Elements at High Pressures and Temperatures, Geochimica et Cosmochimica Acta, 59 (1995) 4329-4350.

[162] L.B. Pankratz, M. United States. Bureau of, Thermodynamic Properties of Carbides, Nitrides, and Other Selected Substances, U.S. Department of the Interior, U.S. Bureau of Mines, Washington, D.C.

[163] M.W. Chase, NIST-JANAF thermochemical tables, New York, 1998.

[164] C. Rostaing, C. Poinssot, D. Warin, P. Baron, B. Lorraina, Development and Validation of the EXAm Separation Process for Single Am Recycling, Procedia Chemistry, 7 (2012) 367-373.

[165] E. Lassner, W. D. Schubert, Tungsten: Properties, Chemistry, Technology of the Element, Alloys, and Chemical Compounds, Springer Science & Business Media, 2012.

[166] E. Lassner, From Tungsten Concentrates and Scrap to Highly Pure Ammonium Paratungstate (APT), The Chemistry of Non-Sag Tungsten, Pergamon, Oxford, 1995, 35-44.

[167] V. Malyshev, A. Gab, A. M. Popescu, V. Constantin, Electroreduction of Tungsten Oxide(VI) in Molten Salts with Added Metaphosphate, Chemical Research in Chinese Universities, 29 (2013) 771-775.

[168] X. Xi, G. Si, Z. Nie, L. Ma, Electrochemical Behavior of Tungsten Ions from WC Scrap Dissolution in a Chloride Melt, Electrochimica Acta, 184 (2015) 233-238.

[169] G. Si, X. Xi, Z. Nie, L. Zhang, L. Ma, Preparation and Characterization of Tungsten Nanopowders from WC Scrap in Molten Salts, International Journal of Refractory Metals and Hard Materials, 54 (2016) 422-426.

[170] K. Dring, R. Dring, M. Bhagat, R. Jackson, D. Dashwood, Inman, Direct Electrochemical Production of Ti–10W Alloys from Mixed Oxide Preform Precursors, Journal of Alloys and Compounds, 419 (2006) 103-109.

[171] R. Diehl, G. Brandt, E. Salje, The Crystal Structure of Triclinic WO_3, Acta Crystallographica Section B: Structural Crystallography and Crystal Chemistry, 34 (1978) 1105-1111.

[172] M. Rosenthal, P. Kasten, R. Briggs, Molten-Salt Reactors—History, Status, and Potential, Nuclear Technology, 8 (1970) 107-117.

[173] M.J. Earle, J.M. Esperança, M.A. Gilea, J.N.C. Lopes, L.P. Rebelo, J.W. Magee, K.R. Seddon, J.A. Widegren, The Distillation and Volatility of Ionic Liquids, Nature, 439 (2006) 831-834.

[174] H. Hartmann, F. Ebert, O. Bretschneider, Elektrolysen in Phosphatschmelzen. I. Die Elektrolytische Gewinnung von α-und β-Wolfram, Zeitschrift für Anorganische und Allgemeine Chemie, 198 (1931) 116-140.

[175] N. Rees, Y.G. Rees, R. Zhou, Compton, The Aggregation of Silver Nanoparticles in Aqueous Solution Investigated via Anodic Particle Coulometry, ChemPhysChem, 12 (2011) 1645-1647.

[176] E.J.E. Stuart, N.V. Rees, R.G. Compton, Particle-Impact Voltammetry: The Reduction of Hydrogen Peroxide at Silver Nanoparticles Impacting a Carbon Electrode, Chemical Physics Letters, 531 (2012) 94-97.

[177] N. Rees, Y.G. Rees, R. Zhou, Compton, Making Contact: Charge Transfer during Particle–Electrode Collisions, RSC Advances, 2 (2012) 379.

[178] K. Tschulik, B. Haddou, D. Omanović, N. Rees, R. Compton, Coulometric Sizing of Nanoparticles: Cathodic and Anodic Impact Experiments Open Two

Independent Routes to Electrochemical Sizing of Fe_3O_4 Nanoparticles, Nano Research, 6 (2013) 836-841.

[179] M. Williamson, J. Willit, Pyroprocessing Flowsheets for Recycling Used Nuclear Fuel, Nuclear Engineering and Technology, 43 (2011) 329-334.

[180] S. Barrett, A. Jacobson, B. Tofield, B. Fender, The Preparation and Structure of Barium Uranium Oxide $BaUO_{3+x}$, Acta Crystallographica Section B: Structural Crystallography and Crystal Chemistry, 38 (1982) 2775-2781.

[181] I. Uchida, J. Niikura, S. Toshima, Electrochemical Study of UO_2^{2+}-UO_2^{+}-UO_2 System in Molten LiCl+KCl Eutectic, Journal of Electroanalytical Chemistry and Interfacial Electrochemistry, 124 (1981) 165-177.

[182] L. Brown, R. Abdulaziz, R. Jervis, V. Bharath, R. Attwood, C. Reinhard, L. Connor, S. Simons, D. Inman, D. Brett, Following the Electroreduction of Uranium Dioxide to Uranium in LiCl–KCl Eutectic In Situ using Synchrotron Radiation, Journal of Nuclear Materials, 464 (2015) 256-262.

[183] S. Abramowitz, N. Acquista, K.R. Thompson, Infrared Spectrum of Matrix-Isolated Uranium Monoxide, The Journal of Physical Chemistry, 75 (1971) 2283-2285.

[184] M.C. Heaven, J.P. Nicolai, S.J. Riley, E.K. Parks, Rotationally Resolved Electronic Spectra for Uranium Monoxide, Chemical Physics Letters, 119 (1985) 229-233.

[185] M.H. Mueller, R.L. Hitterman, H.W. Knott, The Atomic Position Parameter in Alpha Uranium–Room Temperature and Above, Acta Crystallographica, 15 (1962) 421-422.

[186] P.R. Shearing, J. Golbert, R.J. Chater, N.P. Brandon, 3D Reconstruction of SOFC Anodes using a Focused Ion Beam Lift-Out Technique, Chemical Engineering Science, 64 (2009) 3928-3933.

[187] P.R. Shearing, R.S. Bradley, J. Gelb, S.N. Lee, A. Atkinson, P.J. Withers, N.P. Brandon, Using Synchrotron X-Ray Nano-CT to Characterize SOFC Electrode Microstructures in Three-Dimensions at Operating Temperature, Electrochemical and Solid-State Letters, 14 (2011) B117-B120.

[188] P. Shearing, R. Bradley, J. Gelb, F. Tariq, P. Withers, N. Brandon, Exploring Microstructural Changes Associated with Oxidation in Ni–YSZ SOFC Electrodes using High Resolution X-ray Computed Tomography, Solid State Ionics, 216 (2012) 69-72.

[189] R. Clague, P. Shearing, P. Lee, Z. Zhang, D. Brett, A. Marquis, N. Brandon, Stress Analysis of Solid Oxide Fuel Cell Anode Microstructure Reconstructed from Focused Ion Beam Tomography, Journal of Power Sources, 196 (2011) 9018-9021.

[190] P. Trogadas, O.O. Taiwo, B. Tjaden, T.P. Neville, S. Yun, J. Parrondo, V. Ramani, M.O. Coppens, D.J. Brett, P.R. Shearing, X-ray Micro-Tomography as a Diagnostic Tool for the Electrode Degradation in Vanadium Redox Flow Batteries, Electrochemistry Communications, 48 (2014) 155-159.

[191] D.S. Eastwood, P.M. Bayley, H.J. Chang, O.O. Taiwo, J. Vila-Comamala, D.J. Brett, C. Rau, P.J. Withers, P.R. Shearing, C.P. Grey, Three-Dimensional Characterization of Electrodeposited Lithium Microstructures using Synchrotron X-ray Phase Contrast Imaging, Chemical Communications, 51 (2015) 266-268.

[192] D.J.L. Brett, A. Atkinson, N.P. Brandon, S.J. Skinner, Intermediate Temperature Solid Oxide Fuel Cells, Chemical Society Reviews, 37 (2008) 1568-1578.

[193] W. Maskell, B. Steele, Solid State Potentiometric Oxygen Gas Sensors, Journal of Applied Electrochemistry, 16 (1986) 475-489.

[194] D.K. Corrigan, E.O. Blair, J.G. Terry, A.J. Walton, A.R. Mount, Enhanced Electroanalysis in Lithium Potassium Eutectic (LKE) Using Microfabricated Square Microelectrodes, Analytical Chemistry, 86 (2014) 11342-11348.

[195] E.O. Blair, D.K. Corrigan, J.G. Terry, A.R. Mount, A.J. Walton, Development and Optimization of Durable Microelectrodes for Quantitative Electroanalysis in Molten Salt, Journal of Microelectromechanical Systems, 24 (2015) 1346-1354.

[196] J.J. Powers, B.D. Wirth, A Review of TRISO Fuel Performance Models, Journal of Nuclear Materials, 405 (2010) 74-82.

[197] S. Langer, N. Baldwin, H. Phillips, Head-End Separation of Triso-Coated Fissile and Fertile Particles for High-Temperature Gas-Cooled Reactors, Nuclear Technology, 12 (1971) 26-30.

[198] C. FitzqerakJ, V. Vaughen, K. Notz, R. Lowrie, Head-End Reprocessing Studies with Irradiated HTGR-Type Fuels: III. Studies With RTE-7: TRISO UC_2-TRISO ThC_2, (1975).

[199] G. Del Cui, C. Forsberg, W. Rickman, TRISO-Coated Fuel Processing to Support High-Temperature Gas-Cooled Reactors, ORNL, 27 (2002) 4-00.

[200] A. Radkowsky, A. Galperin, The Nonproliferative Light Water Thorium Reactor: A New Approach to Light Water Reactor Core Technology, Nuclear Technology, 124 (1998) 215-222.

[201] P.R. Kasten, Review of the Radkowsky Thorium Reactor Concept, Science & Global Security, 7 (1998) 237-269.

[202] R. Rainey, J. Moore, Laboratory Development of the Acid Thorex Process for Recovery of Thorium Reactor Fuel, Nuclear Science and Engineering, 10 (1961) 367-371.

[203] R. Rainey, J. Moore, Laboratory Development of the Acid Thorex Process for Recovery of Consolidated Edison Thorium Reactor Fuel, Oak Ridge National Laboratory, Tennessee, 1962.

[204] A. Nuttin, D. Heuer, A. Billebaud, R. Brissot, C. Le Brun, E. Liatard, J.M. Loiseaux, L. Mathieu, O. Meplan, E. Merle-Lucotte, Potential of Thorium Molten Salt Reactors Detailed Calculations and Concept Evolution with a View to Large Scale Energy Production, Progress in Nuclear Energy, 46 (2005) 77-99.

[205] L. Mathieu, D. Heuer, R. Brissot, C. Garzenne, C. Le Brun, D. Lecarpentier, E. Liatard, J.-M. Loiseaux, O. Meplan, E. Merle-Lucotte, The Thorium Molten Salt Reactor: Moving on from the MSBR, Progress in Nuclear Energy, 48 (2006) 664-679.

[206] L. Mathieu, D. Heuer, E. Merle-Lucotte, R. Brissot, C. Le Brun, E. Liatard, J.-M. Loiseaux, O. Maplan, A. Nuttin, D. Lecarpentier, Possible Configurations for the Thorium Molten Salt Reactor and Advantages of the Fast Nonmoderated Version, Nuclear Science and Engineering, 161 (2009) 78-89.